ISTANBUL TECHNICAL UNIVERSITY ★ GRADUATE SCHOOL OF SCIENCE ENGINEERING AND TECHNOLOGY

EFFECT OF AUSTEMPERING AND ALUMINIZING PROCESSES ON PROPERTIES OF HIGH SILICON SPHEROIDAL GRAPHITE DUCTILE IRONS

Ph.D. THESIS

Yakup YÜREKTÜRK

Department of Metallurgical and Materials Engineering

Metallurgical and Materials Engineering Programme

NOVEMBER 2018

ISTANBUL TECHNICAL UNIVERSITY ★ GRADUATE SCHOOL OF SCIENCE ENGINEERING AND TECHNOLOGY

EFFECT OF AUSTEMPERING AND ALUMINIZING PROCESSES ON PROPERTIES OF HIGH SILICON SPHEROIDAL GRAPHITE DUCTILE IRONS

Ph.D. THESIS

Yakup YÜREKTÜRK
(506132405)

Department of Metallurgical and Materials Engineering

Metallurgical and Materials Engineering Program

Thesis Advisor: Prof. Dr. Murat BAYDOĞAN

NOVEMBER 2018

İSTANBUL TEKNİK ÜNİVERSİTESİ ★ FEN BİLİMLERİ ENSTİTÜSÜ

YÜKSEK SİLİSYUMLU KÜRESEL GRAFİTLİ DÖKME DEMİRLERE UYGULANAN ÖSTEMPERLEME VE ALÜMİNYUMLAMA İŞLEMLERİNİN MALZEME ÖZELLİKLERİNE ETKİSİ

DOKTORA TEZİ

Yakup YÜREKTÜRK
(506132405)

Metalurji ve Malzeme Mühendisliği Anabilim Dalı

Metalurji ve Malzeme Mühendisliği Programı

Tez Danışmanı: Prof. Dr. Murat BAYDOĞAN

KASIM 2018

Yakup YÜREKTÜRK, a Ph.D. student of ITU Graduate School of Science, Engineering and Technology student ID 506132405, successfully defended the thesis entitled “Effect of Austempering and Aluminizing Processes on Properties of High Silicon Spheroidal Graphite Ductile Irons”, which he prepared after fulfilling the requirements specified in the associated legislations, before the jury whose signatures are below.

Thesis Advisor : **Prof. Dr. Murat BAYDOĞAN** ....
Istanbul Technical University

Jury Members : **Prof. Dr. Sakin ZEYTİN** ....
Sakarya University

Prof. Dr. Hüseyin ÇİMENOĞLU ....
Istanbul Technical University

Assist. Prof. Dr. C. Fahir ARISOY ....
Istanbul Technical University

Assist. Prof. Prof. Dr. Hakan YILMAZER ....
Yıldız Technical University

Date of Submission : 07 November 2018
Date of Defense : 22 November 2018

To my daughter Zeynep Zümra, wife Medine and Parents

FOREWORD

To begin with, I would like to express my gratitude to supervisor Professor Murat BAYDOĞAN for his academic guidance and motivation. He has guided me through the challenging topics and gave me valuable comments whenever I needed. It would have been impossible for me to complete this dissertation without his support and encouragement.

I would also like to thank instructors Professor Hüseyin ÇİMENOĞLU and Professor Eyüp Sabri KAYALI for giving me the opportunity to work in their research groups. They made important contributions to my education and helped me improve myself. I am really grateful to M.Sc. Faiz MUHAFFEL for sharing his precious working and laboratory experiences with me. I also wish to special thank to my friends M.Sc. Onur TAZEGÜL, M.Sc. Doğukan ÇETİNER, M.Sc. Mert ALTAY, M.Sc. Emre TEKOĞLU, M.Sc. Burçak AVCI, M.Sc. Sıddıka MERTDİNÇ and M.Sc. Selçuk YEŞİLTEPE for their supports, warm friendships, cheerful conversations, and original ideas.

I am grateful to Professor Hüseyin ÇİMENOĞLU, who has been Project Coordinator of the TUBITAK (The Scientific and Technological Research Council of Turkey) 1505 Project with Project No. 5160013, for giving me the opportunity to work in this project as a scholarship student. I also thank TUBITAK for supporting me within the scope of this project.

Special thanks to my parents, Recep YÜREKTÜRK and Özgül YÜREKTÜRK, receive my deepest gratitude for their support and prayers during my studies. I would also like to thank my brothers, Abdullah YÜREKTÜRK and Eyyüp YÜREKTÜRK, for their encouragement and motivation.

I would like to thank Istanbul Technical University Scientific Research Found. No: 41008 for its financial support.

Last but not the least, I would like to thank my wife, Medine YÜREKTÜRK, for her limitless patience, encouraging support and love during the Ph.D. works. I also get strength from my beloved daughter, Zeynep Zümra YÜREKTÜRK, when it is hard to cope with the difficulties, that made this thesis a reality.

November 2018

Yakup YÜREKTÜRK
(Metallurgy and Materials Engineer)

TABLE OF CONTENTS

Page

FOREWORD .... **ix**
TABLE OF CONTENTS .... **xi**
LIST OF TABLES .... **xiii**
LIST OF FIGURES .... **xv**
SUMMARY .... **xvii**
ÖZET .... **xxi**
1. INTRODUCTION **1**
  1.1 Ductile Irons 1
    1.1.1 Solution strengthened ferritic ductile irons (SSFs) 3
  1.2 Austempering Heat Treatment 4
    1.2.1 Austempered ductile irons (ADIs) 6
  1.3 Hot-dip Aluminizing (HDA) and Diffusion Annealing of HDA Coating 7
2. RESEARCH OBJECTIVES **9**
  2.1 Effect of Microstructural Features on Mechanical and Magnetic Properties of Austempered High-silicon Ductile Irons 9
  2.2 Characterization of Ferritic Ductile Iron Subjected to Successive Aluminizing and Austempering 9
  2.3 Effect of Aluminizing and Austempering Processes on Structural, Mechanical and Wear Properties of a SSF Ductile Iron 10
3. EFFECT OF MICROSTRUCTURAL FEATURES ON MECHANICAL AND MAGNETIC PROPERTIES OF AUSTEMPERED HIGH-SILICON DUCTILE IRONS **11**
  3.1 Introduction 11
  3.2 Experimental Details 12
    3.2.1 Materials 12
    3.2.2 Thermodynamic equilibrium calculations 13
    3.2.3 Heat-treatment 14
    3.2.4 Structural characterization 14
    3.2.5 Hardness and tensile tests 15
    3.2.6 Vibrating sample magnetometer (VSM) measurements 15
  3.3 Results and Discussion 16
    3.3.1 Modified Fe–C phase diagram and structural analysis 16
    3.3.2 Volume fraction of retained austenite 21
    3.3.3 Mechanical properties 22
    3.3.4 Magnetic properties 26
  3.4 Conclusions 30
4. CHARACTERIZATION OF FERRITIC DUCTILE IRON SUBJECTED TO SUCCESSIVE ALUMINIZING AND AUSTEMPERING **33**
  4.1 Introduction 33
  4.2 Experimental Procedure 34
    4.2.1 Sample preparation 34
    4.2.2 Hot-dip aluminizing 35

4.2.3 Austempering 35
4.2.4 Structural characterization 35
4.2.5 Hardness and tensile tests 36
4.2.6 Corrosion tests 36
4.3 Results and Discussion 37
4.3.1 Formation of intermetallic layers between solid iron and molten aluminum 37
4.3.2 Evolution of intermetallic layers and substrate microstructures by austempering 38
4.3.3 Mechanical properties 43
4.3.4 Corrosion properties 44
4.4 Conclusions 48
5. EFFECT OF ALUMINIZING AND AUSTEMPERING PROCESSES ON STRUCTURAL, MECHANICAL AND WEAR PROPERTIES OF A SSF DUCTILE IRON 51
5.1 Introduction 51
5.2 Experimental Details 52
5.2.1 Material and preparation 52
5.2.2 Coating procedure and heat treatment 53
5.2.3 Structural characterizations 54
5.2.4 Mechanical properties 54
5.2.5 Tribological properties 54
5.3 Results and Discussion 55
5.3.1 Coating characterization after hot-dip aluminizing 55
5.3.2 Coating characterization after austempering on hot-dip aluminized ductile iron 56
5.3.3 Mechanical and microstructural properties 60
5.3.4 Tribological characteristics 62
5.4 Conclusions 68
6. CONCLUSIONS AND RECOMMENDATIONS 69
REFERENCES 71
CURRICULUM VITAE 81

LIST OF TABLES

Page

Table 1.1 : Mechanical properties of SSF and conventional grades according to EN 1563:2012 standard. **4**
Table 3.1 : Chemical compositions and quantitative metallographic analyses of the samples.. .... **12**
Table 3.2 : Mechanical properties of the as-cast and austempered samples. **22**
Table 4.1 : Mechanical properties of samples. **44**
Table 4.2 : Results of potentiodynamic polarization tests applied to uncoated and coated samples **46**
Table 5.1 : Point EDX analysis results of HDA sample. **56**
Table 5.2 : Point EDX analysis results of HDA + ADI sample. **57**
Table 5.3 : Mechanical and microstructural properties of investigated samples. **62**

LIST OF FIGURES

Page

Figure 1.1 : Flowchart of ductile iron casting production [4]. **2**
Figure 1.2 : Schematic of ductile/cast iron microstructures [15]. **3**
Figure 1.3 : Austempering process in steel and ductile iron [26]. **5**
Figure 1.4 : Typical austempering heat treatment cycle in ductile iron [26]. **6**
Figure 1.5 : Comparison of tensile strength-elongation behaviour between ADI and steels [35] **6**
Figure 1.6 : Growth mechanism of HDA coating [61]. **8**
Figure 3.1 : Optical micrographs of as-cast (a) GJS 500-14 and (b) GJS 600-10 samples.. .... **13**
Figure 3.2 : Modified Fe–C phase diagrams for (a) GJS 500-14- and (b) GJS 600-10-grade ductile irons.. .... **16**
Figure 3.3 : Optical micrographs of austempered GJS 500-14- (a, c, e) and GJS 600-10- (b, d, f) grade ductile iron: (a, b) ADI-270, (c, d) ADI-330, and (e, f) ADI-390.. .... **17**
Figure 3.4 : XRD patterns of austempered (a) GJS 500-14 and (b) GJS 600-10 samples.. .... **18**
Figure 3.5 : Variation of carbon content in austenite (C_γ) and total austenite carbon content ($X_\gamma C_\gamma$) with respect to austempering temperature for (a) GJS 500-14- and (b) GJS 600-10-grade ductile irons.. .... **19**
Figure 3.6 : Variation of mean ferritic cell size with respect to austempering temperature for (a) GJS 500-14- and (b) GJS 600-10-grade ductile irons.. .... **20**
Figure 3.7 : Variation of retained austenite volume fraction with respect to austempering temperature for (a) GJS 500-14- and (b) GJS 600-10-grade ductile irons.. .... **21**
Figure 3.8 : Hall–Petch-type plot showing the variation of yield strength as a function of the inverse of the square root of the mean ferritic cell size (d) for all austempered samples.. .... **24**
Figure 3.9 : Variation of tensile strength as a function of Brinell hardness.. .... **24**
Figure 3.10 : Variation of strain-hardening exponent (n) and elongation at fracture with respect to austempering temperature for (a) GJS 500-14- and (b) GJS 600-10-grade ductile irons. **25**
Figure 3.11 : Magnetization (M–H) curves of as-cast (100% ferritic) and (a) GJS 500-14 and (b) GJS 600-10 austempered samples.. .... **26**
Figure 3.12 : Variation of saturation magnetizations with respect to austempering temperature. **28**
Figure 3.13 : Variations of remanence (M_r) and the mean ferritic cell size (d) with respect to austempering temperature for (a) GJS 500-14- and (b) GJS 600-10-grade ductile irons. **28**
Figure 3.14 : Variation of coercivity, hardness, and mean ferritic cell size with austempering temperature for (a) GJS 500-14- and (b) GJS 600-10-grade ductile irons. **30**

Figure 4.1 : Surface XRD pattern (a) and cross-sectional SEM micrograph (b) of the hot-dip aluminized sample before austempering.................................... **38**
Figure 4.2 : XRD results of coatings after austempering... **39**
Figure 4.3 : Surface elemental mapping of ADI-270 sample.. .... **39**
Figure 4.4 : Cross-sectional SEM micrographs after austempering at various temperatures: (a) ADI-270, (b) ADI-330 and (c) ADI-390..................... **41**
Figure 4.5 : Cross-section elemental mapping of ADI-270 sample.......................... **42**
Figure 4.6 : High-magnification FE-SEM micrographs of substrate after austempering at various temperatures: (a) ADI-270, (b) ADI-330 and (c) ADI-390.. **43**
Figure 4.7 : Potentiodynamic polarization curves of uncoated and coated samples in 3.5 wt.% NaCl solution.. .... **45**
Figure 4.8 : Surface SEM micrographs with XRD patterns of (a) the uncoated and (b) coated (ADI-270) samples after 48-h SSCT.................................... **46**
Figure 4.9 : Cross-sectional SEM micrograph of ADI-270 sample after complete removal of corrosion products from the surface.. .... **47**
Figure 5.1 : Optical micrograph of GJS 600-10 ductile iron in as-cast state.. .... **53**
Figure 5.2 : Schematic representations of coating procedure and heat treatment..... **53**
Figure 5.3 : (a) Cross-sectional SEM micrograph, (b) magnified micrograph of framed rectangular region in (a), and (c) surface XRD pattern of HDA sample.. **55**
Figure 5.4 : Cross-sectional elemental mapping of HDA sample............................. **56**
Figure 5.5 : (a) Cross-sectional SEM micrograph of HDA + ADI sample, (b) magnified micrograph of framed rectangular region in (a), and (c) magnified micrograph of substrate... **57**
Figure 5.6 : Cross-sectional elemental mapping of HDA + ADI sample.. .... **58**
Figure 5.7 : Surface SEM micrograph (a), EDX analysis result of marked points (b), and surface XRD pattern (c) of HDA + ADI sample............................. **59**
Figure 5.8 : Hardness of phases on HDA + ADI sample.. **60**
Figure 5.9: Stress-strain curves of investigated samples.. .... **61**
Figure 5.10 : Wear track profiles of investigated samples: (a) As-cast and HDA samples, and (b) ADI and HDA + ADI samples.................................... **62**
Figure 5.11 : Worn surface SEM micrographs of as-cast and HDA samples: (a) as-cast sample, (b) magnified micrograph of worn surface region in (a), (c) HDA sample, (d) magnified micrograph of worn surface region in (c).. **63**
Figure 5.12 : Worn surface of as-cast and HDA samples: (a) Raman and (b) EDX patterns.. .... **64**
Figure 5.13 : Worn surface SEM micrographs of ADI and HDA + ADI samples: (a) ADI sample, (b) magnified micrograph of worn surface region in (a), (c) HDA + ADI sample, (d) magnified micrograph of worn surface region in (c).. **65**
Figure 5.14 : Worn surface of ADI and HDA+ADI samples: (a) Raman and (b) EDX patterns.. .... **66**
Figure 5.15 : Variations of friction coefficient as a function of sliding distance for investigated samples.. **67**

EFFECT OF AUSTEMPERING AND ALUMINIZING PROCESSES ON PROPERTIES OF HIGH SILICON SPHEROIDAL GRAPHITE DUCTILE IRONS

SUMMARY

EN 1563 standard covering spheroidal graphite ductile cast irons was revised in March 2012 and the solution strengthened ferritic (SSF) grades of GJS-450-18, GJS-500-14, and GJS-600-10 with higher Si contents (wt% 3.2-4.3) were newly added to the standard. A higher amount of silicon (as solute atoms) makes a solid solution by replacing iron (solvent atoms) in the lattice, contributes to lattice distortion and makes dislocation motion more difficult. Thus strength of the material increases. Solid solution strengthening improves ductility almost two times, and approximately 50-60% more tool life during machining to SSF ductile cast irons compared to conventional ferritic / pearlitic ductile cast irons is obtained.

Although ductile cast irons have good features in terms of mechanical and wear properties, further improvement of these properties were needed in line with industry demands. In accordance with these demands, austempering heat treatment is applied to the ductile cast irons. With austempering treatment, the existing matrix transforms into acicular ferrite and high-carbon retained austenite, resulting in enhanced strength and toughness. While the austempering process is a method commonly applied to traditional ductile cast irons, it has also been recently applied to SSF ductile cast irons. The results showed that austempered high silicon ductile cast irons showed higher strength and higher ductility than austempered conventional ductile cast irons. Due to the high amount of silicon in the SSF ductile cast iron, it prevents the formation of cementite (Fe_3C), which is likely to occur in the microstructure after the austempering process, and protects the mechanical properties against the detrimental effect of the cementite. Since high silicon in SSF ductile cast irons increases the eutectoid temperature, higher temperatures are required in the austenitizing step of the austempering process than in conventional ductile cast irons. High austenitizing temperature provides more rapid diffusion of carbon to austenite and austenite becomes richer in carbon. Due to the higher enrichment of carbon obtained at the higher austenitization temperature, thermodynamic stabilization austenite are improved.

Because the austenitization step of the austempering process occurs at high temperatures (> 850 °C), it is inevitable that the materials are exposed to oxidation and decarburization if the protective atmosphere is not provided at these temperatures. Thanks to hot-dip aluminizing (HDA) coating technique, these materials can be protected from decarburisation during austenitizing as well as providing high-temperature oxidation resistance to these materials. After HDA coating, generally, a top layer of Al (with $FeAl_3$), a middle layer of $FeAl_3$, and an inner layer of Fe_2Al_5 were formed in the coating. The Al top layer by forming Al_2O_3 at high temperatures protects the material from oxidation and decarburisation. The mechanical properties of the coating are improved by transforming the brittle intermetallics ($FeAl_3$, Fe_2Al_5) present in the coating structure into iron-rich and tougher FeAl and Fe_3Al structures at high

temperatures. Therefore, it is expected that the HDA coating of ductile cast irons before austempering may contribute to the surface properties of the material.

In the first phase of the experimental studies carried out within the scope of the thesis, GJS-500-14 and GJS-600-10 grade ductile irons were austenitized at 975 °C for 2 h, and then they were subjected to the austempering process at predetermined temperatures of 270 °C, 330 °C, and 390 °C for 60 min. The effects of different austempering temperatures on the structural, mechanical and magnetic properties of materials were investigated. It was found that volume fraction of retained austenite increases with increasing austempering temperature, the increase in the amount of silicon from 3.7% (GJS-500-14) to 4.3% (GJS-600-10) negatively affect the ductility and toughness, and also the optimum mechanical properties are obtained at austempering temperature of 330 ° C. One of the factors affecting the optimum mechanical properties is the thin-coarse form of the acicular ferrite found in the microstructure and the other one is the amount of retained austenite is in the range of about 20-25%. The magnetic properties of the SSF ductile irons vary depending on the chemical content and microstructural constituents of the materials, namely, saturation magnetization values decrease with increasing silicon content and increasing retained austenite content. The decrease in saturation magnetization with the increase of silicon content can be explained by the effect of alloying elements, which are capable of decreasing the magnetic moment and consequently the saturation magnetization of iron. The decrease in saturation magnetization due to microstructural constituents can be explained by variations in the ferromagnetic (ferrite) and paramagnetic (austenite) phase volume fractions, namely, saturation magnetization reached a maximum value in the ductile irons containing the highest amount of ferrite.

In the second phase of the thesis, HDA coating (750 °C, 5 min) was applied to GJS-500-14 grade SSF ductile irons, and then aluminized ductile irons were austenitized at 975 °C for 2 h, followed by austempering at predetermined temperatures of 270 °C, 330 °C, and 390°C for 60 min. The effect of additional HDA coating on the mechanical and corrosion properties of the materials was investigated. Compared to as-cast ductile iron without aluminizing, the hardness and strength values and ductility of HDA coated ductile irons were almost unchanged in the as-cast condition. The strength values decreased slightly but the ductility increased in the aluminized and austempered condition. This can be explained by the brittle phases (Fe_2Al_5, $FeAl_2$) in the coating structure and the high temperature gradient during cooling from the austenitizing temperature (975 °C) to the austempering temperature (270 °C–390 °C), which was responsible for the crack formation because of the brittle nature of the Al-rich intermetallics in combination with the tensile stress acting on them. After anodic potentiodynamic polarization corrosion tests, the corrosion resistance of the HDA coated and subsequent austempered ductile irons was found to increase by about 3-6 times compared to as-cast ductile iron without aluminizing. This increment in corrosion resistance can be explained by lack of graphite nodules on the coating surface, namely, graphite nodules are not directly exposed to the corrosive environment in the case of coated ductile irons, unlike as-cast ductile irons without aluminizing. Therefore, graphitic corrosion, which is a common corrosion mechanism of as-cast ductile iron, it was not expected to be the driving mechanism of corrosion in the coated ductile irons.

The third and final phase of the thesis, another grade of SSF ductile irons (GJS-600-10) were coated with HDA technique (750 °C, 5 min), and then austempering heat treatment has been performed in the austempering condition optimized from previous

studies (975 ° C 2 h for austenitization, 330 ° C 1 h for austempering). After the materials were characterized structurally and mechanically, room temperature wear characteristics were predominantly examined. It was found that wear resistance was increased by about 30% when austempering is applied after the HDA coating. The porous Fe_2O_3 oxide formed by abrasion on the surface of austempered ductile iron without aluminizing, and this led to increment in wear rate with plastically deformed graphite during wear test. In the case of coated and austempered ductile iron, although thin Al_2O_3 layer produces cracks on the surface during wear, the newly formed Fe-Al intermetallics in the subsurface during austenitizing provides strong support during wear.

In conclusion, single austempering without aluminizing significantly improved both strength and toughness of SSF ductile irons (GJS-500-14, GJS-600-10), as expected. With the increasing austempering temperature, the volume fraction of ferrite (ferromagnetic) decreased and accordingly the volume fraction of retained austenite (paramagnetic) increased. Utilizing the change of magnetic properties with increasing austempering temperature, the retained austenite volume fraction of these materials were calculated by a magnetic method and these values were found to be compatible with the measurements made by XRD method. Additional HDA coating before austempering improved the surface properties (corrosion, wear) of the SSF ductile irons. Mechanical properties of the HDA coated and austempered ductile irons satisfied the requirements of grades 1200-3, 900-8, and 800-10. A further achievement of HDA coating is that the surface is prevented against decarburization and scaling without a need for further protective atmosphere during austenitizing.

YÜKSEK SİLİSYUMLU KÜRESEL GRAFİTLİ DÖKME DEMİRLERE UYGULANAN ÖSTEMPERLEME VE ALÜMİNYUMLAMA İŞLEMLERİNİN MALZEME ÖZELLİKLERİNE ETKİSİ

ÖZET

Küresel grafitli dökme demirler diğer döküm malzemelerle (gri dökme demir, çelik, demirdışı) kıyaslandığında % 25'lik oranla gri dökme demirden (% 46) sonra dünyada en çok üretilen döküm malzemelerdir. Toplamda yıllık yaklaşık 100.8 milyon ton metal döküm üretimi göz önüne alındığında bunun 25.2 milyon tonunu küresel grafitli dökme demirler oluşturmaktadır. Dünyanın en iyi 5 demir döküm üreticisi sırasıyla Çin, Amerika, Hindistan, Japonya ve Almanya olmakla beraber bu ülkelerde, Çin dışında, küresel grafitli dökme demir üretimi gri dökme demir üretiminden fazladır. Diğer yandan Türkiye dünya metal döküm üretim endüstrisinin yaklaşık % 1.4'lük kısmını oluşturmaktadır.

Küresel grafitli dökme demirlere olan talebin fazla olmasının sebebi bu malzemelerin sahip olduğu üstün yorulma özellikleri, yüksek aşınma direnci, yüksek çekme dayanımı, yüksek süneklik gibi özellikleridir. Bunun yanında küresel grafiti dökme demirler çeliklerle kıyaslandığında yaklaşık % 10 daha az yoğunluğa sahiptir. Tüm bu özelliklerinden dolayı küresel grafitli dökme demirler başta otomotiv olmak üzere birçok mühendislik uygulamasında kullanılmaktadır.

Küresel grafitli dökme demirlerin mekanik özellikleri mikroyapıları ile doğrudan ilişkili olup bu malzemelerin mikroyapısı tamamen ferritik, ferritik/perlitik ya da tamamen perlitik olabilmektedir. Bu mikroyapıyı belirleyen en önemli etkenler malzemenin kimyasal bileşimi ve soğuma hızıdır. Malzemenin soğuma hızı yüzey bölgelerinden iç bölgelere doğru azaldığı için malzemenin yüzeye yakın bölgelerinde perlit miktarı yüksek soğuma hızının etkisiyle fazladır. Buna karşın iç bölgelerde ise düşük soğuma hızının etkisiyle ferrit miktarı fazladır. Dolayısıyla malzemenin yapısı, ferrit ile perlit yapılarının farklı özellikler sergilemesine bağlı olarak, her bölgesinde aynı olmamaktadır. Perlit yapısının ferrit fazına kıyasla daha sert olmasının bir sonucu olarak malzemenin başta sertlik dağılımı olmak üzere mekanik özellikleri yüzey bölgelerinden iç bölgelere doğru gidildikçe farklılık göstermektedir. Bu durum işlenebilirlik açısından problem çıkarmakta olup özellikle talaşlı imalat sırasında kesici uç takım ömrünün kısalmasına, iş ve zaman kaybına neden olmaktadır. Tüm bunlar göz önünde bulundurulduğunda malzemenin tek fazlı mikroyapıya sahip olması başta sertlik dağılımı olmak üzere malzemenin mekanik özelliklerinin her bölgesinde birbirine yakın olması açısından önem arzetmektedir.

Küresel grafitli dökme demirlerle ilgili EN 1563 standardı Mart 2012 yılında revize edilerek ferritik matrisli (yüksek silisyumla katı çözelti sertleşmesi uygulanmış) GJS-450-18, GJS-500-14 ve GJS-600-10 yüksek silisyumlu dökme demirler standarda eklenmiştir. Yüksek silisyum (ağ.% 3.2–4.3) yapı içerisinde demir atomlarının yerini alarak (yeralan) katı çözelti oluşturmakta, bu sayede tamamen ferritten oluşan tek fazlı yapı elde edilmektedir. Burdaki katı çözelti sertleşmesi perlitin dayanım artırıcı görevine alternatif bir çözüm oluşturmanın yanısıra, geleneksel ferritik/perlitik dökme

demirlere kıyasla aynı dayanım değerlerinde % 100'e varan süneklik artışı ve talaşlı imalat sırasında yaklaşık % 50-60 daha fazla kesici uç takım ömrü sağlamaktadır.

Küresel grafitli dökme demirler her ne kadar iyi mekanik ve aşınma özelliklerine sahip olsalarda endüstrinin talepleri doğrultusunda bu özelliklerinin daha da iyileştirilmesi ihtiyacı doğmuştur. Bu talepler doğrultusunda en uygun yöntem olarak küresel grafitli dökme demirlere östemperleme ısıl işlemi uygulanmaktadır. Östemperleme işlemiyle mevcut matris iğnesel ferrit ve yüksek karbonlu östenitten oluşan ösferrit mikroyapısına dönüşerek malzemeye hem dayanım hem de tokluk kazandırmaktadır. Östemperleme işlemi geleneksel dökme demirlere sıklıkla uygulanan bir yöntem olmakla beraber, son yıllarda katı çözelti sertleşmesi uygulanmış yüksek silisyumlu dökme demirlere de uygulanmıştır. Elde edilen bulgular yüksek silisyumlu östemperlenmiş dökme demirlerin geleneksel östemperlenmiş dökme demirlere göre daha yüksek dayanım ve daha yüksek süneklik gösterdiğini ortaya koymuştur. Yüksek silisyumlu dökme demirler içeriğinde bulunan yüksek miktarda silisyumdan (ağ.% 3.2–4.3) dolayı östemperleme işlemi sonrası yapıda oluşması muhtemel sementit (Fe_3C) oluşumunu engelleyerek mekanik özellikleri kırılgan sementitin zararlı etkilerinden korur. Yüksek silisyum malzemenin ötektoid sıcaklığını artırdığı için östemperleme işleminin östenitleme aşamasında geleneksel dökme demirlere kıyasla daha yüksek sıcaklıklar tercih edilir. Yüksek östenitleme sıcaklığı karbonun daha hızlı bir şekilde östenite difüzyonunu sağlamakla birlikte östeniti karbonca daha zengin bir hale getirir ve böylece östenit termodinamik açıdan daha kararlı bir hal almış olur.

Östemperleme işleminin östenitleme aşaması yüksek sıcaklıklarda (>850 °C) gerçekleştiğinden bu sıcaklıklarda malzemelerin koruyucu atmosfer ortamı sağlanmadığı takdirde gerek oksidasyona gerekse de dekrabürizasyona maruz kalması kaçınılmazdır. Sıcak daldırma alüminyumlama (hot dip aluminizing-HDA) kaplama yöntemi sayesinde bu malzemelere yüksek sıcaklık oksidasyon direnci kazandırmanın yanısıra bu malzemeler östenitleme sırasında dekarbürizasyondan korunabilir. HDA sonrası genel olarak kaplamanın en üst kısmında alüminyum (Al), ortasında $FeAl_3$ ve en iç kısmında Fe_2Al_5 intermetaliği oluşur. Kaplamanın en dış kısmında olan Al yüksek sıcaklıklarda en üst katmanda Al_2O_3 oluşturarak malzemeyi oksidasyondan ve dekarbürizasyondan korur. HDA yapısında bulunan mevcut gevrek ve kırılgan intermetalikler ($FeAl_3$, Fe_2Al_5) ise yüksek sıcaklıklarda demirce zengin ve daha tok FeAl ve Fe_3Al yapılarına dönüşebilerek kaplamanın mekanik özelliklerini iyileştirir. Dolayısıyla HDA kaplamanın sunmuş olduğu bu iyi özelliklerinden dolayı dökme demirlerin östempereleme işlemi öncesinde kullanılması malzemenin yüzey özelliklerine katkı sunması beklenir.

Tez kapsamında gerçekleştirilen deneysel çalışmaların ilk aşamasında, GJS-500-14 ve GJS-600-10 grade yüksek silisyumlu küresel grafitli dökme demirler 975 °C'de 2 saat östenitleme işlemine tabi tutulduktan sonra farklı östempereleme sıcaklıklarında (270 °C, 330 °C, 390 °C) 1 saat östempereleme işlemine tabi tutulmuştur. Farklı östemperleme sıcaklıklarının malzemelerin yapısal, mekanik ve manyetik özelliklerine etkisi incelenmiştir. Östemperleme sıcaklığı arttıkça yapıdaki kalıntı östenit miktarının arttığı, malzemenin kimyasal içeriğindeki silisyum miktarının ağırlıkça % 3.7'den (GJS-500-14) % 4.3'e (GJS-600-10) artmasının malzemenin süneklik ve tokluk değerlerini olumsuz etkilediği, ve ayrıca 330 °C östempereleme sıcaklığında optimum mekanik özelliklerin elde edildiği görülmüştür. Optimum mekanik özellikleri belirleyen faktörler mikroyapıda bulunan iğnesel ferritin ince-kaba arasında bir formda olması ve ayrıca kalıntı östenit miktarının yaklaşık % 20-25 aralığında olmasıdır. Manyetik özelliklerin malzemenin kimyasal içeriğine ve mikroyapısal bileşenlerine bağlı olarak değiştiği, şöyle ki, artan silisyumla ve artan kalıntı östenit miktarıyla beraber manyetik doygunluk değerinin azaldığı görülmüştür. Artan silisyumla manyetik doygunluğun azalması, alaşım elementlerinin malzemedeki manyetik momenti azaltma etkisidir. Artan kalıntı östenit miktarıyla manyetik doygunluğun azalması ise, ösferrit yapısında bulunan ferromanyetik ferritin hacimce azalmasına bağlı olarak paramanyetik östenitin hacimce artmasının sonucudur.

Tez kapsamında gerçekleştirilen deneysel çalışmaların ikinci aşamasında, GJS-500-14 kalitedeki dökme demirler HDA yöntemi ile 750 °C'de 5 dakika kaplanmış, sonrasında yine aynı östemperleme koşullarda, 975 °C'de 2 saat östenitleme ve sonrasında 3 farklı östemperleme sıcaklığında (270 °C, 330 °C, 390 °C) 1 saat, östemperleme ısıl işlemi uygulanmıştır. İlave HDA kaplamanın malzemelerin mekanik ve korozyon özelliklere etkisi incelenmiştir. Döküm halindeki kaplamasız malzemeye kıyasla, sadece HDA kaplanmış (östemperlenmemiş) malzemenin mekanik özelliklerinin neredeyse değişmediği görülmüştür. HDA kaplanmış ve sonrasında östemperlenmiş malzemeler sadece östemperlenmiş (kaplamasız halde) malzemeler ile kıyaslandığında ise dayanım değerlerinin bir miktar düştüğü buna karşın süneklik değerlerinin önemli ölçüde arttığı görülmüştür. Dayanım değerlerindeki düşüşe, kaplama yapısında bulunan gevrek Fe_2Al_5 ve $FeAl_2$ fazlar ve östenitleme sıcaklığından (975 °C) östemperleme sıcaklıklarına (270 °C-390 °C) soğutma sırasında oluşan yüksek sıcaklık gradyenine bağlı kaplama yapısında oluşan çatlaklar ve boşluklar etki etmiştir. Süneklik değerlerindeki artışa ise kaplama yapısında bulunan sünek FeAl ve α-Fe tabakalarının olumlu yönde etki ettiği görülmüştür. Elektrokimyasal korozyon sonrası, HDA kaplanmış ve sonrasında östemperlenmiş malzemelerin korozyon dirençlerinin döküm halindeki kaplamasız malzemeye kıyasla yaklaşık 3-6 kat arası artış gösterdiği görülmüştür. Korozyon direncindeki bu artışa, kaplamasız malzemenin yüzeyindeki grafitlerin grafitik korozyona neden olmasına karşın kaplamalı malzemede grafit nodüllerinin doğrudan korozif ortama maruz kalmaması önemli katkı sağlamıştır.

Deneysel çalışmaların üçüncü aşamasında ise tez kapsamında kullanılan diğer kalitedeki GJS-600-10 yüksek silisyumlu dökme demirler HDA (750 °C, 5 dakika) yöntemiyle kaplanmış ve akabinde daha evvel yapılan çalışmalardan optimize edilen östemperleme koşulunda (975 °C 2 saat östenitleme, 330 °C 1 saat östemperleme) östemperleme ısıl işlemine tabi tutulmuştur. Malzemeler yapısal ve mekaniksel olarak karakterize edildikten sonra ağırlıklı olarak oda sıcaklığındaki aşınma özellikleri irdelenmiştir. HDA kaplanmış ve ardından östemperlenmiş malzemelerin sadece östemperlenmiş (kaplamasız halde) malzemelere kıyasla aşınma direncinde yaklaşık % 30 oranında artış olduğu görülmüştür. Sadece östemperlenmiş dökme demir malzemelerin yüzeyinde aşınma etkisiyle oluşan poroz Fe_2O_3 malzemedeki aşınma kaybını artırırken aynı zamanda malzemede bulunan grafitlerde plastik deformasyona uğrayarak buna eşlik etmiştir. Kaplamalı malzemede ise, yüzeyde ince bir tabaka halinde bulunan Al_2O_3 aşınmayla beraber sahip olduğu yüksek sertliğe bağlı olarak yüzeyde çatlaklar oluşturmuşsa da, kaplamada bulunan diğer tabakalar (Fe_2Al_5 + $FeAl_2$, FeAl, α-Fe) alttan yüzeye destek oluşturarak aşınmanın daha derinlere ulaşmasını önlemiştir.

Sonuç olarak, GJS-500-14 ve GJS-600-10 kalite yüksek silisyumlu dökme demirlere sadece östemperleme işleminin uygulanması beklenildiği üzere malzemelere hem dayanım hem de tokluk kazandırmıştır. Artan östemperleme sıcaklığıyla ferrit (ferromanyetik) oranı azalmış buna bağlı olarak kalıntı östenit (paramanyetik) oranı artmıştır. Manyetik özelliklerin östemperleme sıcaklığıyla değişiminden yararlanılarak, bu malzemelerin kalıntı östenit hacim oranları manyetik yöntemle hesaplanmış ve bu değerlerin XRD yöntemiyle yapılan ölçümlerle uyumlu olduğu görülmüştür. Yüksek silisyumlu dökme demirlerin östempereleme öncesi HDA yöntemiyle kaplanması ise gerek östemperleme işleminin östenitleme safhasında koruyucu atmosfer gereksinimini ortadan kaldırdığı için gerekse de östemperleme sonrası malzemelerin yüzey özelliklerini (korozyon, aşınma) geliştirdiği için önem arzetmektedir. HDA kaplanmış ve östemperlenmiş malzemeler mekanik özelliklerin iyi yönde gelişmesini sağlamış ve östemperlenmiş dökme demirler için istenen minimum mekanik özellikleri ilgili BS EN 1564 standardında yer alan 1200-3, 900-8, ve 800-10 sınıfı malzemelerin özelliklerini karşılamıştır.

1. INTRODUCTION

1.1 Ductile Irons

Ductile irons (DIs), also known as nodular or spheroidal graphite irons (SGIs), are widely used in several applications, such as railway brake disks, valves, air spring member and heavy-duty engine blocks [1,2] . DIs, which mainly consist of carbon (C), silicon (Si), manganese (Mn), phosphorus (P), sulphur (S) and balance iron (Fe), are produced through the addition of either magnesium or cerium in the liquid cast iron melt to precipitate the graphite as nodules [3]. The flowchart of ductile iron casting production [4] is given in Figure 1.1. Theoretically, the charge represents the chemical composition of the ductile irons including main elements like carbon, silicon, and phosphorus. Each of these elements in the base composition changes solidification temperature and eutectic composition and this affects the mechanical properties of ductile iron. Therefore, the degree of this effect can be calculated by the parameter defined as carbon equivalent ($CE = C\% + 1/3(Si\% + P\%)$) [5]. It finds out whether the alloy is in eutectic (4.3%), hypoeutectic (< 4.3%) or hypereutectic (> 4.3%) composition. The CE value is a useful guide to foundry behaviour because it provides guidance on an optimum range of composition [6,7]. Due to high CE (> 4.3%), primary graphite can occur and this leads to a detrimental effect on the mechanical properties of the upper part of the casting as a result of graphite flotation [6,8]. Therefore, it is desirable that this CE value is close to the eutectic in terms of good castability with reduced shrinkage and mechanical properties. Although magnesium (with some calcium, cerium and other rare earth elements) has been the most widely used between 0.015% and 0.05% as spheroidizing agent in the production of ductile iron castings, its low boiling point, low solubility in ductile iron and the violent reaction associated with it, strictly restrict the use of metallic magnesium in castings [9]. Therefore, magnesium ferrosilicon alloys, which contain from 3 to 9 percent magnesium, have been started to be used for nodularizing in castings recently because of their low cost and applicability to various castings with different sections and CE values [9,10]. On the other hand, inoculation is an important aspect for ductile iron casting production because it performed to obtain sufficient nucleation sites for dissolved carbon to precipitate as graphite rather than cementite (Fe_3C) in the iron [11]. Traditionally, commercial inoculants have been based on ferrosilicon alloys containing metallic additives such as calcium, barium, strontium, aluminum, and zirconium [11,12].

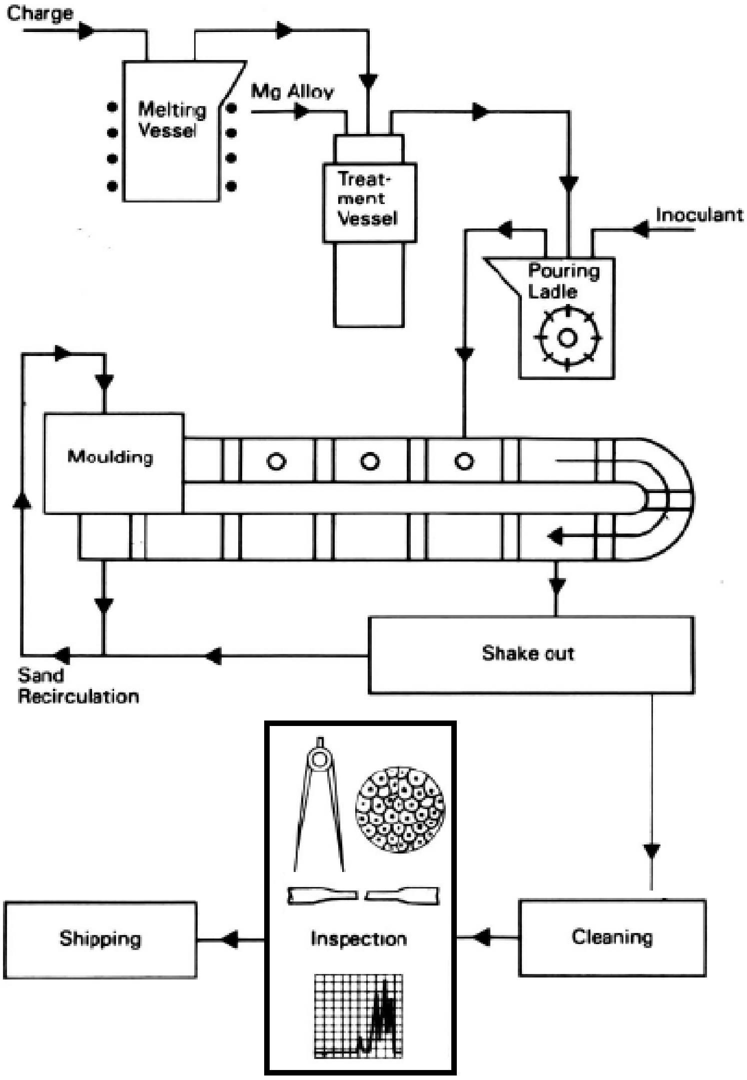
Charge
Melting Vessel
Mg Alloy
Treat-ment Vessel
Inoculant
Pouring Ladle
Moulding
Shake out
Sand Recirculation
Inspection
Shipping
Cleaning

Figure 1.1 : Flowchart of ductile iron casting production [4].

Thanks to this sphere-like morphology of graphite, DIs exhibit far better mechanical properties (yield strength, tensile strength, and ductility) compared to gray cast irons having flaky graphite which act as notches or stress concentrators making it extremely susceptible to brittle failure [13,14]. On the other hand, the mechanical properties of ductile irons are directly related to their microstructure, which can be fully ferritic, fully pearlitic or a combination of ferrite and pearlite with spheroidal graphite in the matrix. These microstructural properties are largely dependent on chemical composition and solidification–cooling rate, which related to the section size of the castings and alloying elements [15]. Schematic representation of ductile/cast iron microstructures is shown in Figure 1.2.

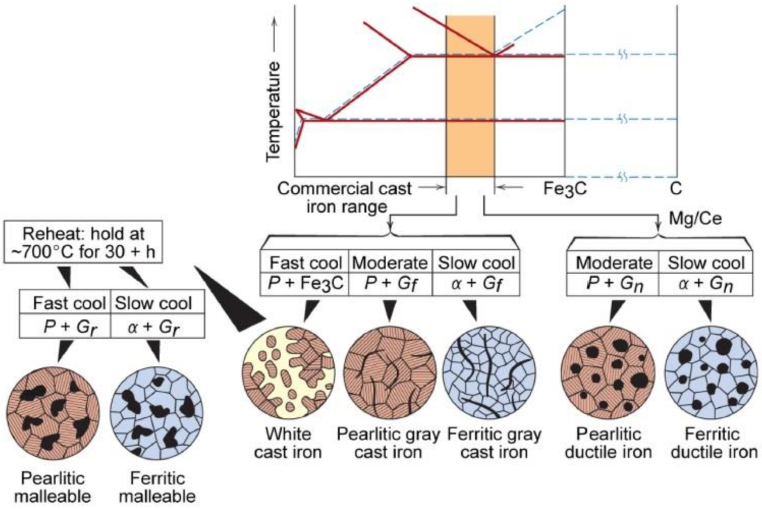
Temperature
Commercial cast iron range
Fe3C
C
Mg/Ce
Reheat: hold at ~700°C for 30 + h
Fast cool
P + Gr
Slow cool
α + Gr
Fast cool
P + Fe3C
Moderate
P + Gf
Slow cool
α + Gf
Moderate
P + Gn
Slow cool
α + Gn
White cast iron
Pearlitic gray cast iron
Ferritic gray cast iron
Pearlitic ductile iron
Ferritic ductile iron
Pearlitic malleable
Ferritic malleable

Figure 1.2 : Schematic of ductile/cast iron microstructures [15].

Ductile iron's properties are changed by adding various alloying elements such as silicon, nickel, chromium, copper, and molybdenum [15,16]. Amongst them, silicon has become a most important alloying element recently with a revision of the EN 1563 European standard in 2012, solution strengthened ferritic (SSF) grades of GJS-450-18, GJS-500-14 and GJS-600-10 with higher Si contents (3.2-4.3%) were newly added to this standard [17,18].

1.1.1 Solution strengthened ferritic ductile irons (SSFs)

Solution strengthened ferritic ductile irons (SSFs), also sometimes referred as high-silicon (Hi-Si) irons, have become an interesting group of materials owing to their castability in complex geometries without requiring too much machining, excellent mechanical properties and relatively low cost [17,19]. Silicon is a strong graphitizer, and it promotes the formation of a fully ferritic matrix making a solid solution. This single-phase metal matrix provides uniform hardness distribution throughout the matrix that improved the machinability of SSFs [20]. According to solid solution strengthening mechanism, solid solutions can be formed by substitutional atoms or interstitial atoms depending on the size of the solute atoms [21,22]. For SSFs, silicon atoms (solute) replace iron atoms (solvent) in the crystal lattice of iron and form a substitutional solid solution, where the solute atoms are large enough to replace the solvent atoms (r_{Si} = 0.118 nm, r_{Fe} = 0.124 nm). The crystal lattice is distorted as a result of the difference in the size of the iron atoms and silicon atoms. Thus, the movement of dislocations becomes more difficult, namely, large stress needed to move dislocation. This causes an increase in the strength of the material [23]. A unique combination of high strength with good elongation is achieved for SSFs by solution strengthening through higher silicon content preventing the formation of carbides in the matrix as compared to conventional (ferritic-pearlitic) grades. Table 1.1 shows the mechanical properties of SSF and conventional grades according to EN 1563:2012 standard. As shown in Table 1.1, SSF grades exhibited better yield strength with higher ductility than conventional grades at the same level of tensile strength.

Table 1.1 : Mechanical properties of SSF and conventional grades according to EN 1563:2012 standard.

	Ductile Iron Grades					
	SSF			Conventional		
Property	GJS-450-18	GJS-500-14	GJS-600-10	GJS-450-10	GJS-500-7	GJS-600-3
Yield strength (0.2%, MPa)	350	400	470	310	320	370
Tensile strength (MPa)	450	500	600	450	500	600
Elongation (%)	18	14	10	10	7	3

According to EN 1563:2012 standard, the silicon content (wt%) of SSF grades of GJS-450-18, GJS-500-14 and GJS-600-10 are approximately 3.2, 3.8 and 4.3, respectively. This revealed that as silicon content increases, yield strength and tensile strength increased whereas elongation decreased. On the other hand, it was reported that increasing the silicon content above 4.3 wt% results in a sudden drop in elongation due to increase in embrittlement of ferrite, which is also as a result of rising ductile-brittle transition temperature depending on the increased silicon content [17,23].

1.2 Austempering Heat Treatment

Austempering is the isothermal transformation, which is applied to ferrous alloys (most notably steel and ductile iron) at a temperature below that of pearlite formation and above that of martensite formation in order to yield a microstructure of high strength, with some ductility and good wear resistance [24,25]. As shown in Figure

1.3 [26], in steel, austempering produces a bainite microstructure, which is directly transformed by austenite whereas in ductile irons it produces a microstructure of acicular (bainitic) ferrite (α) and high carbon retained austenite (γ) known as ausferrite (stage I). However, the high carbon retained austenite (γ) decomposes into ferrite and carbide after prolonged times of austempering (stage II). Namely, if the austempering time is kept too long, undesirable bainite will form. Unlike steel, bainite in ductile iron microstructures exhibits lower toughness and ductility [27].

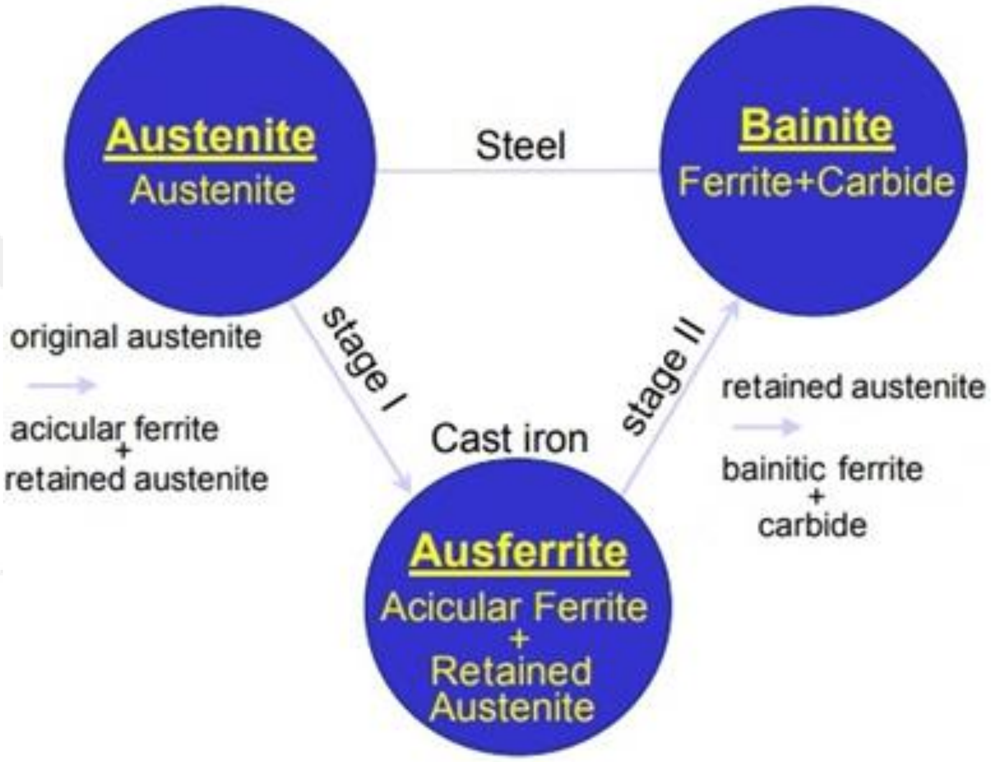
Austenite
Austenite
Steel
Bainite
Ferrite+Carbide
original austenite
acicular ferrite
+
retained austenite
stage I
stage II
Cast iron
retained austenite
bainitic ferrite
+
carbide
Ausferrite
Acicular Ferrite
+
Retained
Austenite

Figure 1.3 : Austempering process in steel and ductile iron [26].

Figure 1.4 shows a typical austempering heat treatment cycle in ductile iron [26]. The austempering heat treatment is started by heating to and holding at a temperature in the austenite-phase range (usually 850 to 950 ºC), where the as-cast matrix transforms into austenite and gets enriched with carbon from the graphite nodules, for a sufficient time (usually 2 h) to produce homogeneous austenite and saturate the austenite with carbon. The next step is to quench (usually in molten salt) rapidly to the austempering temperature in the range 250-450 ºC for a period of time, which typically range from 1 to 4 h depending on alloy content and section size, to achieve the isothermal transformation to obtain an optimum structure of acicular ferrite and carbon-enriched austenite. The last step is cooling to room temperature [26,28].

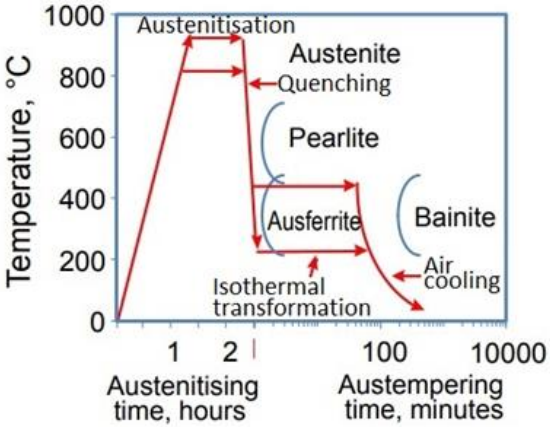

Figure 1.4 : Typical austempering heat treatment cycle in ductile iron [26].

1.2.1 Austempered ductile irons (ADIs)

Austempered ductile irons (ADIs) are heat treated form of as-cast nodular ductile iron to yield an ausferritic microstructure consisting of acicular ferrite (α) and high carbon retained austenite (γ). Thanks to this microstructure, ADIs have emerged as an important engineering material due to their high strength with good ductility, good wear resistance, high fatigue strength and fracture toughness [29–32] . In addition, ADIs have higher specific strength as compared to steels because they are approximately 10% lighter than steels [33]. Because of this properties, ADI is increasingly being used in many areas of mechanical engineering, automotive and engine construction, and they also show excellent economic competitiveness with steels and aluminum alloys [34]. Figure 1.5 shows the comparison of tensile strength-elongation behaviour between ADI and steels [35].

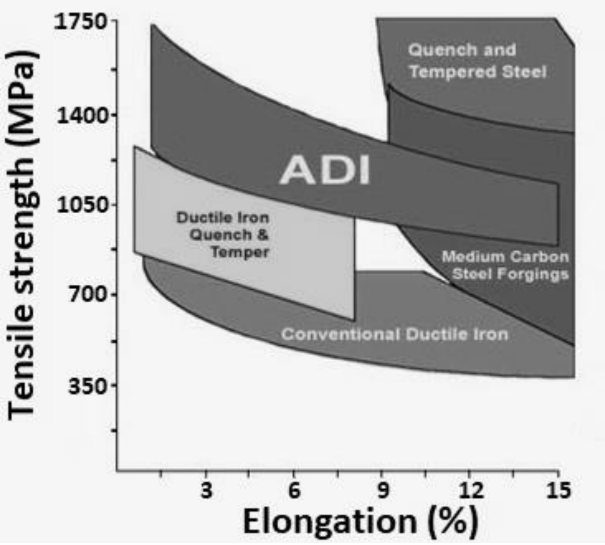

Figure 1.5 : Comparison of tensile strength-elongation behaviour between ADI and steels [35].

Although most of the studies have been focused on conventional ADI [36–38], recently, numerous works have been conducted on austempered alloyed ductile iron [17,19,39,40]. Among them, austempering treatment on high silicon (3.2-4.3 wt%) alloyed ferritic ductile irons (SSFs) stand out in order to obtain further improvement as mechanical properties on these ductile irons [41–43]. Silicon is the one of the most important alloying element in ADI because it increases eutectoid temperature, and thus, high austenitisation temperature is required to avoid the formation of detrimental pro-eutectoid ferrite in the microstructure after austempering [43,44]. Therefore, thermodynamic stabilization and the amount of the austenite phase after austempering are improved due to an obtained high enrichment of carbon as a result of high austenitisation temperature [43]. Moreover, a high amount of silicon present in SSFs further delays or completely prevents the formation of embrittling bainite (ferrite + Fe_3C) and retains a substantial amount of stable high carbon austenite during austempering [19,43]. Additionally, segregation of manganese and molybdenum is also found to be decreased by high silicon in SSFs [43]. Consequently, high silicon content (3.2-4.3 wt%) in ADI meets minimum requirements for mechanical properties of ADI grades specified in EN 1564:2011 standard providing improvements in both strength and ductility compared to conventional ADI having a silicon content of 2.4-2.6 wt% [17,43].

1.3 Hot-dip Aluminizing (HDA) and Diffusion Annealing of HDA Coating

Hot-dip aluminizing (HDA) is an effective coating technique to protect ferrous materials surface from corrosion, oxidation, decarburization and wear at high temperature [45–48]. Because of this advantages, HDA is mostly applied to structural steel parts used in automotive, which exposure to the high temperature during hot stamping process [49,50]. On the other hand, HDA can provides additional oxidation resistance to high silicon ductile irons used as engineering materials in high-temperature applications such as furnace parts, turbocharger housings and exhaust manifolds [51,52].

According to A463/A463M standard, the HDA coating is available in two types: one of them is “Coating Type I” and the other one is “Coating Type II”. Type I is coated with aluminum-silicon alloy containing typically 5–11% silicon to promote better adherence, whereas Type II is manufactured using a coating bath of pure aluminum.

Type I is intended principally for heat-resisting applications and also for uses where corrosion and heat are involved [45,53]. Moreover, it exhibits superior resistance to atmospheric and salt spray corrosion compared to zinc-coated materials [54]. On the other hand, Type II is intended principally for use in applications requiring corrosion and fire resistance [45,55]. In both grades, intermetallic compounds are seen between the top layer and the substrate. This intermetallic layer is thicker in Type II than Type I due to the presence of a certain level of silicon in the molten aluminum, which helps in reducing the thickness of the intermetallic compound layer [45,56].

The formed intermetallic phases are mostly Fe_2Al_5 and $FeAl_3$ after HDA in molten aluminum, and these phases are very brittle in nature [57,58]. Among these phases, the $FeAl_3$ is initially formed at the interface between substrate and coating materials by the diffusion of iron atoms into aluminium layer, and the Fe_2Al_5 which exhibits a tongue-like morphology is then formed at the interface between the $FeAl_3$ and substrate [59,60]. After HDA, the $FeAl_3$ close to top Al coating and the Fe_2Al_5 close to the substrate are formed. The growth mechanism of the HDA coating is schematically shown in Figure 1.6 [61].

As a result of brittle intermetallic phases ($FeAl_3$, Fe_2Al_5), the cracks and peel off may occur in the HDA coating during secondary operations such as bending and machining [48]. Therefore, it is necessary to control intermetallic compound layers for improving interfacial strength in processing techniques by the application of diffusion annealing to transform brittle intermetallic phases into comparatively ductile Fe-rich phases such as FeAl and Fe_3Al [62–64]. The transformation of the HDA coating not only alters the mechanical properties of the aluminized material, but also influences the useful lifetime [65,66]. Diffusion annealing on HDA coating is usually performed in the temperature range from 500 to 1000 °C for 5 min to 480 h [62–64] .

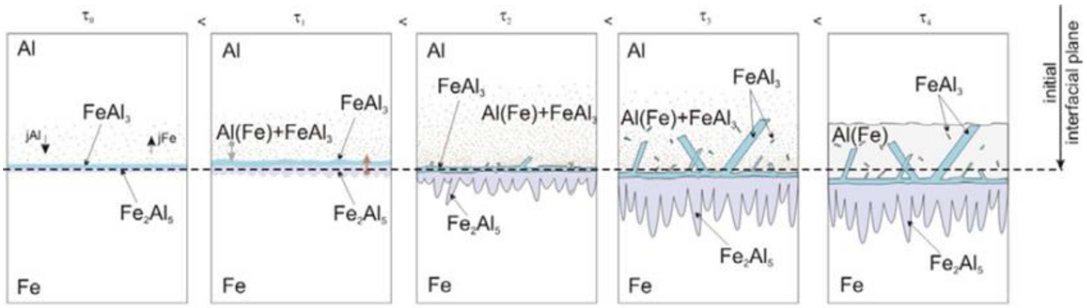

Figure 1.6 : Growth mechanism of HDA coating [61].

2. RESEARCH OBJECTIVES

2.1 Effect of Microstructural Features on Mechanical and Magnetic Properties of Austempered High-silicon Ductile Irons

In this study, mechanical and magnetic properties of high silicon ductile irons (GJS 500-14- and GJS 600-10) with fully ferritic initial microstructures were investigated after being austempered at 270-390 °C for 60 min. Results showed that hardness and strength as well as ductility are mainly controlled by morphologies and volume fractions of the phases in the austempered microstructures. More silicon in the chemical composition results in a significant decrement in ductility and toughness. For this reason, when high toughness is concerned, GJS 600-10 grade ductile iron containing more silicon should not be a preferred grade for austempering. In the view point of magnetic properties, saturation magnetization strongly depends on the austempering temperature, whereas remenance and coercivity are somewhat related to mean ferritic cell size and the solute atoms in the chemical composition.The results of this study are given in Chapter 3.

2.2 Characterization of Ferritic Ductile Iron Subjected to Successive Aluminizing and Austempering

In this study, GJS-500-14 solution-strengthened ferritic ductile iron was subjected to successive hot-dip aluminizing (HDA) and austempering. The combination of these processes resulted in the formation of a thin Al_2O_3 layer on the iron surface, an intermetallic layer beneath the surface, and an ausferritic microstructure in the interior. Scanning electron microscopy-energy dispersive X-ray spectrometry and X-ray diffraction analyses allowed the qualitative identification of the intermetallics formed due to the aluminizing and their transformation after austempering. Corrosion properties of the final product were also evaluated by potentiodynamic polarization and salt spray corrosion tests, and the surfaces and subsurfaces of the coating layer were examined. The results revealed that this combined process improved the corrosion resistance of ductile iron and enhanced its mechanical properties. The results of this study are given in Chapter 4.

2.3 Effect of Aluminizing and Austempering Processes on Structural, Mechanical and Wear Properties of a SSF Ductile Iron

The aim of this study is to investigate the effect of aluminizing process on structural, mechanical and tribological properties of GJS 600-10 solution strengthened ferritic (SSF) ductile iron before and after austempering heat treatment. The as-cast samples were coated by hot-dip aluminizing (HDA) at 750 °C for 5 min. For austempering heat treatment, the as-cast and aluminized samples were austenitized at 975 °C for 2 h and austempered (ADI) at 330 °C for 1 h, which were referred as ADI and HDA + ADI samples, respectively. Structural characterizations made by scanning electron microscopy (SEM), energy dispersive X-ray spectrometry (EDX) and X-ray diffraction (XRD) analysis revealed that single HDA process produced a coating of $FeAl_3$ and Fe_2Al_5 layers with an Al topcoat on the surface. By the application of austempering after HDA, as-aluminized coating layer transformed into Fe_2Al_5 + $FeAl_2$, FeAl and α-Fe with Al_2O_3 scale on the surface. Tensile tests conducted at room temperature indicated that single HDA does not significantly affect the mechanical properties of the as-cast ductile irons, whereas application of austempering after HDA decreases strength and increases ductility in comparison to ADI samples. Dry sliding wear tests performed against Si_3N_4 ball at room temperature showed that HDA samples exhibited much worse wear resistance than the as-cast samples. However, wear resistance was increased about 30% when austempering is applied after HDA. Formation of various oxides on the worn surfaces of the samples was studied by Raman spectroscopy and EDX analysis. Test results were comparatively evaluated on the basis of surface and subsurface characteristics of the investigated ductile irons, and showed that increased wear resistance can be obtained when HDA is followed by austempering for the ductile iron used in this investigation. The results of this study are given in Chapter 5.

3. EFFECT OF MICROSTRUCTURAL FEATURES ON MECHANICAL AND MAGNETIC PROPERTIES OF AUSTEMPERED HIGH-SILICON DUCTILE IRONS [1]

3.1 Introduction

Austempered ductile irons (ADIs) have remarkable properties such as high strength with good toughness, high wear resistance and fatigue strength owing to their ausferritic microstructures as compared to conventional ductile irons. Because of unique combinations of these properties, ADIs are preferred as an engineering material in many structural applications in the automotive and defense industries and in earth-moving machinery [24,67,68].

Ductile irons containing silicon in the range of 2.8–4.5 wt% can be categorized as high-silicon grades. Silicon, as a ferrite-forming element, encourages the formation of a fully ferritic microstructure in high silicon ductile irons, and decreases total shrinkage during solidification as well [41]. On the other hand, silicon makes a solid solution by replacing iron in the lattice, contributes to lattice distortion and finally makes dislocation motion more difficult.

The mechanical properties of ADIs depend on microstructural features such as ferrite morphology, retained austenite volume fraction and the carbon content of the retained austenite. For example, lower ausferritic microstructure and higher carbon content in the retained austenite enhances fracture toughness, while optimum fracture toughness is obtained when retained austenite was around 25% [30]. High fatigue strength, on the other hand, is attributed to low carbon content and high volume fraction of retained austenite due to possible transformation of low carbon retained austenite into martensite during straining [69].

The magnetic properties of materials strongly depend on their microstructure, chemical composition, and heat-treatment conditions [70]. Especially, microstructural features such as dislocation density, grain size, and the presence of solute atoms and precipitates affect the motion of magnetic domain walls, which, in turn, affects the characteristic magnetic parameters such as coercivity, remanence, hysteresis loss, and saturation magnetization [70,71]. Renzetti et al. [72] revealed that a decrease in coercivity was resulted from the grain size increment in ferritic–martensitic steel. Similarly, a theoretical work performed by Sablik et al. [73] showed that there was a linear relationship between coercivity and the inverse of the grain size.

---

[1] This chapter is based on the paper "Y. Yürektürk, M. Baydoğan, Effect of microstructural features on mechanical and magnetic properties of austempered high-silicon ductile irons, ISIJ Int. 57 (2017) 2049–2057, https://doi.org/10.2355/isijinternational.ISIJINT-2017-167."

Investigations concerning austempered high-silicon ductile irons with fully ferritic microstructures are very limited [41]. Also, there have been few studies on the magnetic properties of ADIs [74]. In the present work, we therefore investigated the mechanical and magnetic properties of austempered high-silicon ductile irons by varying their silicon content, and these properties were correlated each other on a microstructural basis.

3.2 Experimental Details

3.2.1 Materials

The chemical compositions and quantitative metallographic analyses of GJS 500-14- and GJS 600-10-grade high-silicon ductile irons used in the present work were given in Table 3.1. Samples 15 mm in diameter and 5 mm thick were cut from as-cast cylindrical bars. Optical micrographs of the as-cast samples, etched with 4 vol% nital, are presented in Figure 3.1.

Table 3.1 : Chemical compositions and quantitative metallographic analyses of the samples.

Sample	Chemical Composition (wt%)						Nodularity (%)	Nodule Count (mm^{-2})	Graphite Volume (%)
	C	Si	Mn	P	S	Mg			
GJS 500-14	3.3	3.7	0.3	0.029	0.008	0.04	94	215	8.6
GJS 600-10	3.1	4.3	0.2	0.029	0.007	0.05	94	220	9.8

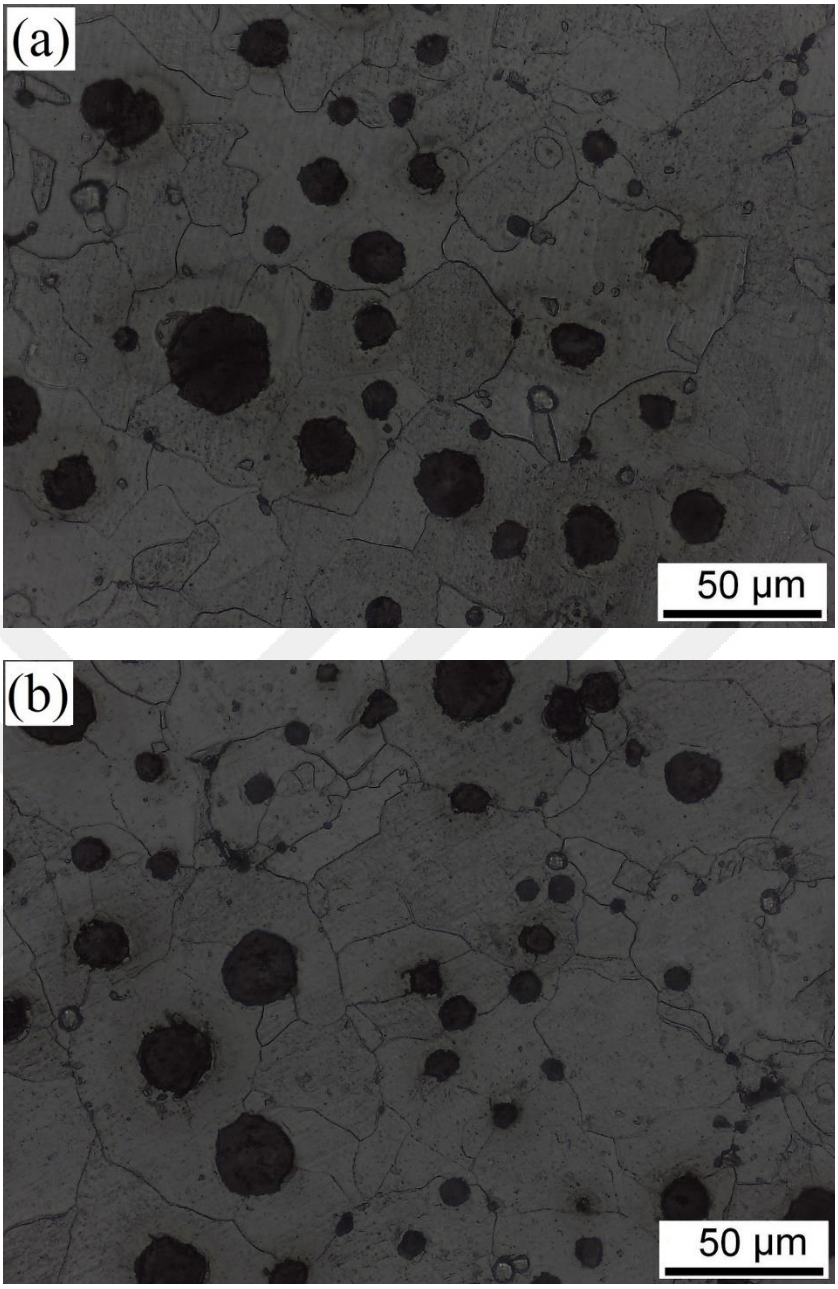

Figure 3.1 : Optical micrographs of as-cast (a) GJS 500-14 and (b) GJS 600-10 samples.

The micrographs reveal that both the GJS 500-14- and GJS 600-10-grade ductile irons had fully ferritic microstructures with high-nodularity graphite distributed throughout the matrix.

3.2.2 Thermodynamic equilibrium calculations

A modified Fe–C phase diagram of the GJS 500-14- and GJS 600-10- grade ductile irons were plotted by using the chemical compositions of the samples through the thermodynamic database program FactSage. The calculation parameters were set as atmospheric air at a pressure of 1 atm.

3.2.3 Heat-treatment

The samples were austenitized in an electrical furnace at 975 °C for 120 min as immersed in cast iron chips to prevent decarburization. Following austenitizing, they were rapidly transferred to a salt bath containing Petrofer® AS135 commercial annealing salt in a stainless-steel container. Austempering was performed by holding the samples in the salt bath at predetermined temperatures of 270, 330, and 390 °C for 60 min, followed by air cooling to room temperature. The temperature was monitored during the austenitizing and austempering steps by a Ni–NiCr thermocouple to ensure that the desired temperatures were maintained. Samples were designated as ADI-270, ADI-330, and ADI-390 according to their austempering temperatures.

3.2.4 Structural characterization

An optical microscope (Leica DM 750M) was used to visualize the microstructures of the austempered samples, which were etched with 4 vol% nital. The quantitative and qualitative phase analyses of the samples were carried out by an X-ray diffractometer (XRD, GBC MMA-027) using Mo–Kα radiation. The accelerating voltage and applied current were 35 kV and 28.5 mA, respectively. The samples were scanned over 2θ angles of 25–45° in steps of 0.05° and at a scanning speed of 0.5° min^{-1}. The acquired XRD patterns were then analyzed with XRD analysis software (X'pert HighScore Plus) to identify the peak positions. The direct comparison method [75]) was used to estimate the volume fractions of ferrite (X_α) and austenite (X_γ) utilizing the integrated intensities of the (2 0 0) and (2 2 0) planes of body-centered cubic (bcc) ferrite and the (2 2 0) and (3 1 1) planes of face-centered cubic (fcc) austenite. The carbon content of the austenite (C_γ, wt%) was determined through Equation 3.1.

$$a_\gamma = 0.3548 + 0.0044C_\gamma \tag{3.1}$$

The lattice parameter of austenite (a_γ, nm) in Equation 3.1 was calculated by using the (2 2 0) and (3 1 1) planes of the austenite peaks. The mean ferritic cell size (d) as a measure of the mean free path of dislocation motion [76] was estimated from the width of the (2 1 1) diffraction peaks of ferrite [75] by using the Scherrer formula shown in Equation 3.2.

$$d = 0.9\,\lambda / (\beta \cos\theta) \tag{3.2}$$

Where d is the particle size, λ is the wavelength of radiation, β is the full width at half maximum intensity, and θ is the Bragg angle.

3.2.5 Hardness and tensile tests

Hardness measurements were carried out on a Brinell Hardness tester (Zwick/Roell ZHU 2.5) using a 187.5 kg load and a 2.5-mm-diameter tungsten ball as the indenter (HB30). The holding time at maximum load was 30 s. The tests were performed by making at least five indentations on each sample and averaging the results.

Duplicate tensile tests of the samples were performed by a servo-hydraulic test machine (MTS Landmark model 370.10) according to the ASTM E8/E8M standard and the average results are reported. All tests were made at a constant engineering strain rate of 0.005 min^{-1} at room temperature. The strain-hardening exponent (n) and strength coefficient (K) of the samples were determined by Holloman’s equation, shown in Equation 3.3.

$$\sigma = K\,\epsilon^{n} \tag{3.3}$$

Where σ and ϵ are the true stress and true strain, respectively.

3.2.6 Vibrating sample magnetometer (VSM) measurements

The samples were first cut to approximately 50 mg using a low-speed alumina disk. Magnetic measurements were carried out in a vibrating sample magnetometer (VSM) at room temperature up to the saturation magnetization; the time constant was 30 ms. The equipment was calibrated using a standard NIST nickel sample with a sensitivity of 10^{-5} emu. Magnetization measurements give the relation between the measured magnetization (M, emu/g) and applied magnetic field (H, Oe). The saturation magnetization (M_s), remanence (M_r), and coercivity (H_c) values of the samples were obtained from the M–H curves. The volume fraction of RA was determined from saturation magnetization values by Equation 3.4 [77].

$$X_{\gamma} = (M_s^{\alpha} - M_s) \;/\; M_s^{\alpha} \tag{3.4}$$

Where M_s^{α} is the experimentally determined saturation magnetization of a 100% ferritic sample and M_s is the saturation magnetization of the austempered samples. It should be noted that this equation can be used when the paramagnetic phase is only austenite.

3.3 Results and Discussion

3.3.1 Modified Fe–C phase diagram and structural analysis

The modified Fe–C phase diagrams of the GJS 500-14- and GJS 600-10- grade ductile irons are shown in Figure 3.2. The most obvious difference between them is the extent of the austenite region. It is clear that there is a relatively larger austenite region in GJS-500-14 than in GJS-600-10 where the silicon content was higher. Accordingly, carbon content of the GJS 500-14 sample can be expected to be slightly higher than GJS 600-10 sample after austenitizing.

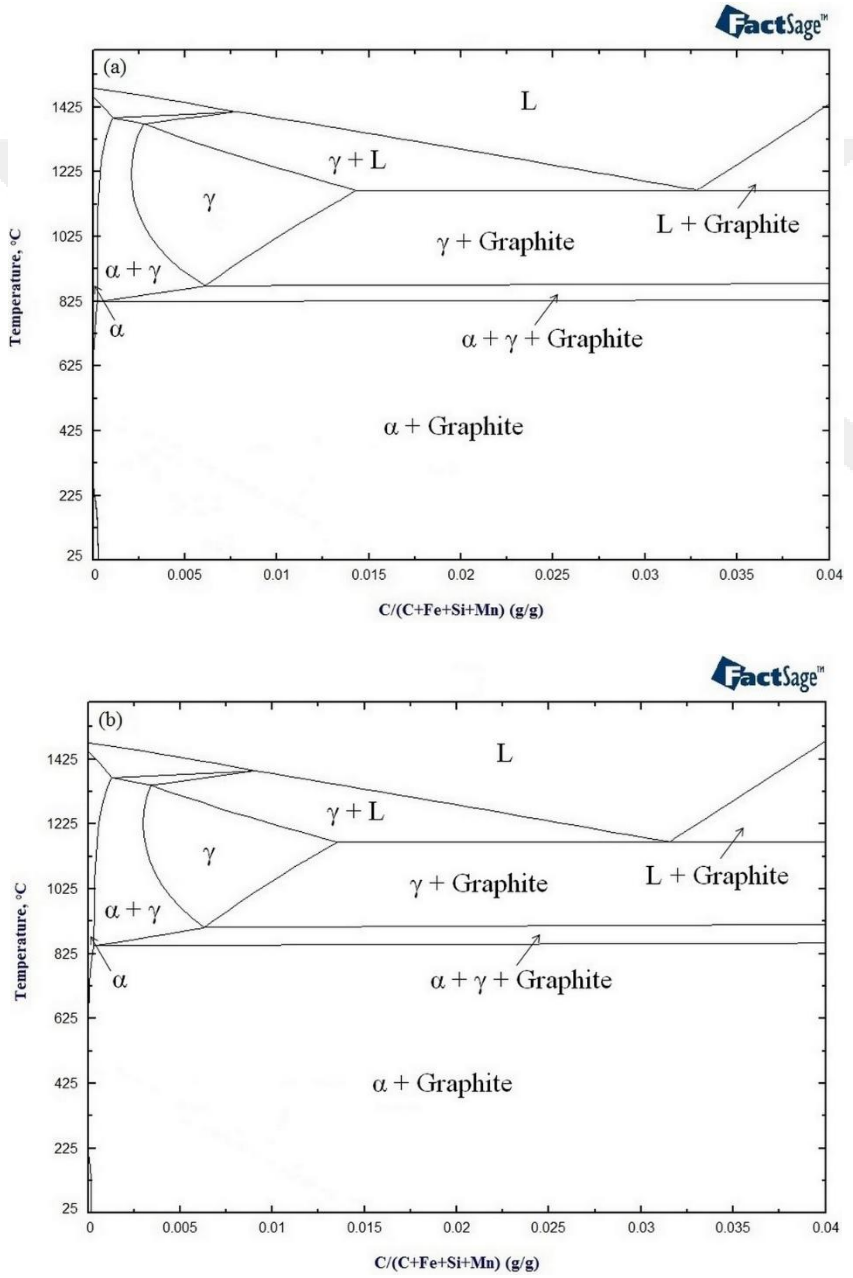

Figure 3.2 : Modified Fe–C phase diagrams for (a) GJS 500-14- and (b) GJS 600-10-grade ductile irons.

Optical micrographs of the austempered GJS 500-14 and GJS 600-10 samples are shown in Figure 3.3. At 270 °C, the predominant microstructure was lower ausferrite, characterized by ferrite needles and RA. As the austempering temperature increased from 270 to 390 °C, the ferrite needles thickened, exhibiting a feathery morphology, which is the characteristic appearance of ferrite in upper ausferritic structures. In terms of the second-stage reaction of austempering, no carbide precipitation was noticed in the microstructures, possibly due to the presence of higher amounts of silicon [78] and relatively short austempering times.

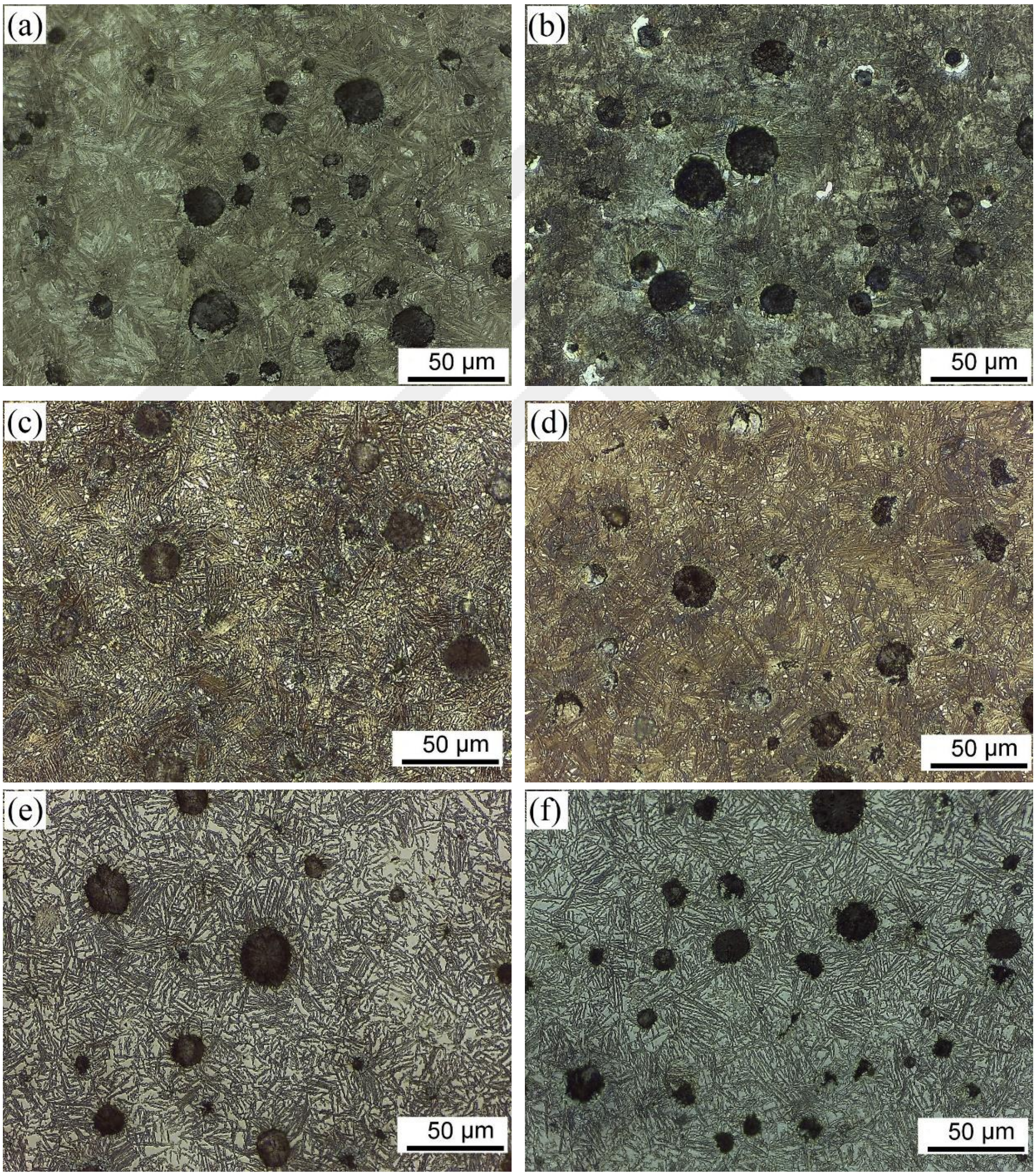

Figure 3.3 : Optical micrographs of austempered GJS 500-14- (a, c, e) and GJS 600-10- (b, d, f) grade ductile iron: (a, b) ADI-270, (c, d) ADI-330, and (e, f) ADI-390.

The XRD patterns of the austempered GJS 500-14 and GJS 600-10 samples are shown in Figure 3.4. Ferrite and austenite peaks are clearly identified, but no carbide peaks were detected which is in agreement to the microstructural observations. As the austempering temperature increased from 270 to 390 °C, the relative intensities of the ferrite peaks decreased, whereas those of the austenite peaks increased for both the GJS 500-14 and GJS 600-10 samples.

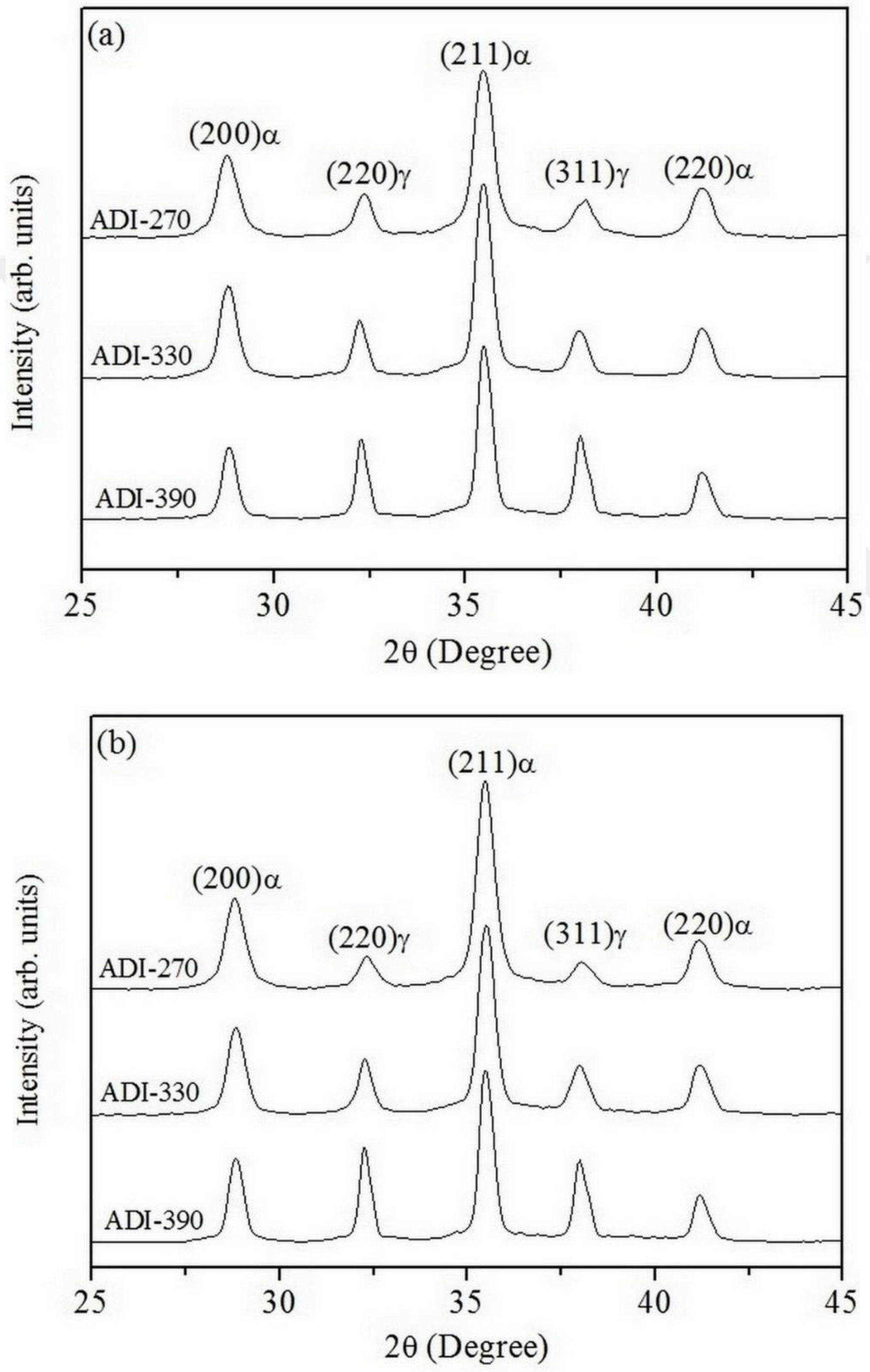

Figure 3.4 : Optical XRD patterns of austempered (a) GJS 500-14 and (b) GJS 600-10 samples.

Figure 3.5 shows the effect of austempering temperature on the carbon content in austenite (C_γ) and the total austenite carbon content ($X_\gamma C_\gamma$). They both increase as the austempering temperature increases because of faster rate of carbon diffusion at a higher austempering temperature [79]. In the view point of ductile iron grade, GJS 500-14 samples have slightly higher austenite carbon content than GJS 600-10 samples. This is in agreement to FactSage predictions shown in Figure 3.2 and can be attributed to more amount of silicon in GJS 600-10 sample.

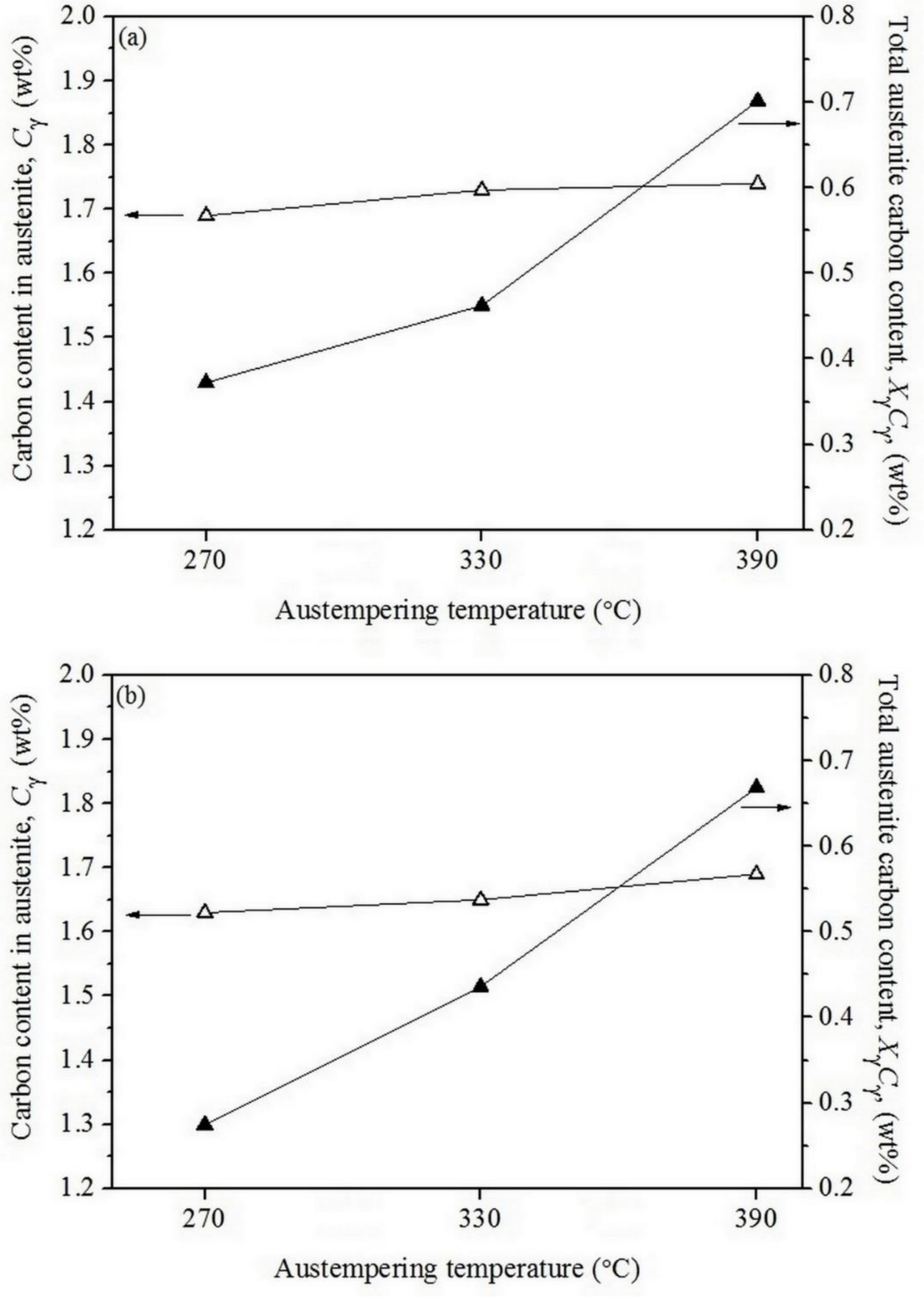

Figure 3.5 : Variation of carbon content in austenite (C_γ) and total austenite carbon content ($X_\gamma C_\gamma$) with respect to austempering temperature for (a) GJS 500-14- and (b) GJS 600-10-grade ductile irons.

The effect of austempering temperature on the mean ferritic cell size (*d*) is presented in Figure 3.6. The value of *d* increases accompanied by a corresponding coarsening of ferrite as the austempering temperature increases because of the lower nucleation rate and higher growth rate of ferrite at a higher austempering temperature [76].

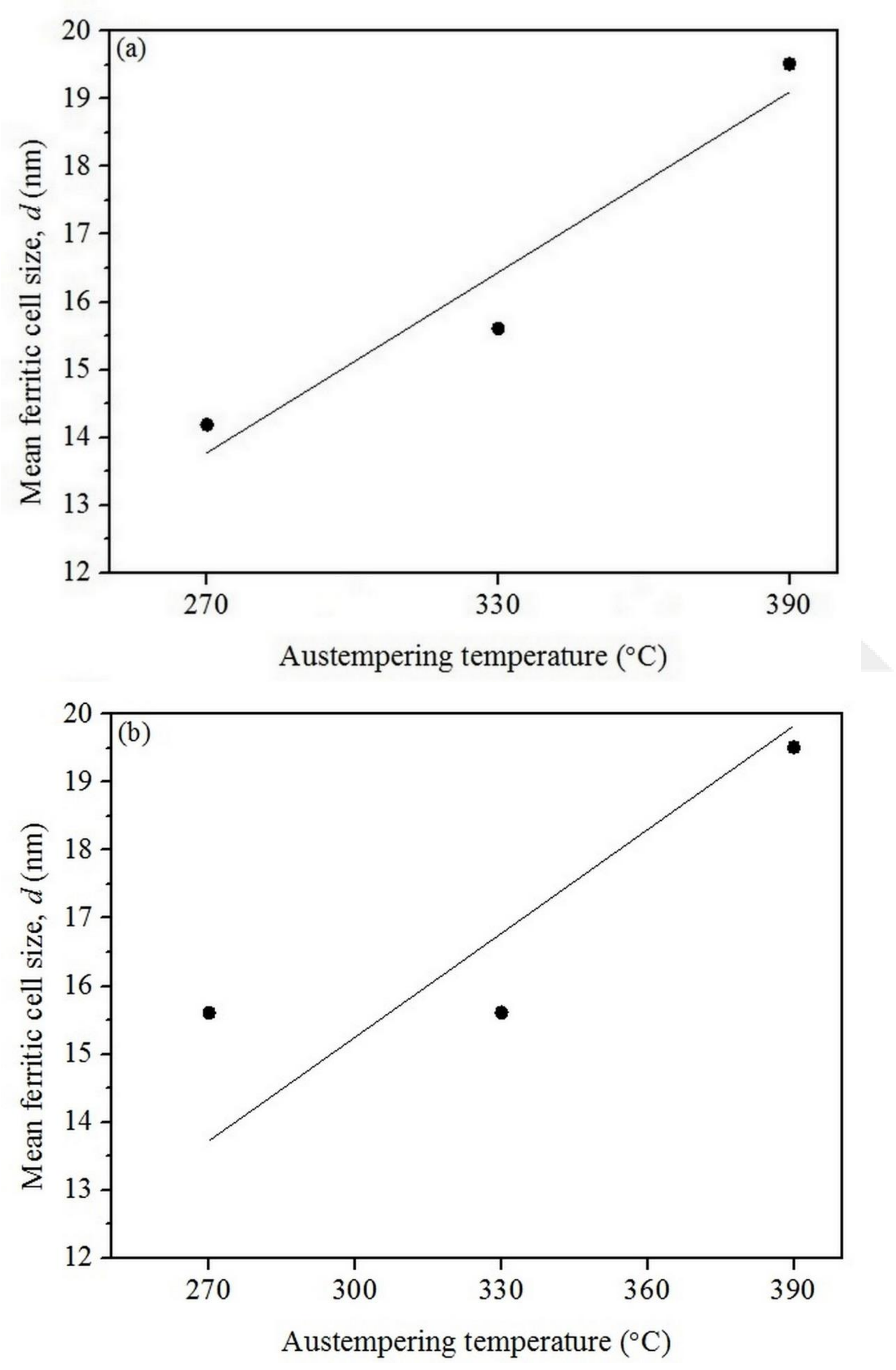

Figure 3.6 : Variation of mean ferritic cell size with respect to austempering temperature for (a) GJS 500-14- and (b) GJS 600-10-grade ductile irons.

3.3.2 Volume fraction of retained austenite

The volume fraction of RA estimated by both XRD and VSM measurements (saturation magnetization values used to estimate volume fraction of the RA are given in Section 3.3.4) is shown in Figure 3.7.

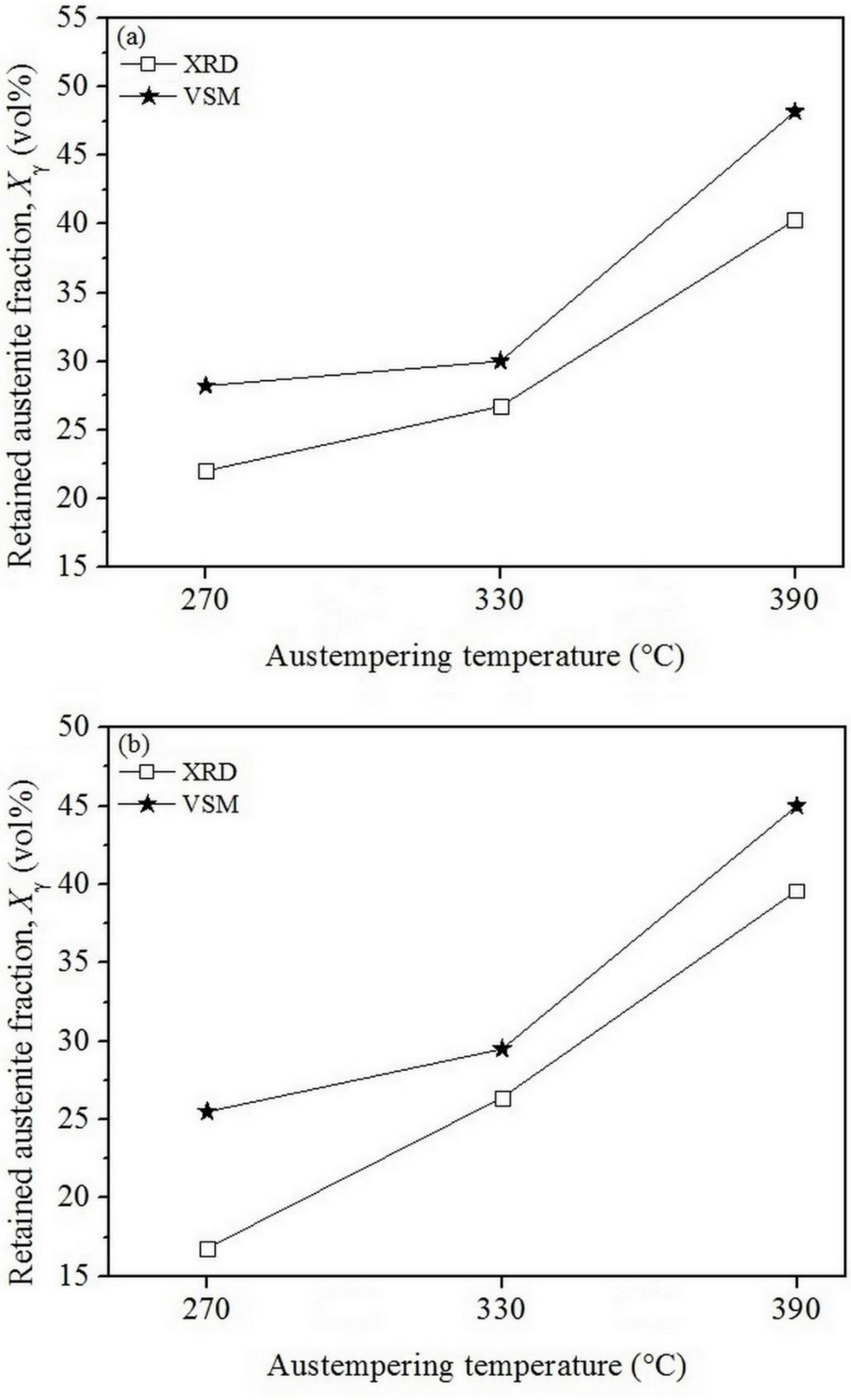

Figure 3.7 : Variation of retained austenite volume fraction with respect to austempering temperature for (a) GJS 500-14- and (b) GJS 600-10-grade ductile irons.

Both techniques show similar trends in that the volume fraction of RA increases with increasing austempering temperature. The volume fraction of RA estimated by VSM measurement was higher than that estimated by XRD measurement at the same austempering temperature. This is mainly attributed to material-related features such as texture and grain size, as well as to the inherent limitations of the XRD technique [80]. The present results are in good agreement with those reported by Jacques et al., [81] who found that the saturation magnetization exhibited larger estimations of the RA content than XRD for TRIP steels.

3.3.3 Mechanical properties

The mechanical properties of the as-cast and austempered GJS 500-14 and GJS 600-10 samples, which were determined by hardness and tensile tests, are presented in Table 3.2.

Table 3.2 : Mechanical properties of the as-cast and austempered samples.

Mechanical Property	Ductile Iron Grade	As-cast samples	Austempered Samples		
			ADI-270	ADI-330	ADI-390
Hardness (HB30)	GJS 500-14	225	477	406	365
	GJS 600-10	235	490	409	370
Yield Strength (MPa)	GJS 500-14	466	1165	1130	625
	GJS 600-10	522	1285	1110	665
Tensile Strength (MPa)	GJS 500-14	633	1635	1368	1096
	GJS 600-10	623	1662	1373	1161
Elongation at Fracture (%)	GJS 500-14	14.1	5.0	10.2	11.7
	GJS 600-10	16.0	3.7	6.3	8.3
Toughness* (10^{-3} J/mm^3)	GJS 500-14	89	82	140	128
	GJS 600-10	100	62	87	96

*Toughness is taken as the product of tensile strength (in MPa) by elongation at fracture (in mm/mm).

It can be seen that the hardness and strength values are inversely proportional to ductility in general. Hardness, yield strength, and tensile strength all significantly decrease, whereas elongation at fracture increases with increasing austempering temperature for both ductile irons. Lower ausferritic structures produced by austempering at 270 °C contained ferrite needles and RA, as shown in Figure 3.3, which are responsible for the higher hardness and strength values due to the high dislocation density in ferrite [82]. The ductility of such a microstructure is generally low because there is less RA (Figure 3.7). In the ADI-330 samples, which were austempered at the mid-temperature in the present study, the ductility increased almost 100%, while the hardness and strength values were lower than those obtained at 270 °C. As the austempering temperature increased to 390 °C, the ferrite exhibited a feathery morphology, and the volume fraction of the RA correspondingly increased, as shown in Figure 3.3 and in Figure 3.7. The mechanical properties exhibited by such a microstructure would include lower hardness and lower strength with increased ductility [83]. The most diminished property at this temperature is the yield strength, with only a limited increase in ductility. This clearly indicates that increasing the austempering temperature to the upper ausferritic range for further improvement in ductility is not effective for high-silicon ductile irons.

When toughness was taken as the product of tensile strength by elongation at fracture, it was seen that the maximum toughness values were exhibited by the ADI-330 sample of the GJS 500-14-grade ductile iron among all the samples investigated. In terms of chemical composition, on the other hand, it should be pointed out that increasing the silicon content from 3.7 wt% to 4.3 wt% resulted in a slight increase in the hardness and strength values but at the expense of a more obvious decrease in ductility. Even though both ductile irons are high-silicon grades, the presence of more silicon in the chemical composition results in a lower toughness owing to significantly decreasing ductility.

Figure 3.8 shows the variation of yield strength of both grade austempered ductile irons with respect to the inverse of the square root of the mean ferritic cell size. The figure clearly demonstrates that the yield strength increased with decreasing mean ferritic cell size. It is well known that the strength of a material can be improved by preventing dislocation motion. As the mean ferritic cell size, which is defined as the mean free path of dislocations decreases, there would be more barriers to dislocation motion and thus hardness and strength would increase [76]. A somewhat similar linear relationship between tensile strength and hardness with R^2 of 0.918 can be obtained by fitting a curve over data pairs through the origin, as shown in Figure 3.9. The ratio of tensile strength to hardness on that plot varies in between 3.0–3.43, which increases with decreasing austempering temperature and has an average value of 3.31.

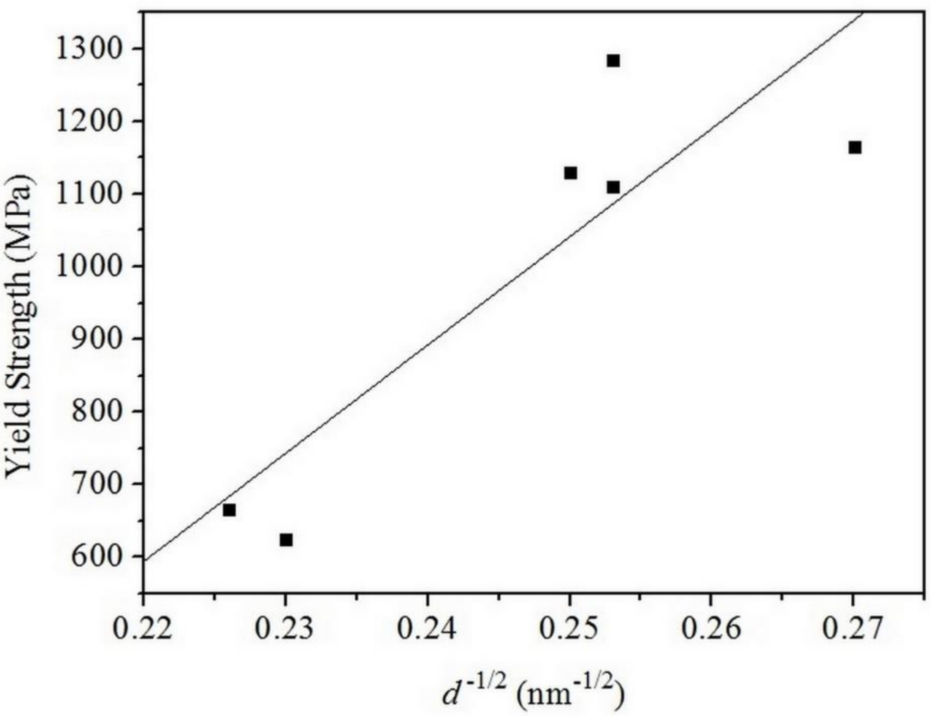

Figure 3.8 : Hall–Petch-type plot showing the variation of yield strength as a function of the inverse of the square root of the mean ferritic cell size (*d*) for all austempered samples.

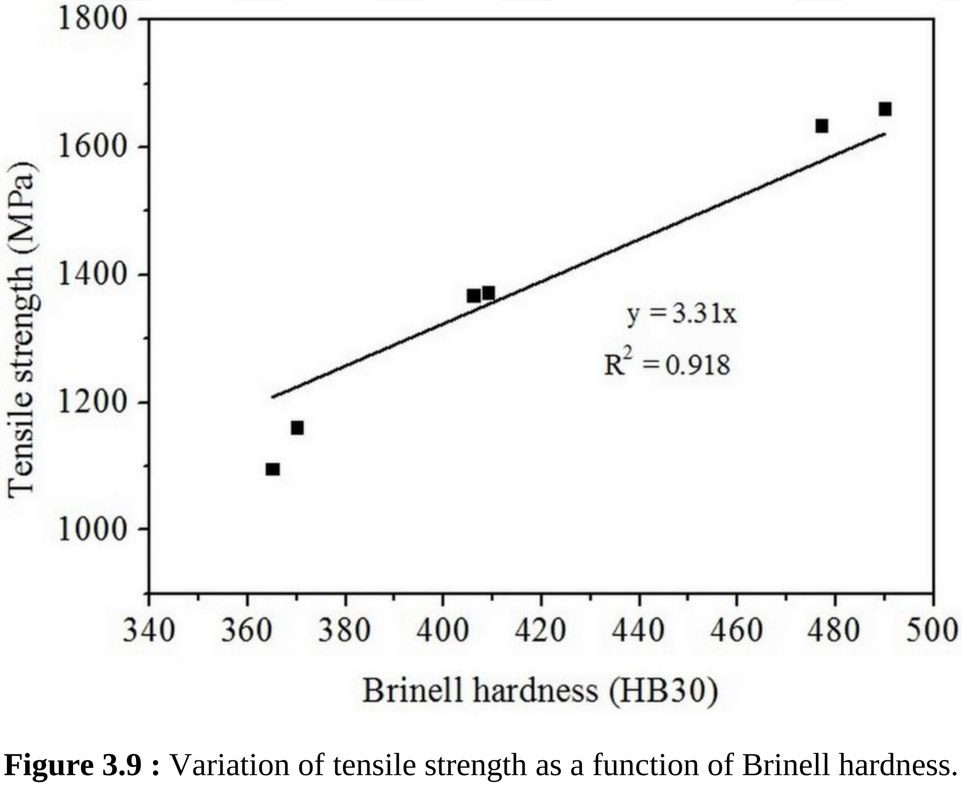

Figure 3.9 : Variation of tensile strength as a function of Brinell hardness.

Figure 3.10 shows variations of the strain-hardening exponent (*n*) with respect to austempering temperature. The variations of elongation at fracture are also included in these figures for comparison. It should be first mentioned that the strain-hardening exponent of both grades of ductile iron is maximum at the lower austempering temperature (270 °C). It then decreases to the minimum value at the mid-austempering temperature (330 °C) and then increases again at the austempering temperature of 390 °C.

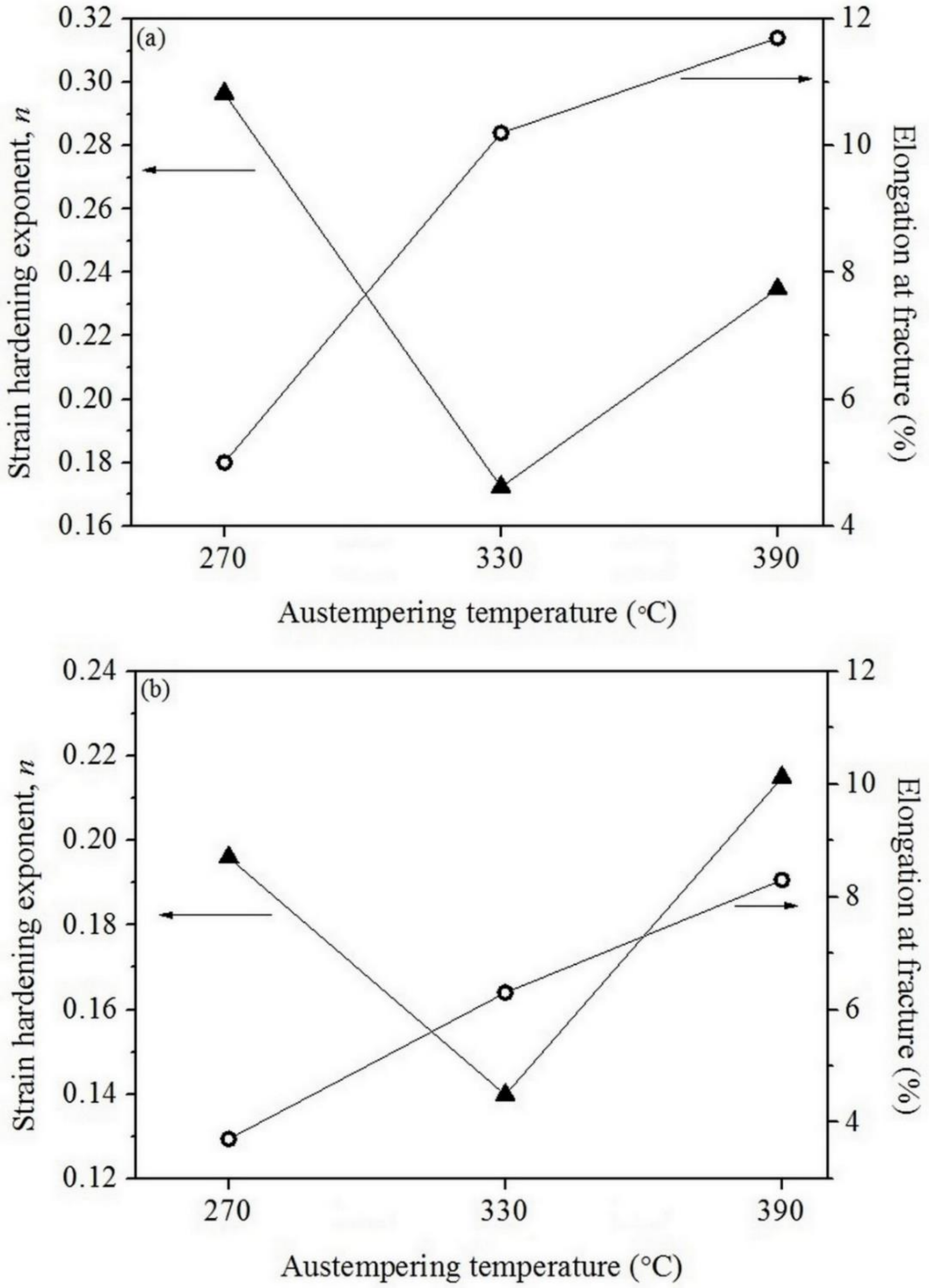

Figure 3.10 : Variation of strain-hardening exponent (*n*) and elongation at fracture with respect to austempering temperature for (a) GJS 500-14- and (b) GJS 600-10-grade ductile irons.

As shown in the present study, the volume fraction of ferrite is high at 270 °C, whereas the volume fraction of RA is low. Because of the high dislocation density within the ferrite [82], interactions between dislocations and carbon atoms are prevalent depending on the high volume fraction of ferrite at the low austempering temperature. Therefore, the strain-hardening exponent values obtained at the low austempering temperature would be high as a result of these interactions. On the other hand, it is shown that the minimum value of the strain-hardening exponent corresponds to an elongation at fracture of approximately 10 % for the GJS 500-14 samples and approximately 6 % for the GJS 600-10 samples. This observation is consistent with that reported by Yang and Putatunda [38], who concluded that further increases in the strain-hardening exponent after exhibiting the minimum value was due to the transformation of RA into martensite. However, the approximately 6% elongation at fracture found for GJS 600-10 is lower than these values, suggesting that a different mechanism might be responsible for increasing the strain-hardening exponent at higher austempering temperatures for samples containing more silicon [84]. It should also be mentioned that the ductile iron grades used in this study have higher amounts of silicon (3.7 wt% and 4.3 wt% for GJS 500-14 and 600-10, respectively) than that used in Ref. 38 (2.48 wt%), resulting in correspondingly higher strain-hardening values. This can be explained by the fact that more silicon reduces the stacking fault energy and contributes to strain hardening [85].

3.3.4 Magnetic properties

Figure 3.11 displays the magnetization (*M–H*) curves of the as-cast (100% ferritic) and austempered samples. The saturation magnetization values of the GJS 500-14 samples were always higher than those of the GJS 600-10 samples. This is true for both the as-cast and austempered samples. Because alloying elements in the chemical composition are capable of decreasing the magnetic moment and consequently the saturation magnetization of iron [80], the difference between the saturation magnetization values of both ductile iron grades is attributed to the difference in their chemical composition [86]. In a similar manner, Nakano and Kawano [87] reported that as the silicon content increased in a ferrite-matrix ductile iron, the magnetic saturation value decreased.

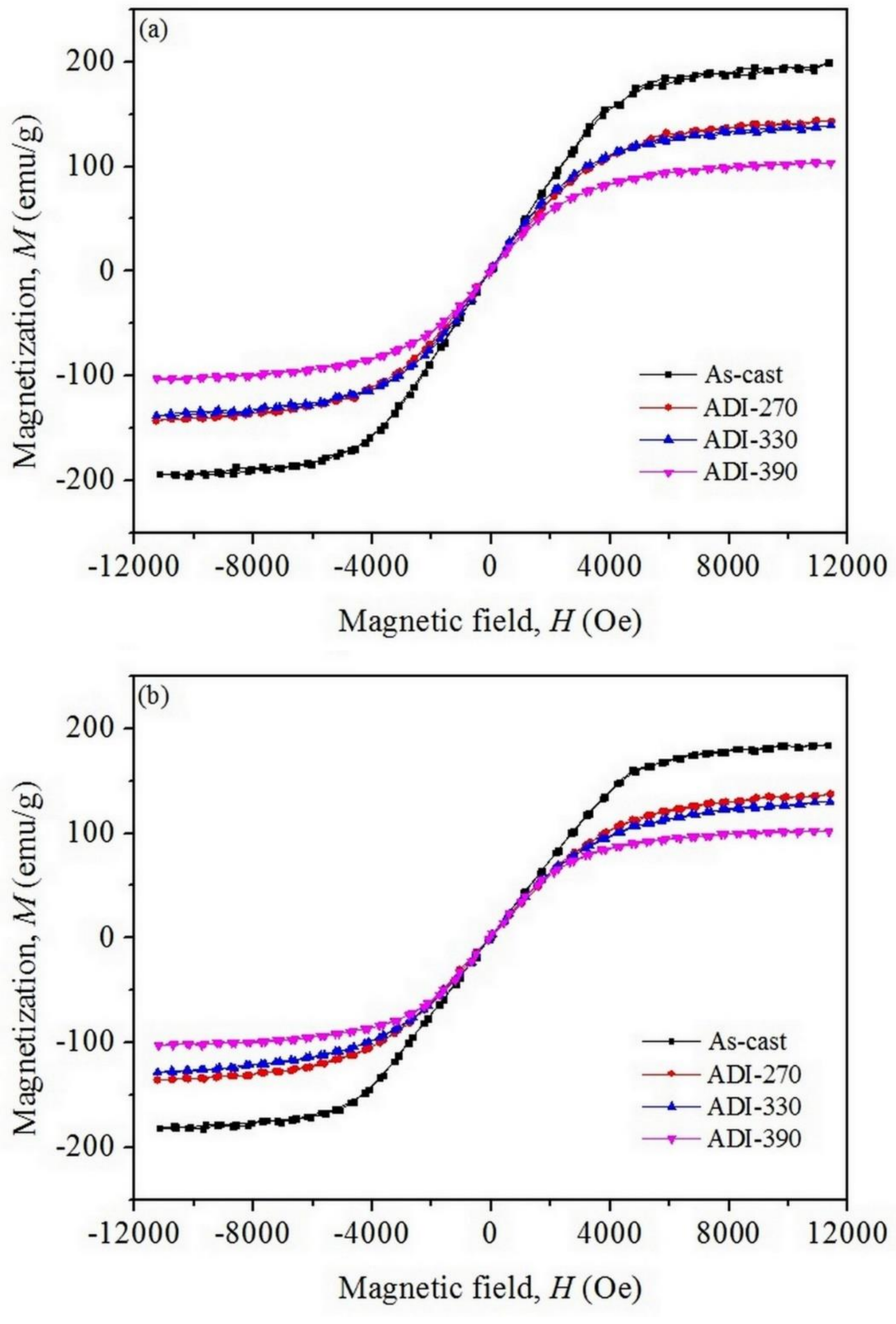

Figure 3.11 : Magnetization (*M–H*) curves of as-cast (100 % ferritic) and (a) GJS 500-14 and (b) GJS 600-10 austempered samples.

On the other hand, saturation magnetization reached a maximum value in the samples containing the highest amount of ferrite (i.e., those austempered at 270 °C) and followed a decreasing trend with increasing temperature, as shown in Figure 3.12. This can be explained by variations in the ferromagnetic (ferrite) and paramagnetic (austenite) phase volume fractions and confirms that the saturation magnetization increases as the ferromagnetic ferrite volume fraction increases [80].

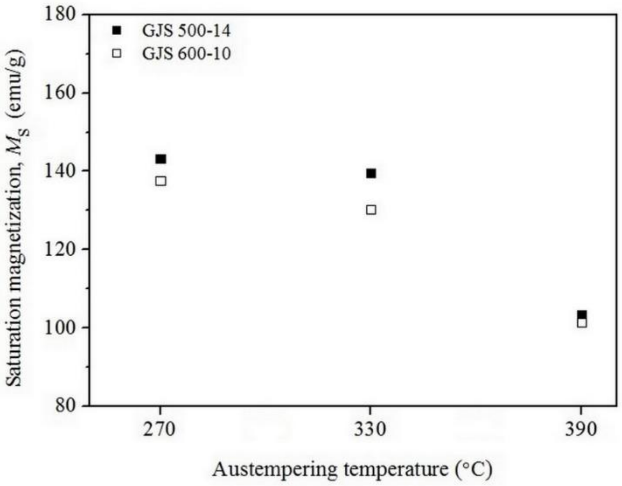

Figure 3.12 : Variation of saturation magnetizations with respect to austempering temperature.

Figure 3.13 shows the variations of remanence (M_r) and mean ferritic cell size (d) with respect to austempering temperature.

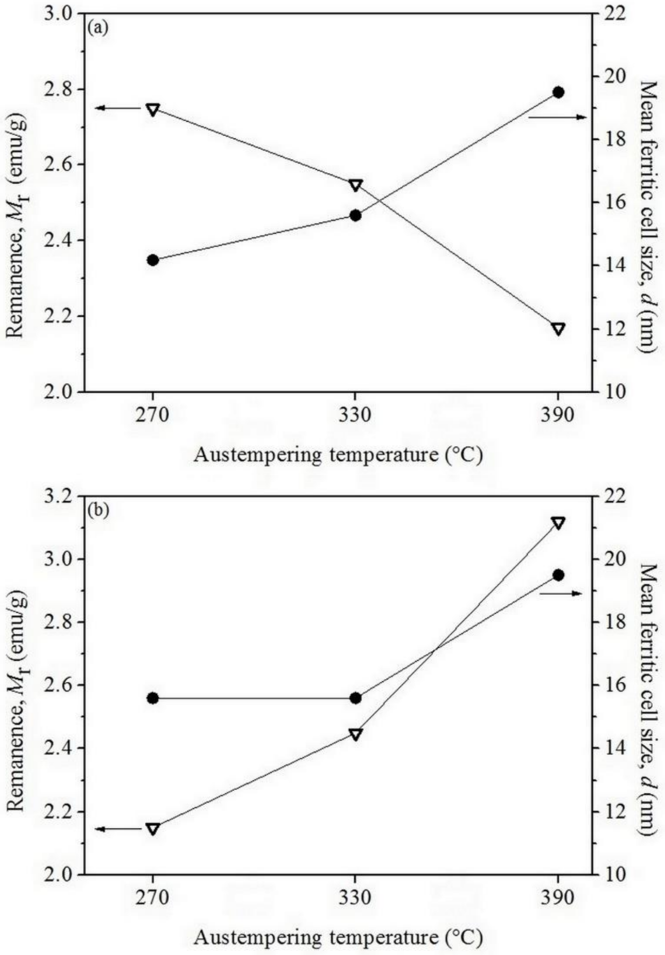

Figure 3.13 : Variations of remanence (M_r) and the mean ferritic cell size (d) with respect to austempering temperature for (a) GJS 500-14- and (b) GJS 600-10-grade ductile irons.

It is obvious that the remanence decreases whereas the mean ferritic cell size increases with increasing austempering temperature for the GJS 500-14 samples. This trend was also reported in studies on the magnetic behavior of supermartensitic stainless steels containing ferromagnetic and paramagnetic phases in different fractions [80]. However, the opposite behavior exists for the GJS 600-10 samples, where both the remanence and the mean ferritic cell size increase with increasing austempering temperature. This contrary behavior suggests that remanence is not a factor that is only controlled by the mean ferritic cell size.

Figure 3.14 shows the variation of coercivity (H_c) with austempering temperature. The variations of mean ferritic cell size and hardness are also included for comparison. Similar to the variation of remanence (in Figure 3.13), the coercivity of the GJS 500-14 samples exhibit an inverse relationship with mean ferritic cell size. These results show that remanence and coercivity are sensitive to microstructural features such as grain size and dislocation density. Because of the growth of the grains, the pinning effect of dislocations on magnetic domain wall movement decreases and thus the coercivity and the remanence increase [72]. On the other hand, it is clear that coercivity and hardness exhibited similar trends, decreasing with increasing austempering temperature for the GJS 500-14 samples. This is consistent with the results of Jiles et al. [88], who found that the coercivity generally increased with increasing hardness in a plain carbon steel. In the GJS 600-10 samples, on the other hand, both the coercivity and the mean ferritic cell size increased as the austempering temperature increased (Figure 3.14), which is similar to the variation of remanence (Figure 3.13).

As shown in Figures 3.13 and 3.14, for a given type of ductile irons, both coercivity and remanence exhibited the similar trend with respect to mean ferritic cell size. In contrast to their inverse relationship with mean ferritic cell size in GJS-500-14 samples, they both increase with increasing mean ferritic cell size in GJS-600-10 samples. Since increased coercivity and remanence are consequences of pinning the magnetic domain walls [89], this behavior is attributed to that more solute atoms (silicon) in the chemical composition of the GJS 600-10 sample can act pinning sites against domain wall motion [72] , and play a more dominant role than the mean ferritic cell size in determining coercivity and remanence. This is especially effective at higher austempering temperature, where the density of dislocations in ferrite is expected to be lower and thus their pinning effect might be minimized.

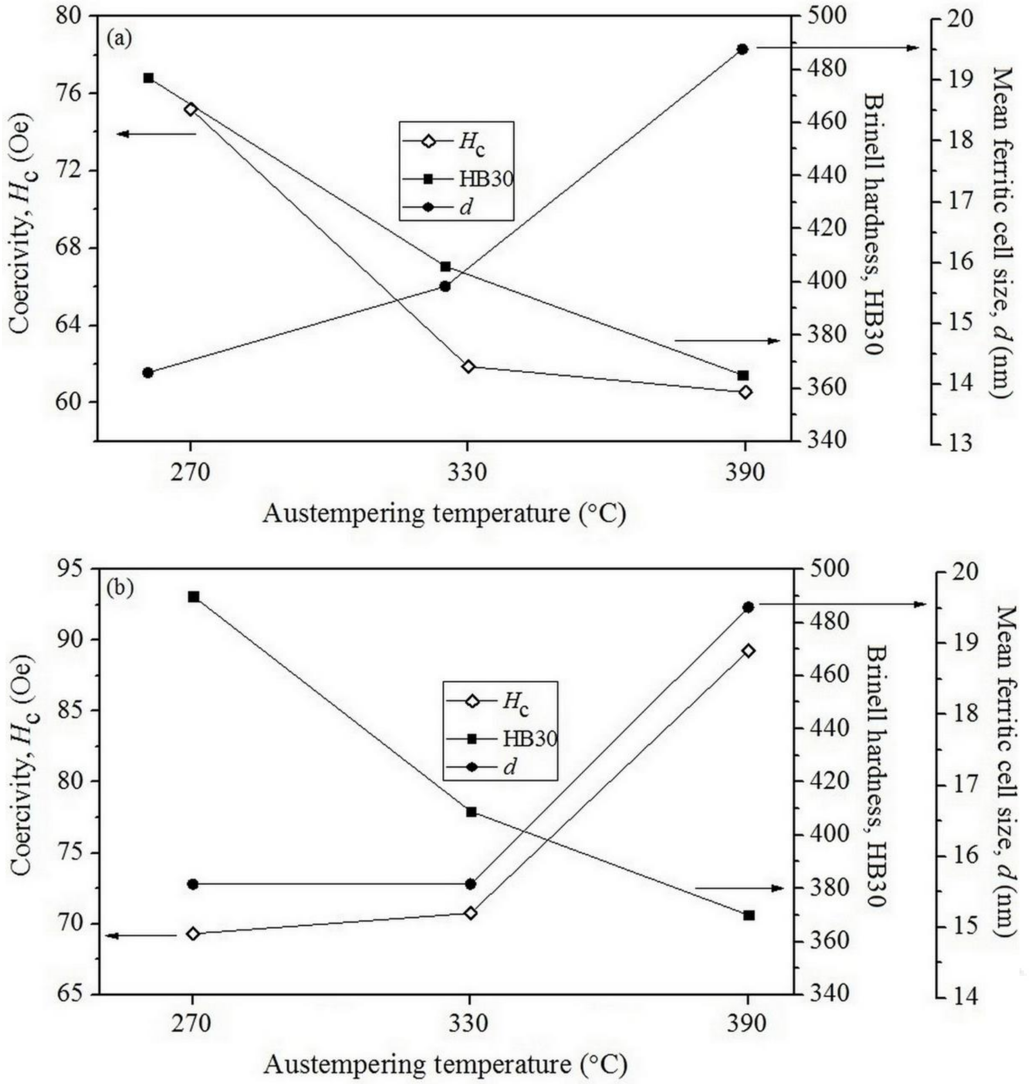

Figure 3.14 : Variation of coercivity, hardness, and mean ferritic cell size with austempering temperature for (a) GJS 500-14- and (b) GJS 600-10-grade ductile irons.

3.4 Conclusions

Austempered high-silicon ductile irons varying in silicon content were investigated through microstructural, mechanical, and magnetic characterization tests, and the following conclusions were drawn:

1. Both grades of high-silicon ductile iron with fully ferritic initial microstructures were successfully austempered to satisfy the minimum mechanical properties specified in BS EN 1564. The mechanical properties of the samples austempered at 270, 330, and 390 °C met the requirements of grades 1400-1, 1200-3, and 900-8, respectively, in the standard.

2. The presence of silicon in the GJS 600-10-grade ductile iron resulted in slightly higher hardness and strength as compared to the GJS 500-14-grade ductile iron but only at the expense of an obvious drop in ductility, which significantly decreases toughness. For this reason, GJS 600-10 should not be a preferred grade in the view point achieving optimum mechanical properties giving high toughness.
3. Austempered high-silicon ductile iron with 3.7 wt% of silicon (GJS 500-14) exhibited more than two times higher strength than the as-cast iron while maintaining at least 10% ductility when austempered at 330 °C. These results correspond to the optimum combination of strength and ductility in terms of the highest toughness obtained in the present study.
4. The volume fraction of the RA estimated by VSM and XRD techniques exhibited similar trends with respect to austempering temperature. However, the VSM measurements produced higher values than those estimated by XRD measurements.
5. The saturation magnetization decreased with increasing austempering temperature owing to the decreasing volume fraction of ferrite. Also, more silicon in the chemical composition of GJS 600-10 slightly reduced the saturation magnetization.
6. Both coercivity and remanence had an inverse relationship with the mean ferritic cell size for GJS 500-14. However, they exhibited a linear relationship for the GJS 600-10-grade ductile irons.

4. CHARACTERIZATION OF FERRITIC DUCTILE IRON SUBJECTED TO SUCCESSIVE ALUMINIZING AND AUSTEMPERING [2]

4.1 Introduction

Solution-strengthened ferritic ductile iron (SSF) is an engineering material that has attracted considerable attention recently due to its low production cost, high ductility, and good castability and machinability compared to conventional ferritic-pearlitic grades [18,90,91]. In this iron, the ferritic matrix is solution-strengthened by silicon contents ranging from 3 to 4.3 wt% instead of pearlite. This provides a higher yield strength and higher ductility with the same tensile strength [17]. Silicon is a graphitizer, and it promotes the formation of a fully ferritic microstructure in ductile iron. To extend the demand and service life of ductile iron components, austempering heat treatment is applied to conventional ductile iron to convert the initial as-cast microstructure into a unique combination of acicular ferrite (α) and retained austenite (γ). Austempered ductile iron (ADI) is gaining popularity because of its improved mechanical and tribological properties and unique microstructure [30,36]. Despite the good mechanical and tribological properties of ADI, its poor corrosion resistance strictly restricts its use in humid and marine environments [92,93].

The corrosion properties of ADI can be improved by surface modification methods such as physical vapor deposition [94] and electroless nickel plating [95]. On the other hand, hot-dip aluminizing (HDA) is a promising alternative to these methods as it requires short time and can be applied to a metallic substrate without the need for sophisticated equipment.

HDA is generally performed by dipping the substrates into molten Al [57]and Al–Si alloys [96] , and results in the formation of various Fe–Al intermetallics along the thickness of the coating. Immersing the substrate into pure Al produces Fe_2Al_5 close to the substrate and $FeAl_3$ close to the surface. Also, a high-temperature diffusion annealing is generally applied following HDA. This annealing allows further interdiffusion between the layers of the coatings, thus facilitating the variation in the type and order of the layers.

---

[2] This chapter is based on the paper "Y. Yürektürk, M. Baydoğan, Characterization of ferritic ductile iron subjected to successive aluminizing and austempering, Surf. Coat. Technol. 347 (2018) 142–149, https://doi.org/10.1016/j.surfcoat.2018.04.083."

Previous research has mostly focused on the characterization and transformation kinetics of intermetallics formed during aluminizing and subsequent annealing. Their effects on the oxidation and corrosion resistance of the substrate have also been studied [97–99]. In addition, some studies have explored the additional benefits of aluminide layers to extend aluminizing into various industrial areas. For example, Jiang et al. [100] used aluminizing in combination with galvanizing to modify steel in the fabrication of aluminum/iron bimetallic composites and obtained a more uniform and compact layer at the aluminum-iron interface compared to that obtained without galvanizing and aluminizing. Jamnapara et al. [101] performed plasma and thermal tempering of P91 steel aluminized in Al–7Si at 720 °C. Plasma tempering produced a stable α-Al_2O_3 layer on the steel surface, while thermal tempering resulted in the formation of a θ-Al_2O_3 layer. They stated that the α-Al_2O_3 layer on the aluminized P91 steel is a promising candidate to protect the surface from attack by flowing Pb–17Li in the thermal blanket module of fusion reactors.

HDA can be directly applied to ductile iron with initial as-cast microstructures [51,52]. However, when HDA is applied to an austempered sample, the ausferritic microstructure, which is produced by austenitizing at 840–975 °C followed by austempering at 250–400 °C, may deteriorate. As a result, the good mechanical properties of ADI are lost. Therefore, we propose that austempering should be performed after HDA to avoid any loss in the mechanical properties. Therefore, this sequence was followed in the present study to improve the corrosion resistance of ADI by maintaining its ausferritic microstructure. Another major finding was that this process protected the iron surface from decarburization and scaling without the need for a protective atmosphere during austenitizing.

4.2 Experimental Procedure

4.2.1 Sample preparation

Disk-shaped SSF GJS-500-14 samples with a diameter of 15 mm and thickness of 5 mm were cut from cast round cylindrical bars. The chemical composition of the GJS-500-14 ductile iron samples was as follows (in wt%): 3.3 C, 3.7 Si, 0.2 Mn, 0.029 P, 0.007 S, 0.05 Mg, and balance Fe. Prior to HDA, the samples were ground using #800 grit SiC abrasive papers, ultrasonically washed with acetone, and completely dried in air at room temperature, and then treated with a phosphoric acid solution to destroy the oxide layer on the surface.

4.2.2 Hot-dip aluminizing

Similar to the method presented in Ref. [102], aluminum (99.9 wt%) was melted in a graphite crucible placed in a resistance furnace, and the aluminizing was performed at 750 °C for 5 min to form a thick aluminide coating on the substrate. The temperature was monitored using a Ni–NiCr thermocouple that was placed directly in the molten aluminum to ensure that the desired temperatures were maintained. The aluminum bath was covered with a flux material to prevent the oxidation of the surface before and after the hot-dipping process. The samples fixed by a stainless steel wire were immersed into the molten aluminum and then pulled out from the molten bath. They were finally air cooled to room temperature, and no shedding of the coating layer was observed after cooling.

4.2.3 Austempering

The aluminized samples were heated to an austenitizing temperature of 975 °C at a heating rate of <12 °C/s and held at this temperature for 2 h. The austenitized samples were rapidly transferred to a salt bath containing Petrofer® AS135 commercial annealing salt and austempered at 270 °C, 330 °C, and 390 °C for 1 h. In the last step of the heat treatment, the samples were removed from the bath and cooled to room temperature in air. The temperature was measured and controlled by a Ni–NiCr thermocouple during the austenitizing and austempering steps. The samples were represented as ADI-270, ADI-330, and ADI-390 depending on their austempering temperatures.

4.2.4 Structural characterization

Qualitative phase analysis of the coatings was performed by X-ray diffraction (XRD, GBC MMA-027) using Cu-Kα ($\lambda = 0.154$ nm) radiation. The accelerating voltage and applied current were 35 kV and 28.5 mA, respectively. The samples were scanned over a 2θ range of 20°–90° in steps of 0.02° at a scanning speed of 1° min^{-1}. The obtained XRD patterns were then analyzed by software (X'pert HighScore Plus) to identify the peak positions. A scanning electron microscopy (SEM) system (JEOL JSM 6335 F

FEG) equipped with an energy dispersive spectrometry (EDS) system (JEOL NeoScope JCM-6000) was used to examine the surface morphology of the coatings and elemental distribution of the phases. The cross-sectional morphology of the coatings and the microstructures of the samples were examined by field-emission SEM (FE-SEM, Zeiss Ultra Plus) after etching with 4 vol% nital solution. The elemental analysis of the coatings was performed using an energy dispersive X-ray spectroscopy (EDX) system (Bruker XFlash 5010) integrated into the SEM system. Quantitative phase analysis of the cross-section of the samples was conducted using XRD with Cu-Kα radiation over a 2θ range of 60°–105° in steps of 0.05° and at a scanning speed of 1° min^{-1} to estimate the volume fraction of ferrite (X_α) and austenite (X_γ) utilizing the integrated intensities of the (200) and (220) planes of body-centered cubic (bcc) ferrite and the (220) and (311) planes of face-centered cubic (fcc) austenite according to the direct comparison method [103].

4.2.5 Hardness and tensile tests

Hardness measurements were performed at the cross sections of the coatings and the substrates by a Zwick universal hardness tester (Roell ZHU 2.5) with a diamond Vickers indenter. During indentation, the maximum test load was 100 g with a dwell time of 20 s. At least 5 measurements were taken for each sample, and the results were averaged.

Duplicate tensile tests of the samples were performed with a gage length of 25 mm using a universal servo-hydraulic test machine (Instron 8801) according to the ASTM E8/E8M standard, and the average results were reported. All tests were conducted at a cross-head speed of 2 mm min^{-1} at room temperature.

4.2.6 Corrosion tests

Anodic potentiodynamic polarization corrosion tests were performed in a 3.5 wt% NaCl solution to simulate an aggressive chloride-containing aqueous environment. The samples were placed in a potentiostat/galvanostat apparatus (EGMA 273), and a standard saturated calomel electrode (SCE) was used as the reference electrode and platinum was used as the counter or auxiliary electrode. The contact area in all cases was 1 cm^2, and the temperature was maintained at 25 °C during the corrosion tests. The electrode potential was raised from −1.2 V to 0.4 V at a scanning rate of 1 mV/s. All polarization curves were obtained after 20 min of free immersion of the samples to ensure a steady open-circuit potential. The corrosion parameters were evaluated by Tafel extrapolation of the polarization curve.

Salt spray corrosion tests (SSCTs) were performed in a chamber containing a 5 wt% NaCl solution for 48 h in accordance with the ISO 9227 standard. The pH was maintained between 6.5 and 7.2, and the temperature was maintained at 35 ± 2 °C during the corrosion tests. After the SSCTs, the surface morphology of the samples was examined by SEM (Hitachi TM-1000). Following the SSCTs, the corrosion products were completely removed by chemical cleaning according to the ISO 8407 standard. The weight loss due to corrosion was measured using an analytical balance with a precision of 0.1 mg. Cross-sectional SEM images of the samples were also obtained after the chemical cleaning.

4.3 Results and Discussion

4.3.1 Formation of intermetallic layers between solid iron and molten aluminum

Figure 4.1 shows (a) the surface XRD patterns and (b) cross-sectional SEM micrographs of the hot-dip aluminized sample before austempering. From the XRD analysis, it was found that the coating was composed of Al (JCPDS No. 085-1327), $FeAl_3$ (JCPDS No. 050-0797), and Fe_2Al_5 (JCPDS No. 029-0043) phases. These phases were also identified by EDX analysis shown in the inset of Figure 4.1. The phases could be seen in the cross-sectional SEM images, with a top layer of Al (with $FeAl_3$), middle layer of $FeAl_3$, and inner layer of Fe_2Al_5. The tongue-like morphology of Fe_2Al_5 was due to its preferential growth on the substrate [96].

EDX analysis of the layers revealed the presence of a very small amount of silicon in the $FeAl_3$ and Fe_2Al_5 layers (0.84 at% in $FeAl_3$ and 2.16 at% in Fe_2Al_5). Therefore, no Fe–Al–Si or Al–Si compounds could not be detected. This was attributed to the lower solid diffusion rate of Si than that of Fe during inter-diffusion reactions between the substrate and molten Al; hence, it was difficult to form Al–Si compounds after HDA in a pure Al bath [52]. As shown in Figure 4.1, the thickness of the Fe_2Al_5 layer (33–43 μm) was greater than that of the $FeAl_3$ layer (8–23 μm) due to faster growth rate of orthorhombic Fe_2Al_5 along its c-axis, where 30% of its vacancies are occupied. These vacancies provided suitable diffusion paths, contributing to the faster growth rate of Fe_2Al_5 [104,105].

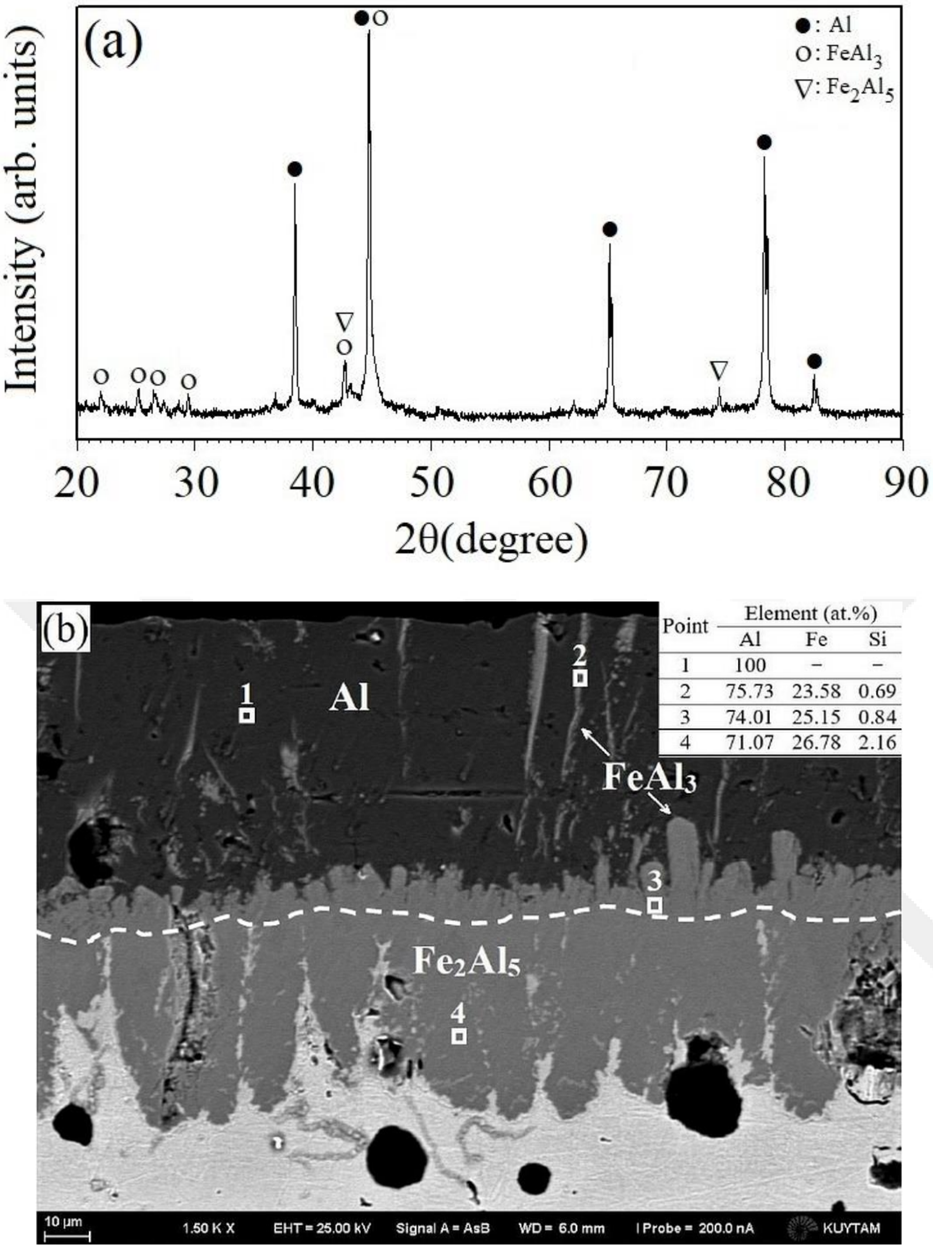

Point	Element (at.%)		
	Al	Fe	Si
1	100	–	–
2	75.73	23.58	0.69
3	74.01	25.15	0.84
4	71.07	26.78	2.16

Figure 4.1 : Surface XRD pattern (a) and cross-sectional SEM micrograph (b) of the hot-dip aluminized sample before austempering.

4.3.2 Evolution of intermetallic layers and substrate microstructures by austempering

Figure 4.2 shows the XRD patterns of the coatings after austempering at various temperatures. It should be noted that all austempered samples, regardless of the austempering temperature, showed similar phases: Al_2O_3 (JCPDS No. 088-0107), Fe_2Al_5 (JCPDS No. 029-0043), $FeAl_2$ (JCPDS No. 034-0570), FeAl (JCPDS No. 001-1257), and Fe (JCPDS No. 085-1410).

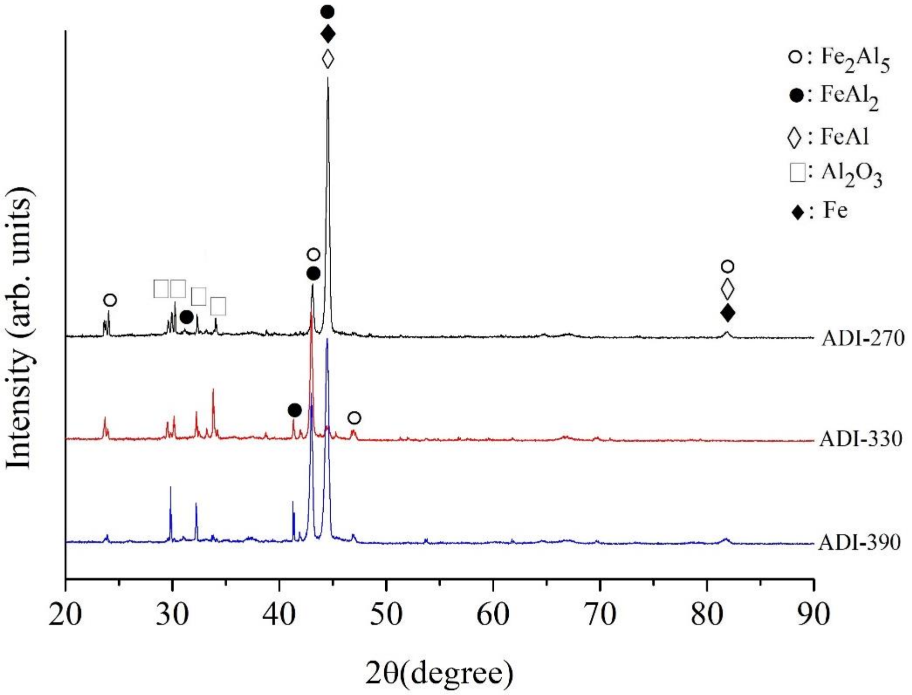

Figure 4.2 : XRD results of coatings after austempering.

Surface elemental mapping (O, Al, and Fe) of the ADI-270 sample as a representative example for the austempered samples is shown in Figure 4.3. Signals from O and Al were attributed to the formation of the Al_2O_3 layer on the surface, confirming the XRD results shown in Figure 4.2. The Al_2O_3 layer was formed from the Al top layer in the coating by the outward diffusion of Al [106] during high-temperature austenitizing. As a barrier layer formed on the aluminide coating, the Al_2O_3 layer could protect the substrate against aggressive attacks in oxidizing and corrosive environments [107,108].

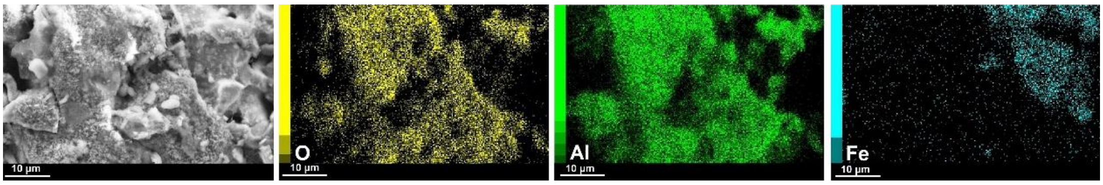

Figure 4.3 : Surface elemental mapping of ADI-270 sample.

Figure 4.4 shows the cross-sectional SEM micrographs of the coatings after austempering at various temperatures. Austenitizing at 975 °C for 2 h resulted in the transformation of the intermetallics formed during HDA. The cross-sectional SEM-EDX analysis revealed the presence of a thin Al_2O_3 layer on the surface and Fe_2Al_5, $FeAl_2$, FeAl, and α-Fe phases, as confirmed by the XRD results of Figure 4.2. The coating layers exhibited similar morphologies regardless of the austempering temperature. They did not contain any discontinuities at their intersections and therefore well adhered to each other. The Al top layer formed during HDA was transformed to Fe_2Al_5 due to the inward diffusion of Al toward the substrate [106] during austenitizing. According to Cheng and Wang [62], austenitizing at 750 °C for 15 min was sufficient for the complete transformation of the Al top layer into single-phase Fe_2Al_5. Although $FeAl_3$ grew simultaneously with Fe_2Al_5 [63], no Al-rich $FeAl_3$ phase was detected in the aluminide layer. This could be attributed to the preferential growth of Fe_2Al_5, which inhibited the formation of $FeAl_3$ [63,99]. The enhanced inter-diffusion during austenitizing also formed $FeAl_2$, FeAl, and α-Fe phases. These phases were located between $FeAl_2$ and the ADI substrate. The formation of the α-Fe layer was due to the stabilization of the bcc ferrite by aluminum, which transformed the austenitic microstructure into α-Fe [109]. Therefore, the α-Fe layer did not transform into ausferrite during austempering, as shown in the inset in Figure 4.4. The total thickness of the coating was about 100 µm after HDA and significantly increased to about 300 µm after austenitizing. Al content in these layers decreased due to the outward diffusion of iron, resulting in the formation of high Fe content layers (FeAl and α-Fe) with a total thickness of 185 µm [62]. Although the formation of an iron-rich intermetallic Fe_3Al layer during diffusion annealing of 0.44% C steel at 1000 °C was observed by Kobayashi and Yakou [63], no Fe_3Al was detected in the present study due to lower austenitizing temperature used (975 °C). Therefore, the coating layer after austenitizing only consisted of Fe_2Al_5 and $FeAl_2$ as the Al-rich intermetallics in addition to the FeAl and α-Fe layers. All structures formed after austenitizing exhibited an increasing Al content from the surface to the ADI substrate. From the viewpoint of austempering temperatures varying between 270 °C and 390 °C, there was no remarkable difference in the order and type of the layers of the coated ADI samples (Figure 4.4). This implied that the main factor determining the coating structure was aluminizing and austenitizing temperatures, which were significantly higher than the austempering temperatures, and further diffusion in the austempering temperature range (270 °C–390 °C) was difficult.

On the other hand, some Kirkendall pores were observed within the $FeAl_2$ layer in the coated samples as shown in Figure 4.4. These pores were formed as a result of the different diffusion coefficients of Al and Fe at the austenitizing temperature. Some cracks were also observed within the coatings.

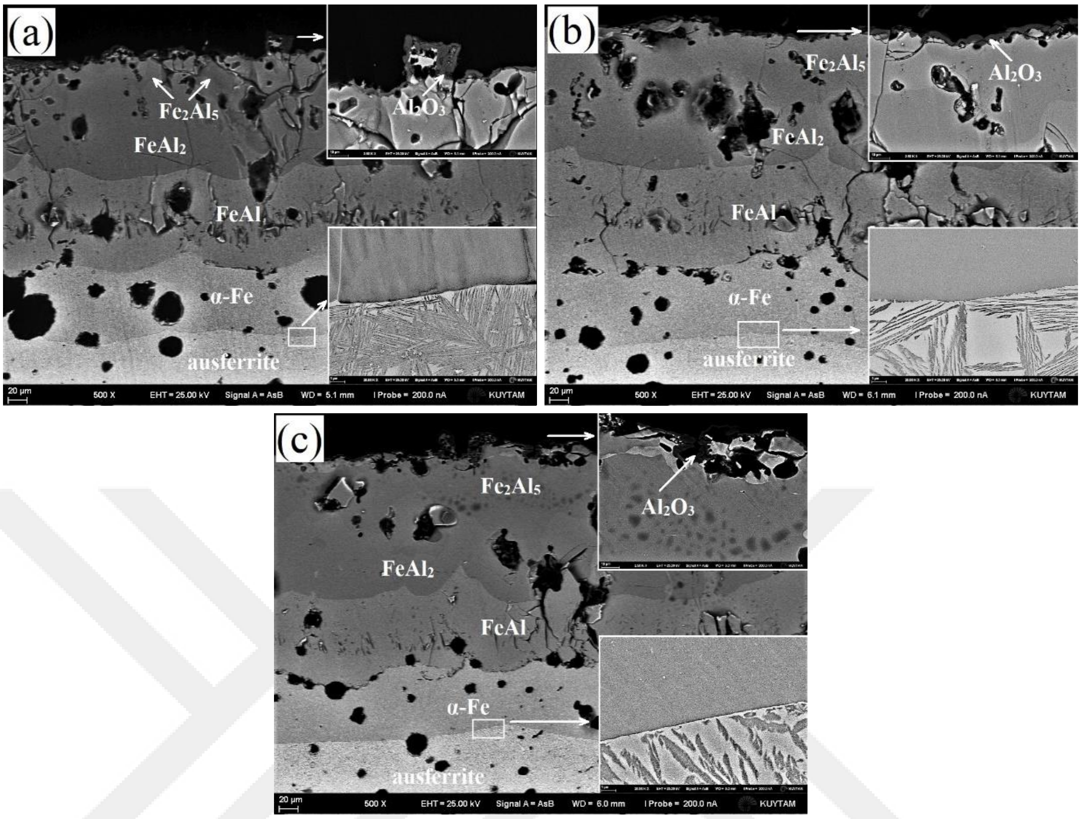
(a)
Fe2Al5
FeAl2
FeAl
α-Fe
ausferrite
Al2O3
20 µm 500 X EHT = 25.00 kV Signal A = AsB WD = 5.1 mm I Probe = 200.0 nA KUYTAM
(b)
Fe2Al5
FeAl2
FeAl
α-Fe
ausferrite
Al2O3
20 µm 500 X EHT = 25.00 kV Signal A = AsB WD = 6.1 mm I Probe = 200.0 nA KUYTAM
(c)
Fe2Al5
FeAl2
FeAl
α-Fe
ausferrite
Al2O3
20 µm 500 X EHT = 25.00 kV Signal A = AsB WD = 6.0 mm I Probe = 200.0 nA KUYTAM

Figure 4.4 : Cross-sectional SEM micrographs after austempering at various temperatures: (a) ADI-270, (b) ADI-330, and (c) ADI-390.

The cracks occurred during cooling from the diffusion annealing temperature as a result of the difference in the thermal expansion coefficients of the intermetallics. Wang et al. [110] reported that the stress in the Fe_2Al_5 layer after HDA was compressive in nature; therefore, no cracking was observed along the thickness of the coating. However, this stress turned into tensile stress after the high-temperature corrosion test and cracks perpendicular to the surface were easily formed during cooling. In Figure 4.4, the cracks were mainly initiated in the $FeAl_2$ and Fe_2Al_5 layers and propagated toward the FeAl layer. It is known that the Fe_2Al_5 and $FeAl_2$ layers are brittle; therefore, it was expected that the high temperature gradient during cooling from the austenitizing temperature (975 °C) to the austempering temperature (270 °C–390 °C) was responsible for the crack formation because of the brittle nature of the Al-rich intermetallics in combination with the tensile stress acting on them. Even though the cracks and pores could reduce the surface integrity by some degree, it was expected that the coating layer could remain protective because the cracks and pores were limited to the top section of the coating within the Al-rich intermetallics ($FeAl_2$ and Fe_2Al_5) and did not extend beyond the tougher α-Fe layer of the coating.

Figure 4.5 shows the cross-sectional elemental mapping of the ADI-270 sample. Elemental distribution along the thickness of the coating revealed decreasing Al content from the surface toward the substrate, while the Fe content increased outward. Si signals were associated with its high content in the substrate, and O signals close to the surface indicated the oxide layer at the surface. Therefore, these elemental mapping results agreed with the previous SEM-EDX analysis (Figure 4.4), indicating the type of layers within the coating.

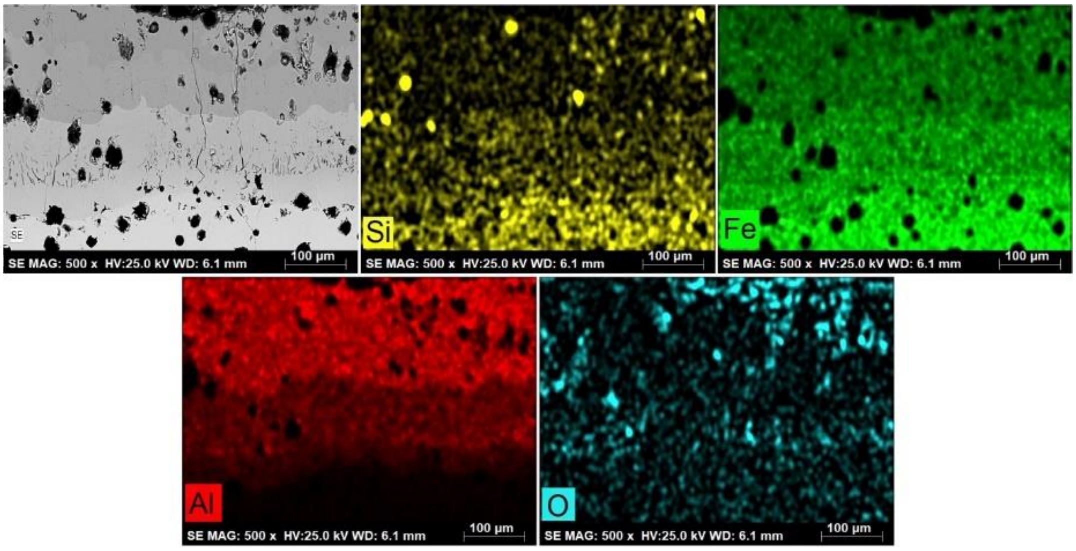

Figure 4.5 : Cross-sectional elemental mapping of ADI-270 sample.

Figure 4.6 shows the high-magnification FE-SEM micrographs of the substrate (ADI) austempered at various temperatures. The microstructures consisted of bcc ferritic acicular laths (α) and fcc retained austenite (γ). The ferrite became progressively coarser as the austempering temperature increased from 270 °C to 390 °C. The width of the ferritic lamellae, λ(α), was measured from the SEM micrographs shown in Figure 4.6 and was found to be in the range of 40–65 nm for ADI-270, 80–150 nm for ADI-330, and 200–300 nm for ADI-390. The retained austenite volume fractions of ADI-270, ADI-330, and ADI-390 were estimated by XRD to be 15.7%, 21.7%, and 31.1%, respectively. At low austempering temperatures, the nucleation rate of ferrite was high because of the higher supercooling, whereas the diffusion rate of carbon was low, so the growth rate of ferrite was low. Hence, a high ferrite nucleation rate and low ferrite growth rate increased the number of ferritic lamellae, reduced the width of the lamellae, and decreased the volume fraction of the retained austenite [76].

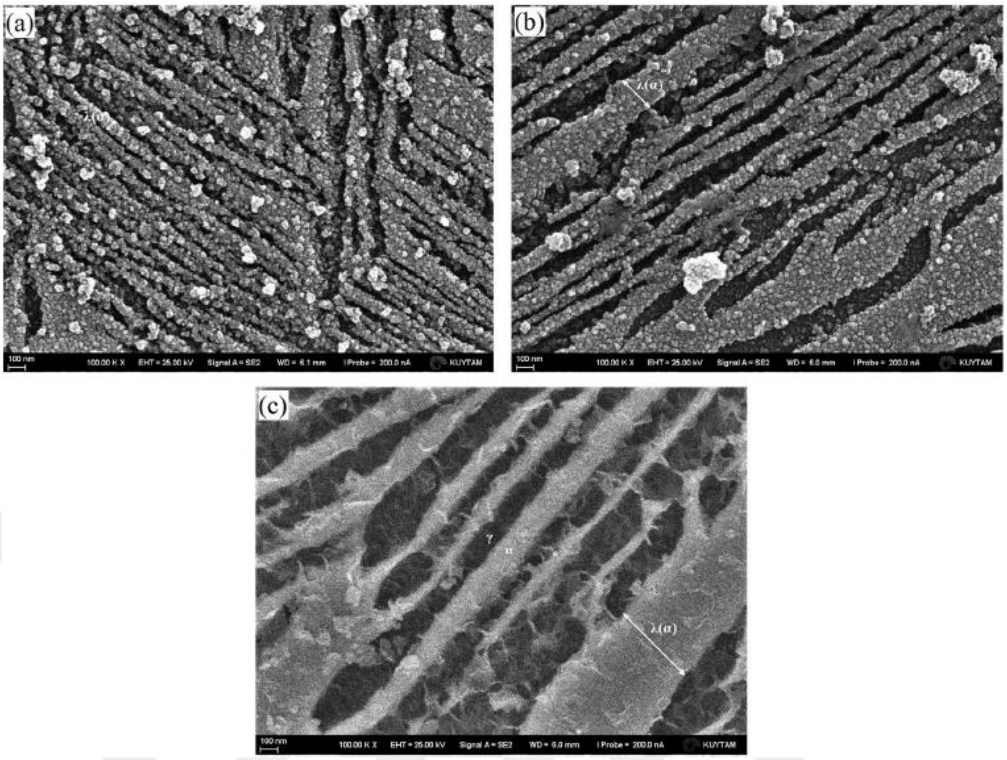
(a)
λ(α)
100 nm
100.00 K X EHT = 25.00 kV Signal A = SE2 WD = 6.1 mm I Probe = 200.0 nA KUYTAM
(b)
λ(α)
100 nm
100.00 K X EHT = 25.00 kV Signal A = SE2 WD = 6.0 mm I Probe = 200.0 nA KUYTAM
(c)
γ
α
λ(α)
100 nm
100.00 K X EHT = 25.00 kV Signal A = SE2 WD = 6.0 mm I Probe = 200.0 nA KUYTAM

Figure 4.6 : High-magnification FE-SEM micrographs of substrate after austempering at various temperatures: (a) ADI-270, (b) ADI-330, and (c) ADI-390.

4.3.3 Mechanical properties

The hardness of the Fe_2Al_5, $FeAl_2$, FeAl, and α-Fe phases were measured to be 1035 ± 112, 985 ± 91, 495 ± 83, and 366 ± 27 $HV_{0.1}$, respectively. It was clear that the Al-rich phases showed higher hardness than the Fe-rich phases. The hardness values were consistent with previous results [111,112]. Although the Fe_2Al_5 and $FeAl_2$ phases exhibited high hardness, low fracture toughness due to their brittle nature was a problem [63,109]. On the other hand, the more ductile FeAl phase improved the fracture toughness and interface strength of the aluminized steel [109]. Therefore, the transformation of Al-rich intermetallics ($FeAl_3$, Fe_2Al_5) to FeAl-type Fe-rich intermetallics after austempering was better both in terms of interface strength and fracture toughness.

Table 4.1 lists the mechanical properties of the aluminized samples in the as-cast and austempered conditions. The hardness and strength values are inversely proportional to ductility in general. It was clear that the austempering process significantly improved the hardness of ductile iron, as expected.

Table 4.1 : Mechanical properties of samples.

Mechanical property	Samples			
	As-cast	ADI-270	ADI-330	ADI-390
Substrate hardness ($HV_{0.1}$)	238 ± 22	685 ± 61	530 ± 31	455 ± 38
Yield strength (MPa)	470 ± 11	1114 ± 34	922 ± 16	655 ± 29
Tensile strength (MPa)	646 ± 18	1321 ± 45	1057 ± 37	805 ± 22
Elongation at fracture (%)	16.1 ± 1.7	10.1 ± 0.9	11.9 ± 1.1	15.2 ± 1.8

The mechanical properties of the aluminized samples austempered at 270, 330, and 390 °C satisfied the requirements of grades 1200-3, 900-8, and 800-10, respectively, specified in the BS EN 1564 standard. When comparing the mechanical properties of aluminized ductile iron obtained in the present study to those obtained in our previous study on ductile iron without aluminizing [113], it was found that the hardness and strength values and ductility were almost unchanged in the as-cast condition. On the other hand, the strength values decreased slightly but the ductility increased in the austempered condition. This could be because there were more ductile phases (FeAl, α-Fe) in the coating structure (Figure 4.4) than brittle phases (Fe_2Al_5, $FeAl_2$); therefore, the ductility of the samples was positively affected by the FeAl and α-Fe phases in the coating structure, which negatively affected the strength of the samples. The elongation at fracture increased at the expense of yield strength and tensile strength with increasing austempering temperature. This was related to the previously described microstructural behavior: increased retained austenite volume fraction as well as coarsening of the microstructure with increasing austempering temperature decreased the strength but increased the ductility. It is well known that the strength of a material can be improved by inhibiting dislocation motion. As the width of the ferritic lamellae $\lambda(\alpha)$, which identifies the mean ferritic free path of mobile dislocations, decreases, the dislocation motion is inhibited and the hardness and strength increase [76,114].

4.3.4 Corrosion properties

Figure 4.7 shows the potentiodynamic polarization curves of the examined samples. Anodic and cathodic Tafel constants (β_a and β_c), corrosion potential (E_{corr}), and corrosion current density (i_{corr}) estimated by the extrapolation of the Tafel plots are listed in Table 4.2.

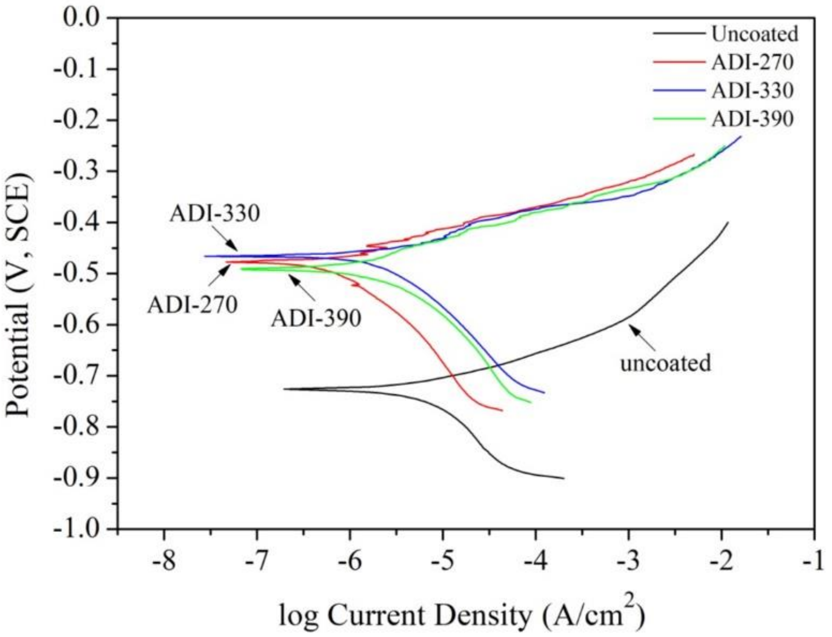

Figure 4.7 : Potentiodynamic polarization curves of uncoated and coated samples in 3.5 wt% NaCl solution.

Moreover, the polarization resistance (R_p) values of the samples (Table 4.2) were calculated according to the Stern–Geary method [115]. As shown in Table 4.2, the E_{corr} value of the coated samples was considerably higher than that of the uncoated sample. This indicated that the corrosion resistance of the coated samples was better, as a higher E_{corr} value implied a more stable electrode potential [116]. Also, the coated samples exhibited significantly lower i_{corr} values than the uncoated sample. The electrode potentials and i_{corr} values of the austempered samples were close to each other and did not show a systematic trend with respect to the austempering temperature. Furthermore, the magnitude of the R_p value, which is inversely proportional to the corrosion rate [92], was higher for the coated samples than for the uncoated sample. Consequently, the coated samples exhibited better corrosion resistance than the uncoated sample, as confirmed by the E_{corr}, i_{corr}, and R_p values. As shown previously [92,117], graphitic corrosion is a common corrosion mechanism of ductile iron. Graphite nodules dispersed uniformly throughout the iron matrix act as cathodic areas with respect to the surrounding matrix, which acts as the anode. As a result, the matrix around the nodules is severely corroded. On the other hand, because graphite nodules are not directly exposed to the corrosive environment in the case of coated samples, graphitic corrosion was not expected to be the driving mechanism of corrosion in the coated samples.

Table 4.2 : Results of potentiodynamic polarization tests applied to uncoated and coated samples.

Sample	β_a (V_{SCE}/decade)	β_c (V_{SCE}/decade)	E_{corr} (V_{SCE})	i_{corr} ($\mu A/cm^2$)	R_p ($k\Omega\ cm^2$)
Uncoated	0.062	0.163	−0.734	17.3	3.457
ADI-270	0.054	0.158	−0.485	0.8	20.558
ADI-330	0.046	0.135	−0.472	2.3	7.091
ADI-390	0.057	0.121	−0.493	1.4	8.561

The findings of the potentiodynamic polarization tests were further confirmed by SSCTs. Figure 4.8 shows the surface SEM micrographs with XRD patterns of (a) the uncoated and (b) ADI-270 samples after a 48-h SSCT.

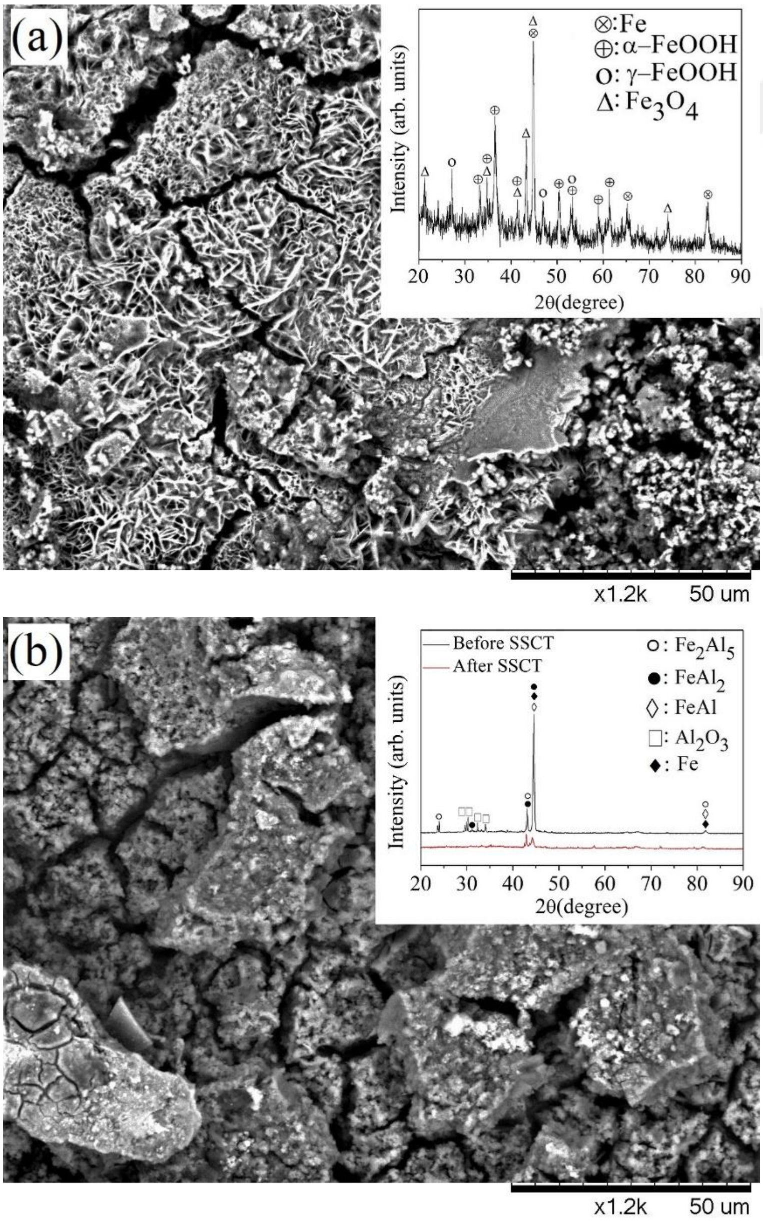

Figure 4.8 : Surface SEM micrographs with XRD patterns of (a) uncoated and (b) ADI-270 samples after 48-h SSCT.

Here it should be mentioned that there was a large amount of white corrosion products accumulated on the surface of the uncoated sample and the morphologies of these corrosion products exhibited a porous appearance. From the surface XRD patterns (Figure 4.8) of the uncoated sample, we found that the rust layer mainly consisted of α-FeOOH (goethite), γ-FeOOH (lepidocrocite), and Fe_3O_4 (magnetite), which could be confirmed by the sharp structures (goethite), flattened areas (magnetite), and flowery structures with sandy crystals (lepidocrocite) observed in the surface SEM micrograph shown in Figure 4.8 [118]. On the other hand, the coated sample surface exhibited some corrosive micro-cracks, white and black corrosion products with cavities and pits. With the exposure of the coated sample to salt spray, the relative intensities of the peaks decreased compared to those before the salt spray test. This could be explained by the fact that Fe dissolution from the coating due to the neutral pH conditions associated with a high chloride concentration could result in the formation of cavities. Pitting corrosion could also be attributed to the formation of Al_2O_3 in the vicinity of the pits owing to the corrosion of the aluminum-rich phases (Fe_2Al_5, $FeAl_2$) [119].

Figure 4.9 shows a cross-sectional SEM micrograph of the ADI-270 sample after complete removal of the corrosion products from the surface by chemical cleaning.

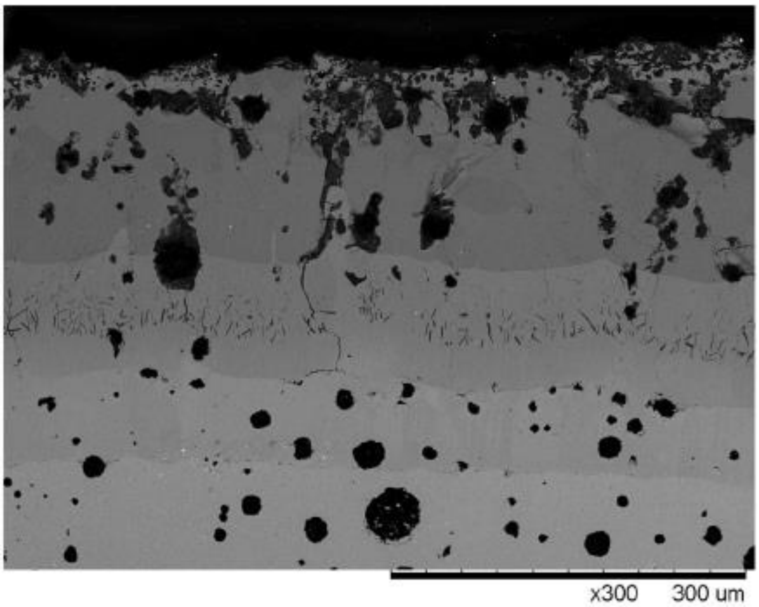

Figure 4.9 : Cross-sectional SEM micrograph of ADI-270 sample after complete removal of corrosion products from the surface.

The corrosion products penetrated up to a thickness of approximately 55 μm in the coating and moved inward through the cracks present on the coating before corrosion.

On the other hand, the weight losses (×10^{-4}, g/mm^2) of the uncoated and coated samples were measured to be 8.85 ± 0.52 and 4.34 ± 0.33, respectively, after complete removal of the corrosion products from their surfaces by chemical cleaning. It was verified that the corrosion experiments showed that the SSCTs showed a tendency similar to that of the potentiodynamic polarization tests. Although the coated sample had some cracks in its structure, ADI substrate could be protected against corrosion because of the aluminide layer acting as a sacrificial anode in Cl^--bearing environments [119]. Konys et al. [120] reported that HDA could improve the corrosion resistance of steels. In their study, FeAl exhibited a better corrosion resistance than $FeAl_2$; hence, they concluded that the heat-treatment schedule should be optimized to transform Al-rich intermetallics into FeAl layers. In addition, Allély et al. [119] investigated anticorrosion mechanisms of aluminized steel. They found that improved corrosion resistance for Usibor® 1500 steel was obtained even though cracks were present in the coating. It was also possible that the coating layers in combination with the thin Al_2O_3 layer at the surface could act as barrier layers to separate the ADI substrate from the surrounding corrosive environment.

4.4 Conclusions

Successive HDA and austempering of SSF GJS-500-14 at different austempering temperatures was studied and the following results were obtained:

1. A surface treatment (HDA) and bulk heat treatment (austempering) were applied in combination to as-cast ductile iron.
2. After aluminizing, the as-cast sample consisted of a top layer of Al (with $FeAl_3$), middle layer of $FeAl_3$, and inner layer of Fe_2Al_5, as confirmed by the XRD and EDX analyses.
3. After austempering, the coatings were mainly composed of four layers: thin Al_2O_3, Fe_2Al_5 + $FeAl_2$, FeAl, and α-Fe.
4. The mean coating thickness of the aluminized samples increased by approximately three times due to austempering because of the diffusion of iron into the coating and aluminum into the substrate.
5. These two processes enhanced both corrosion resistance and mechanical properties of the as-cast ductile iron by forming intermetallic layers with a thin Al_2O_3 layer at the surface and ausferritic microstructure in the interior. However, no remarkable differences in terms of corrosion resistance of the austempered samples

were observed due to the similar coating morphology regardless of the austempering temperature.

6. The aluminized and austempered samples (ADI-270, ADI-330, and ADI-390) satisfied the mechanical property requirements of grades 1200-3, 900-8, and 800-10 according to the BS EN 1564 standard, respectively.

YK

5. EFFECT OF ALUMINIZING AND AUSTEMPERING PROCESSES ON STRUCTURAL, MECHANICAL AND WEAR PROPERTIES OF A SSF DUCTILE IRON [3]

5.1 Introduction

Ferritic ductile irons strengthened by high silicon (3.2-4.3 wt%) also known as solution strengthened ferritic ductile irons (SSFs) have a unique combination of properties, i.e. high yield strength, high tensile strength, high elongation, good castability, good machinability and low production cost [18]. SSFs have gained interest from foundries in recent years because they exhibit much better elongation and higher yield strength at the same tensile strength when comparing to conventional ferritic/pearlitic ductile iron grades [17]. However, poor strength/elongation ratio, insufficient toughness and wear resistance strictly limits the useful life of parts made of SSFs. Although austempering heat treatment improves the wear resistance of ductile irons due to the transformation of the as-cast structure into ausferritic structure, surface and subsurface graphite nodules have a negative effect on the wear resistance because severe plastic deformation and crack propagation are generated at local regions (graphite interfaces) during wear test [121]. Therefore, many surface treatment methods including laser surface melting, surface hardening, case hardening (boro-tempering) and surface alloying have been developed so far to improve the sliding wear resistance of austempered ductile iron (ADI) [122–125]. In addition to these methods, aluminide coatings, which were prepared by hot-dip aluminizing (HDA) and subsequent high-temperature diffusion, is considered a good solution to effectively improve sliding wear performance of steel [102,126].

Previously published investigations [62,63,109] mostly focused on structural and morphological properties of hot dip aluminized parts. Kobayashi and Yakou [63]investigated the evolution of Fe-Al intermetallic compound layers at different heat treatment conditions. They found that Fe_2Al_5 phase changed to FeAl and Fe_3Al phases at temperatures higher than 1000 °C. Cheng and Wang [62] studied microstructure and phase evolution of hot-dipped aluminide mild steel. They reported that $FeAl_2$ and FeAl phases formed at the interface between Fe_2Al_5 and the steel substrate after diffusion treatment, and Fe_2Al_5 layer was completely replaced by $FeAl_2$ with an increase in the diffusion time. On the other hand, there are few studies that have investigated wear characteristics of aluminide coatings generated by HDA and subsequent high-temperature diffusion [102,126]. Zhang et al. [126] studied dry sliding wear behavior of aluminide coated and uncoated AISI H13 steel and found that wear performance of the aluminized steel was improved as a result of the strong support from high-strength intermetallic compound. Although all these studies focused on the modification of HDA phase structure by high temperature diffusion but no attempt was made to modify the substrate microstructure simultaneously.

---

[3] This chapter is based on the paper "Y. Yürektürk, M. Baydoğan, Effect of aluminizing and austempering processes on structural, mechanical and wear properties of a SSF ductile iron, Mater. Res. Express 6 (2019), https://doi.org/10.1088/2053-1591/aae804."

Since temperature intervals of the diffusion process (700-1100 °C) and austenitizing step (850-975 °C) of austempering are in the same range, authors make an attempt to use the austenitizing step of austempering as the diffusion process applied after aluminizing. Once this was achieved, it would then be possible to obtain characteristic ADI microstructure (after subsequent austempering) while altering the coating phase simultaneously. Combining these two processes (aluminizing and austempering) in one is not only a cost effective way but also eliminates the need for protective atmosphere during austenitizing as well. Our previous work [127], which mainly deals with the corrosion behavior of a hot-dip aluminized and austempered ductile iron, clearly demonstrated that this technique can be appropriate for ADI without any deterioration in the mechanical properties. In the present study, it is therefore aimed to investigate the effect of the combined application of aluminizing and austempering processes on structural, mechanical and wear properties of a ferritic ductile iron, and the results were evaluated as compared to those obtained by the single application of aluminizing and austempering processes.

5.2 Experimental Details

5.2.1 Material and preparation

A commercial GJS 600-10 SSF ductile iron (C-3.1, Si-4.3, Mn-0.2, P-0.029, S-0.007, Mg-0.05 in wt%) was used as cylindrical substrates with dimension of Ø15×5 mm. Optical micrograph of a nital-etched (4 vol%) ductile iron in the as-cast state is shown in Figure 5.1. The as-cast ductile iron has a fully ferritic microstructure with nodular graphites distributed throughout the microstructure. Prior to the coating experiments, the samples were ground and polished in accordance with the standard procedures, and then ultrasonically cleaned in acetone and phosphorous acid for 15 min.

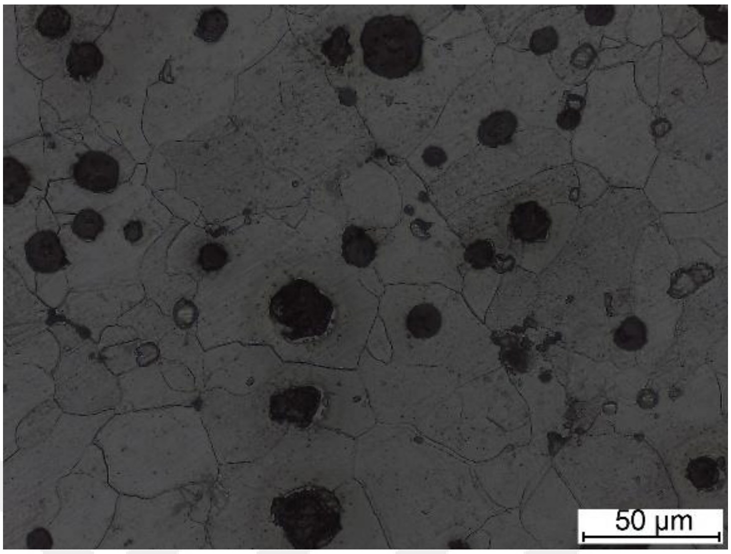

Figure 5.1 : Optical micrograph of GJS 600-10 ductile iron in as-cast state.

5.2.2 Coating procedure and heat treatment

Samples attached to a stainless-steel wire were aluminized at 750 °C for 5 min by immersing into high-purity (99.9 wt%) of molten aluminum bath in a graphite crucible in a resistance furnace. The samples were then removed from the bath and cooled down to room temperature. The molten Al bath was protected against oxidation by using a commercially available coverall flux. For austempering heat treatment, the as-cast and the aluminized samples were austenitized at 975 °C for 2 h and then austempered in a salt bath at 330 °C for 1 h followed by air cooling to room temperature. Schematic representations of the coating procedure and the heat treatment are shown in Figure 5.2.

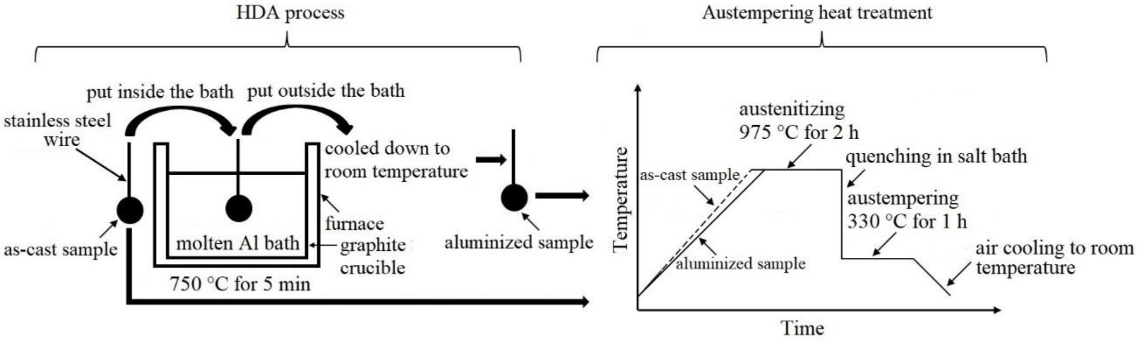
HDA process
Austempering heat treatment
put inside the bath
put outside the bath
stainless steel wire
cooled down to room temperature
furnace
as-cast sample
molten Al bath
graphite crucible
750 °C for 5 min
aluminized sample
Temperature
Time
austenitizing 975 °C for 2 h
quenching in salt bath
austempering 330 °C for 1 h
air cooling to room temperature
as-cast sample
aluminized sample

Figure 5.2 : Schematic representations of coating procedure and heat treatment.

As shown in Figure 5.2, heating rate of aluminized sample to the austenitizing temperature was lower than that of as-cast sample to facilitate the diffusion process in a controlled manner, while as-cast sample was heated to the austenitizing temperature in the conventional manner with a higher heating rate.

5.2.3 Structural characterizations

Phase analysis of the samples was characterized by using an X-ray diffractometer (XRD, GBC, MMA 027) with Cu-Kα radiation in the 2θ range from 20 to 90 degrees using goniometer step of 0.02 and scan speed of 1° per minute. The cross-sectional morphologies and the substrate microstructures of the nital-etched (4 vol%) samples were analyzed using a field emission scanning electron microscope (FE-SEM, Zeiss Ultra Plus) and an optical microscope (Leica DM 750M), respectively. An energy dispersive X-ray spectroscopy (EDX, Bruker XFlash 5010) system attached to SEM was also used to perform elemental analysis of the samples. The retained austenite volume fraction of the samples was estimated by X-ray diffraction analysis on the cross section of the polished surface by using the direct comparison method [75].

5.2.4 Mechanical properties

Hardness of samples was measured by using a universal hardness tester (Zwick, Roell ZHU 2.5) at an applied load of 100 g for a dwell time of 15 s. Tensile tests of samples were conducted at a cross-head speed of 2 mm.min^{-1} on a servo-hydraulic controlled universal test system (Instron 8801) at room temperature by using cylindrical samples with a gage length of 25 mm per ASTM E8/E8M standard.

5.2.5 Tribological properties

Wear performance of the samples was examined at room temperature by a ball-on-disc type wear tester (CSM High Temperature Tribotester) under dry sliding conditions. Samples were worn against a 6-mm diameter Si3N4 ball along a circular path of 2.5 mm in radius with a sliding speed of 2 cm/s. The applied load and total length of the sliding path were chosen 3 N and 200 m, respectively. After the wear tests, the worn volume of the samples was calculated from the width and depth of the wear-tracks obtained by using a 2-D contact surface profilometer (Dektak-6M, Veeco). Wear rate of the samples was expressed in terms of mm3/Nm by dividing the worn volume by the applied load and the total length of the sliding path. The wear tracks of the samples were examined by EDX equipped FE-SEM and Raman spectroscopy (Renishaw, inVia Reflex spectrometer) using an excitation wavelength of 632.8 nm.

5.3 Results and Discussion

5.3.1 Coating characterization after hot-dip aluminizing

Figure 5.3 shows (a, b) cross-sectional SEM micrographs and (c) surface XRD pattern of HDA sample. Point EDX results, which are gathered from these SEM micrographs, were given in Table 5.1. According to Figure 5.3, three distinct regions are observed in the coating, outer Al topcoat with $FeAl_3$ as the discrete phase in it, middle $FeAl_3$ separated from Fe_2Al_5, and inner phase of Fe_2Al_5 at the interface. The obtained results from the EDX analysis were further confirmed by XRD pattern given in Figure 5.3. The cross-sectional SEM micrographs proved that the main intermetallic phase is Fe_2Al_5 with a thickness of about 40 μm after HDA due to the high growth rate of Fe_2Al_5 with an orthorhombic structure [61]. Thanks to orthorhombic structure of Fe_2Al_5, the crystalline defects, 30% vacancy in the c-axis direction, offered a rapid diffusion path to increase the growth rate of Fe_2Al_5 [61,105], resulting in tongue-like Fe_2Al_5.

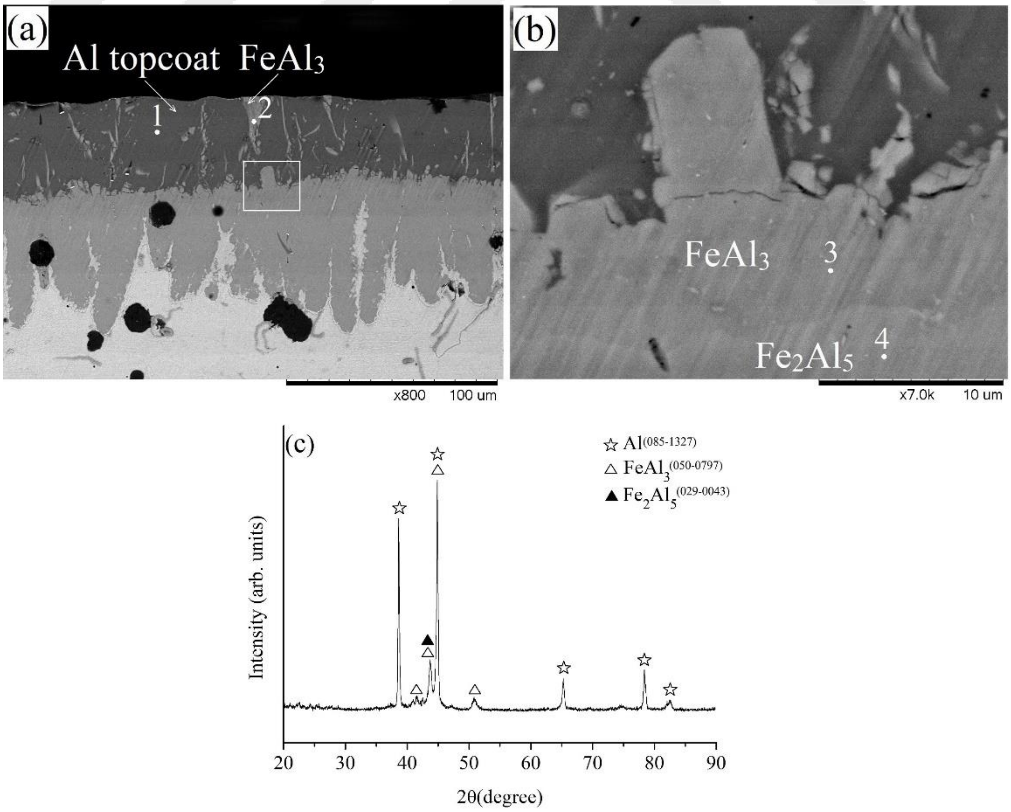

Figure 5.3 : (a) Cross-sectional SEM micrograph, (b) magnified micrograph of framed rectangular region in (a), and (c) surface XRD pattern of HDA sample.

Table 5.1 : Point EDX analysis results of HDA sample.

Point	Element (at%)				
	Al	Fe	Si	O	Phase
1	100	-	-	-	Al
2	76.73	22.58	0.69	-	$FeAl_3$
3	78.45	19.39	2.16	-	$FeAl_3$
4	72.88	25.83	1.29	-	Fe_2Al_5

The EDX mapping of HDA sample is presented in Figure 5.4. It is quite clear that the Al content decreases on moving towards the substrate, while the Fe content is increasing towards the top surface of the coating. Also, some Si signals are appeared in the coating, coming from the underlying substrate containing a high amount of silicon. These findings showed that EDX mapping results were consistent with previously obtained SEM-EDX results.

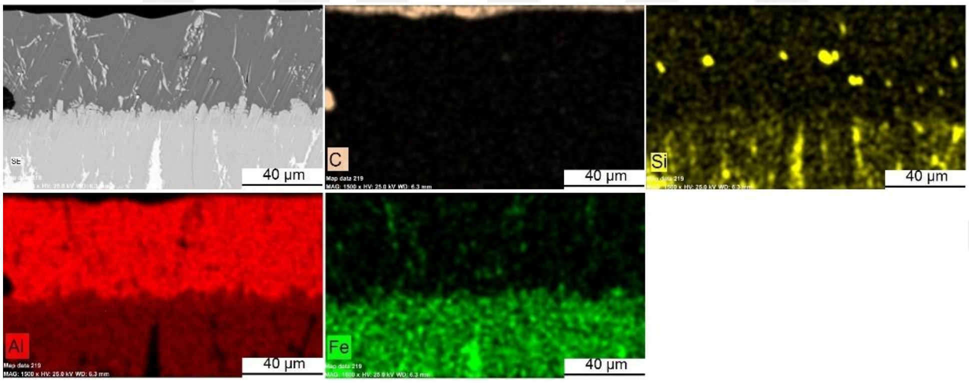

Figure 5.4 : Cross-sectional elemental mapping of HDA sample.

5.3.2 Coating characterization after austempering on hot-dip aluminized ductile iron

The cross-sectional SEM micrographs of HDA+ADI sample are presented in Figure 5.5. Application of austempering on HDA sample, coating structure was modified into Al_2O_3 scale, Fe_2Al_5 + $FeAl_2$, FeAl and α-Fe layers, as detected by point EDX analysis (see Table 5.2). During diffusion annealing (austenitizing), outward or inward diffusion of the elements take place. In this respect, the formation of Al_2O_3 scale is attributed to outward diffusion of Al from topcoat [106] during austenitizing. FeAl and $FeAl_2$ phases were produced from the initial tongue-like morphology of Fe_2Al_5 phase through high temperature austenitizing [96]. Moreover, formation of α-Fe layer is a result of aluminum diffusion into the substrate. According to magnified portion of α-Fe layer, it is clearly seen that it does not evolve into ausferrite during austempering because it contains about 7.5 at% aluminum, which promotes α-Fe stabilization during austenitizing [109]. On the other hand, high-magnification FE-SEM micrograph of the substrate shown in Figure 5.5 exhibited a typical ausferritic microstructure consisting of ferrite laths in acicular morphology (α–bcc) and retained austenite (γ–fcc) between the ferrite laths. The thickness of the ferrite laths, which are obstacles to dislocation motion [128], is in the range of 50-80 nm measured from FE-SEM micrograph.

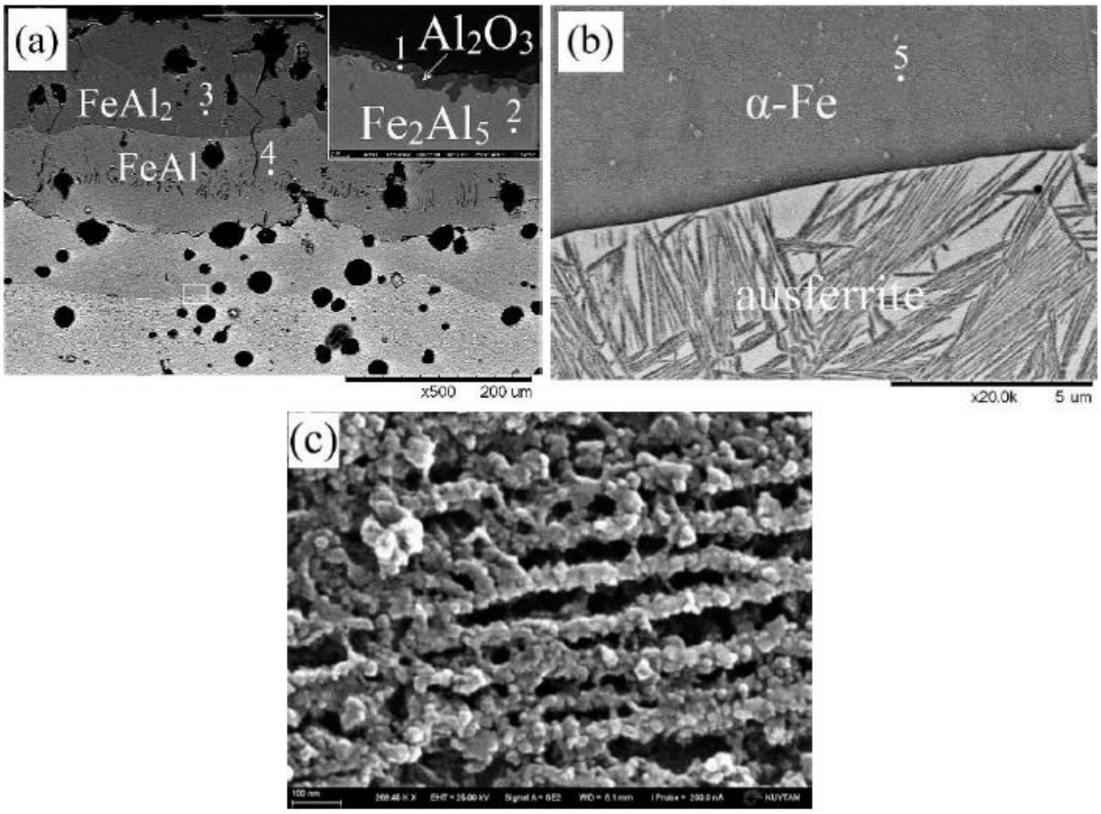

Figure 5.5 : (a) Cross-sectional SEM micrograph of HDA + ADI sample, (b) magnified micrograph of framed rectangular region in (a), and (c) magnified micrograph of substrate.

Table 5.2 : Point EDX analysis results of HDA + ADI sample.

Point	Element (at%)				
	Al	Fe	Si	O	Phase
1	41.39	-	-	58.61	Al_2O_3
2	72.30	26.68	1.02	-	Fe_2Al_5
3	64.01	34.74	1.24	-	$FeAl_2$
4	45.06	52.43	2.51	-	FeAl
5	7.52	84.85	7.63	-	α-Fe

The corresponding phase map of HDA + ADI sample is shown in Figure 5.6. It was clearly seen that the distribution of all the elements were highly varied by austempering. Silicon coming from the underlying substrate is distributed more homogeneously in the coating structure after austempering. It should be also mentioned that some black areas of spherical morphology do not belong to graphite phase as evidenced in EDX mapping of carbon, therefore, the existence of these areas show that there are nodular-like pores in the structure. These pores were especially visible within the Fe_2Al_5 + $FeAl_2$ layer and attributed to well-known Kirkendall effect origination from the different diffusion rates of Al and Fe atoms. By the application of austempering, Al content decreased from the surface toward the substrate due to the inward diffusion of aluminum atoms, while the Fe content increased due to the outward diffusion of iron atoms [106]. In addition, O and Al close to the surface reveal the presence of an oxide layer at the surface, which was already confirmed by the point EDX analysis as seen in Table 5.2. On the other hand, there are some cracks within the coating and they have been nucleated and grown from brittle Al-rich phases (Fe_2Al_5, $FeAl_2$). These cracks can be the result of high temperature difference between austenitizing (975 °C) and austempering (330 °C) temperatures, but, these cracks did not reach the tougher α-Fe layer. It can be finally deduced that the each layer within the coating was well adhered to each other and there was no discontinuity between them even though outer layers (Fe_2Al_5, $FeAl_2$) have some pores and cracks in a limited extent.

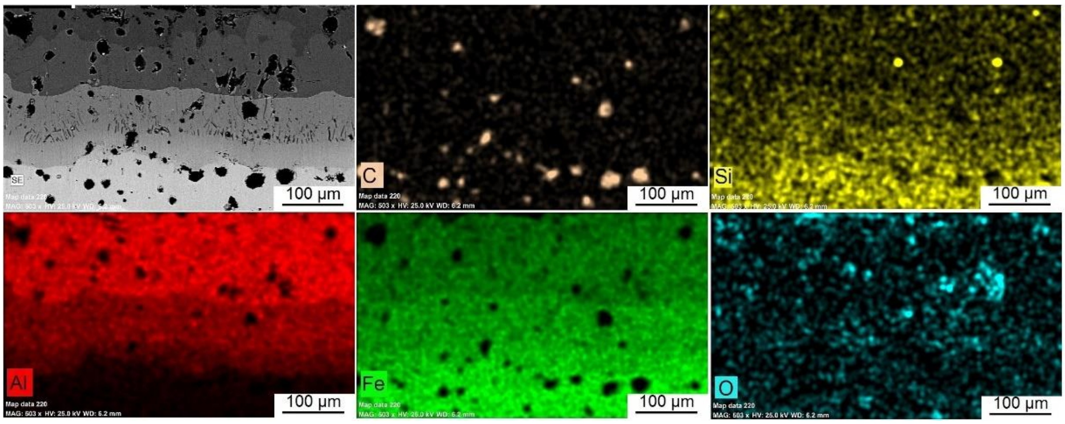

Figure 5.6 : Cross-sectional elemental mapping of HDA + ADI sample.

Surface SEM micrograph (a), EDX analysis result of marked points (b) and surface XRD pattern (c) of HDA+ADI sample are displayed in Figure 5.7. From the SEM micrograph, the surface exhibits porous and rough appearance with some flat regions. EDX analysis reveals strong Al and O peaks, suggesting the presence of Al_2O_3 as the surface oxide. However, Al_2O_3 does not seem to be a continuous layer, and hence

Fe_2Al_5 was also detected on the surface. In addition, XRD pattern from the surface (Figure 5.7) demonstrated that coating layer composed of Al_2O_3 Fe_2Al_5, $FeAl_2$, FeAl and Fe phases, which were compatible with the point EDX results taken from the cross-section of the coating (Figure 5.5, Table 5.2).

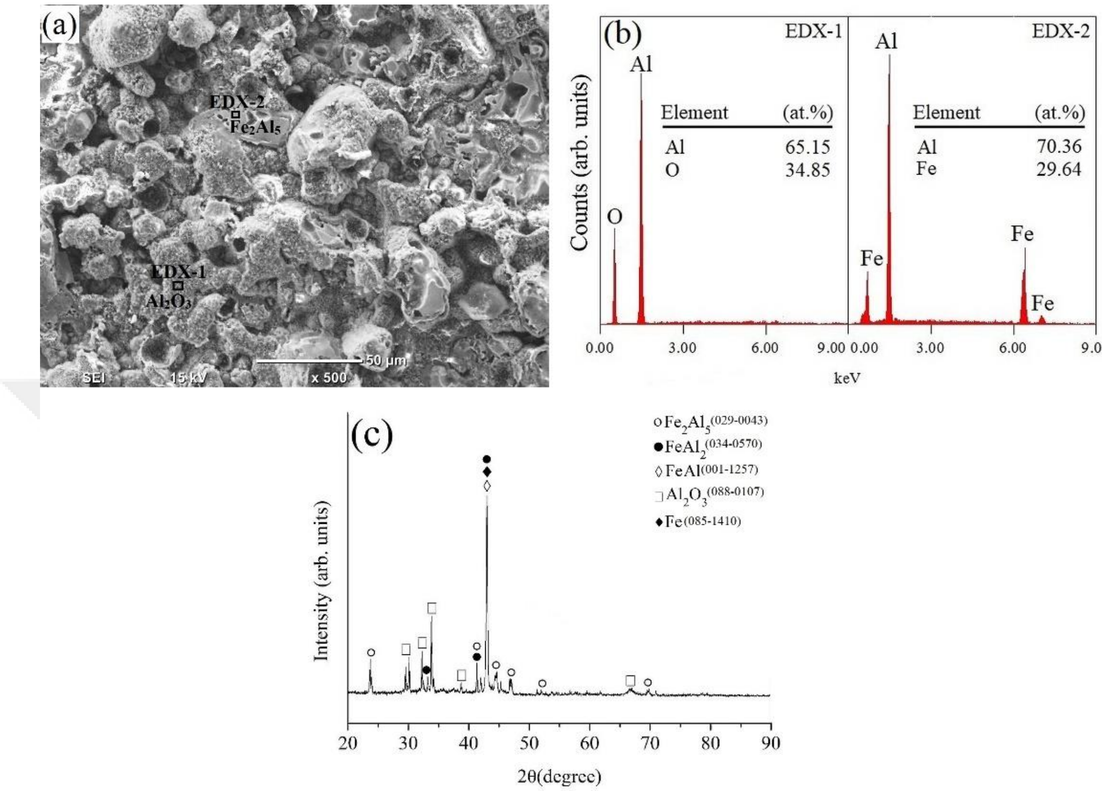

Figure 5.7 : Surface SEM micrograph (a), EDX analysis result of marked points (b), and surface XRD pattern (c) of HDA + ADI sample.

Figure 5.8 shows the hardness of the phases after successive application of HDA and austempering (HDA + ADI sample). It can be clearly seen that Al-rich phases ($FeAl_3$, Fe_2Al_5, $FeAl_2$) have higher hardness compared to that of Fe-rich phases, and the hardness results are compatible with the literature [111,112]. It was previously reported that the presence of Al-rich phases having high hardness was a problem due to their brittle nature with low fracture toughness as it promotes formation and propagation of cracks in the coating [63,110]. However, more ductile FeAl intermetallic enhanced the interface strength and fracture toughness of the coating [110]. It is therefore finally concluded that the transformation of initial Al-rich intermetallic of Fe_2Al_5 to Fe-rich phases (FeAl, α-Fe) after austempering is beneficial in terms of improved interface strength and high fracture toughness.

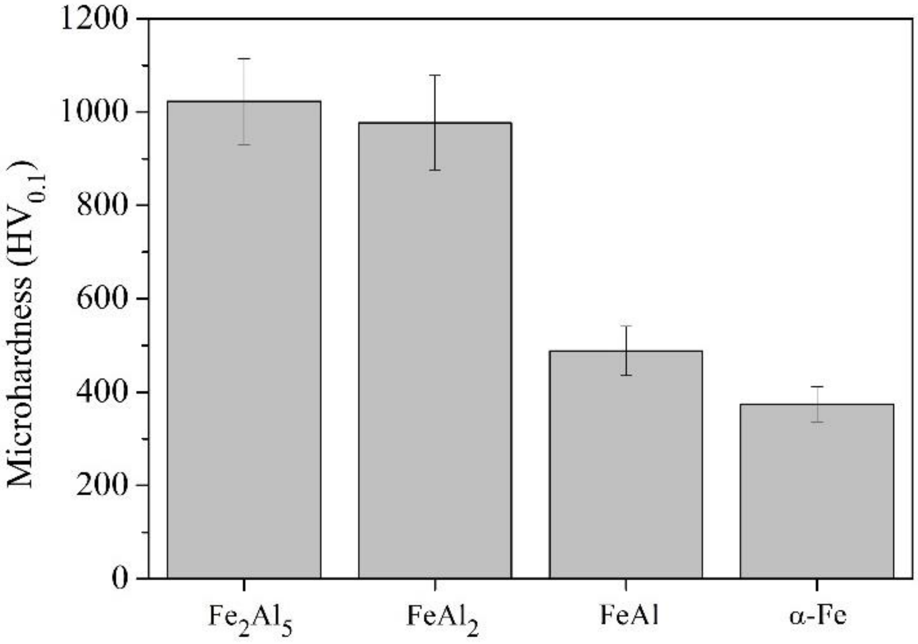

Figure 5.8 : Hardness of phases on HDA + ADI sample.

5.3.3 Mechanical and microstructural properties

Figure 5.9 shows stress-strain curves of the investigated samples. Yield strength, ultimate tensile strength, elongation at fracture, substrate hardness and retained austenite content values of samples are listed in Table 5.3. Results clearly revealed that there was no significant change between the mechanical properties of the as-cast and HDA samples. It was previously reported that the thickness of intermetallic layer is the main factor affecting the mechanical properties of aluminized parts, and it is desired to keep the thickness of intermetallic layer to a minimum value due to brittle nature of this layer [57]. In the current study, the thickness of intermetallic layer on HDA sample was about 60 μm (Figure 5.3), and it is revealed by the results that this value is not high enough to significantly affect the mechanical properties. Similarly, an experimental work performed on mechanical properties of aluminized steel plate by Kim and Choi [129] found that the ultimate tensile strength and elongation of aluminized steel exhibited a nearly constant value over all thickness below about 150 μm. As shown in Table 5.3, HDA + ADI sample has higher hardness and lower retained austenite content than ADI sample. Substrate hardness of ADI material decreases with increasing volume fraction of retained austenite in the microstructure, as expected. On the other hand, it is known that higher heating rates lead to higher volume fraction of retained austenite [130]. In the present study, HDA + ADI sample was subjected to a lower cooling rate to facilitate diffusion in a controlled manner during austenitizing, while ADI sample was austenitized in the conventional manner with a higher heating rate. It is therefore reasonable to attribute the difference in substrate hardness and retained austenite content to different heating rates of the samples during heating to the austenitizing temperature. On the other hand, even though substrate hardness of HDA + ADI sample is higher than that of ADI sample, it exhibited 5% and 24% lower yield and tensile strength values, respectively with 41% higher ductility compared to ADI sample. It can be attributed to high thickness of the brittle intermetallic layer (Fe_2Al_5 + $FeAl_2$, ~150 µm) accompanied by pores and cracks in the coating (Figure 5.5), having potentiality to decrease strength values. It should also be mentioned that yield strength decrement was less as compared to that of ultimate tensile strength, implying the more pronounced effect of the surface irregularities on ultimate tensile strength. Badaruddin et al. [131] similarly reported that some pores and cracks were generated on aluminized steel after diffusion treatment, and this led to a decrement on mechanical properties of aluminized steel as a result of stress concentration in the coating layer. The increment in ductility in HDA + ADI samples can also be ascribed through ductile phases of FeAl and α-Fe with a thickness of ~105 µm and ~70 µm, respectively, in the coating structure. The presence of crack-free and pore-free ductile phase (α-Fe) with the high total thickness of the ductile phases in the coating positively affected the ductility [129,131].

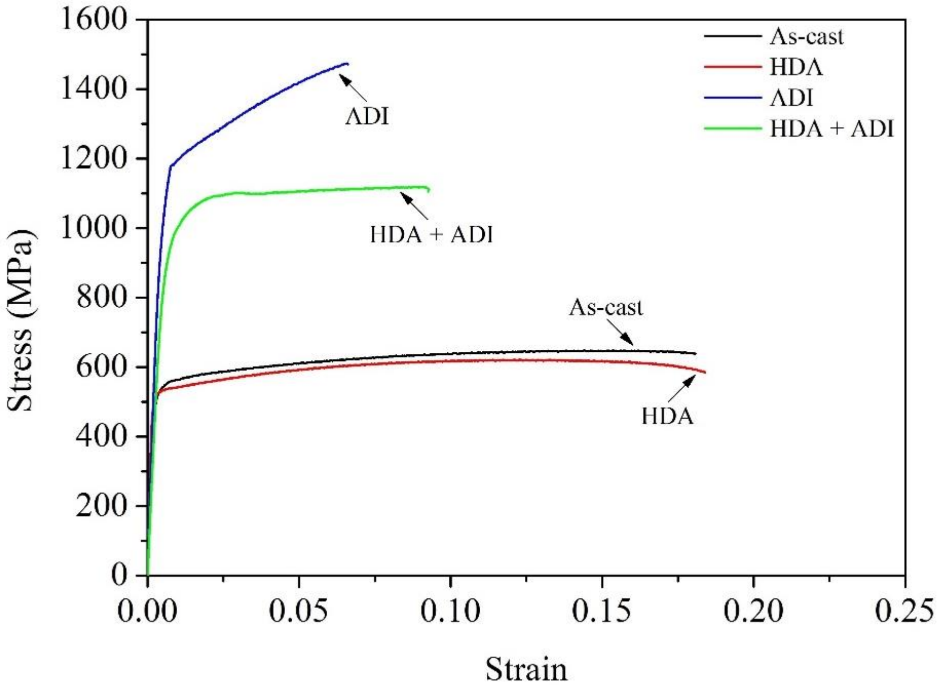

Figure 5.9 : Stress-strain curves of investigated samples.

Table 5.3 : Mechanical and microstructural properties of investigated samples.

Sample	0.2 % Proof strength (MPa)	Ultimate tensile strength (MPa)	Elongation at fracture (%)	Substrate hardness ($HV_{0.1}$)	Retained austenite content (vol%)
As-cast	518 ± 17	641 ± 19	18.1 ± 1.5	251 ± 19	–
HDA	507 ± 22	619 ± 16	18.4 ± 2.1	234 ± 12	–
ADI	1012 ± 21	1465 ± 44	6.6 ± 0.8	465 ± 16	23.1
HDA + ADI	966 ± 13	1112 ± 31	9.3 ± 1.1	547 ± 22	18.4

5.3.4 Tribological characteristics

Wear track profiles of the investigated samples are shown in Figure 5.10.

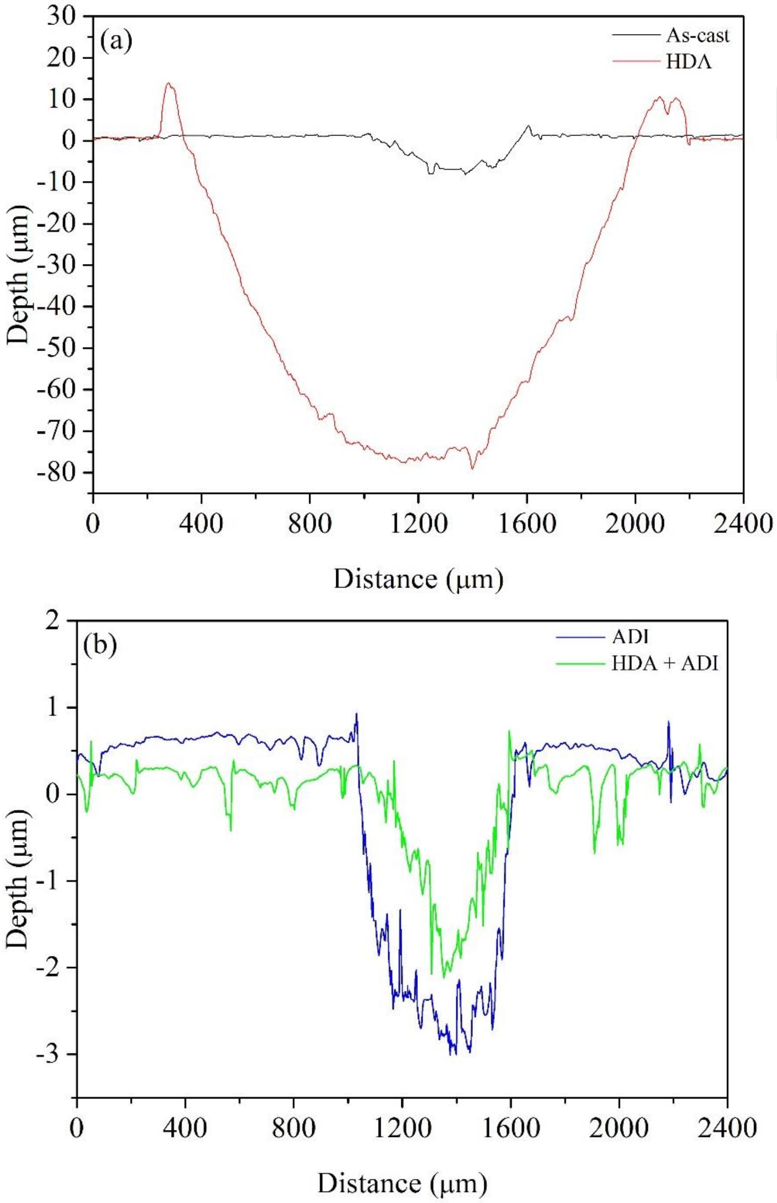

Figure 5.10 : Wear track profiles of investigated samples: (a) As-cast and HDA samples, and (b) ADI and HDA + ADI samples.

The as-cast sample showed smaller wear track as compared to that of HDA sample, and calculated wear rates of the as-cast and HDA samples are 9.74 and 36.29 (x10^{-5} mm^3/Nm), respectively. This shows that the wear resistance of the as-cast sample is better than that of HDA sample. It is a result of Al topcoat on the surface of HDA sample having a lower hardness than that of the as-cast sample, and clearly suggests that the surface hardness is a significant factor determining the wear rate of HDA sample.On the other hand, wear rate (x10^{-5} mm^3/Nm) of ADI and HDA + ADI samples are 4.53 and 3.45, respectively (Figure 5.10). This shows that a 30% increment in the wear resistance was achieved when the sample is austempered after HDA, and could be attributed to higher substrate hardness of HDA + ADI sample. In the view point of the effect of the subsurface on the wear resistance, it was previously reported [102,126] that, subsurface intermetallic compounds of aluminide coatings (prepared by HDA and subsequent diffusion treatment) provide a strong support during sliding wear even though the wear cracks slightly reduce the surface integrity. Moreover, it is also likely that the Al$_2$O$_3$ scale on the surface could provide an additional protection against wear during sliding.

The worn surface SEM micrographs of the as-cast and HDA samples are presented in Figure 5.11.

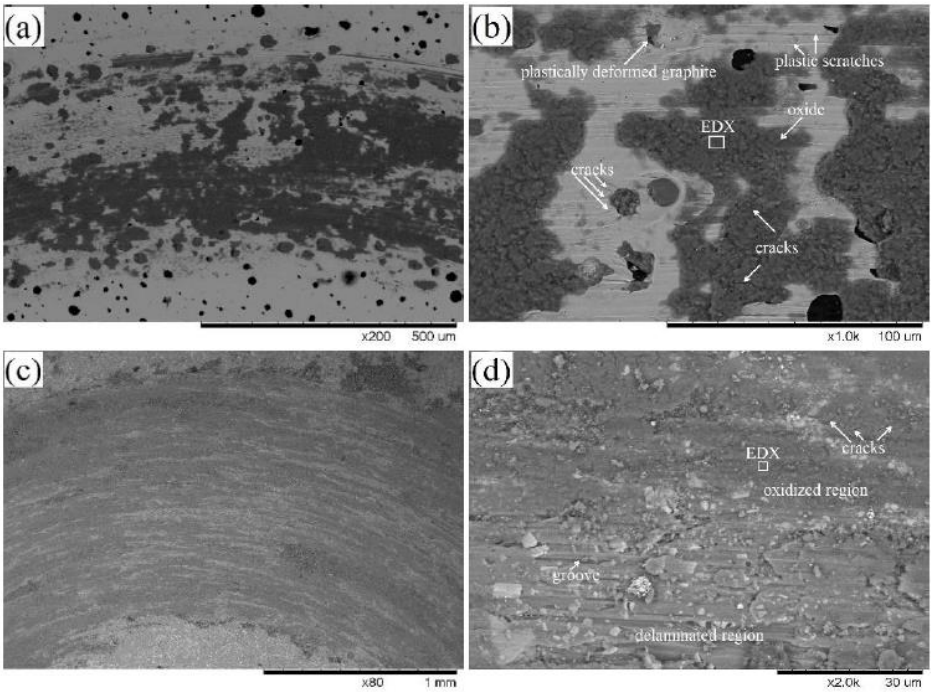
(a)
x200 500 um
(b)
plastically deformed graphite
plastic scratches
oxide
EDX
cracks
cracks
x1.0k 100 um
(c)
x80 1 mm
(d)
EDX
cracks
oxidized region
groove
delaminated region
x2.0k 30 um

Figure 5.11 : Worn surface SEM micrographs of as-cast and HDA samples: (a) as-cast sample, (b) magnified micrograph of worn surface region in (a), (c) HDA sample, (d) magnified micrograph of worn surface region in (c).

The worn surface of the as-cast sample contains plastic flow and scratches along the sliding direction. Moreover, some graphite spheres were ruined and flowed depending on the deformation due to the abrading action of the ball. It was explained by Prado et al. [132] that severe plastic deformation and crack propagation are generated at the graphite nodule during wear test and the growth of these cracks on the plastically deformed graphite nodules controls the wear mechanism. As shown in Figure 5.11, dark, cracked and discontinuous oxide areas were also formed in the wear debris of the as-cast sample. The presence of high amount of oxide on the worn surface indicated that the wear mechanism is mainly controlled by oxidation under the present experimental condition, which led to the loss of material during the wear test. Raman spectroscopy and EDX analysis of the oxides formed on the as-cast sample are given in Figure 5.12., which is a typical Raman spectrum of the amorphous Al_2O_3 structure [135,136].

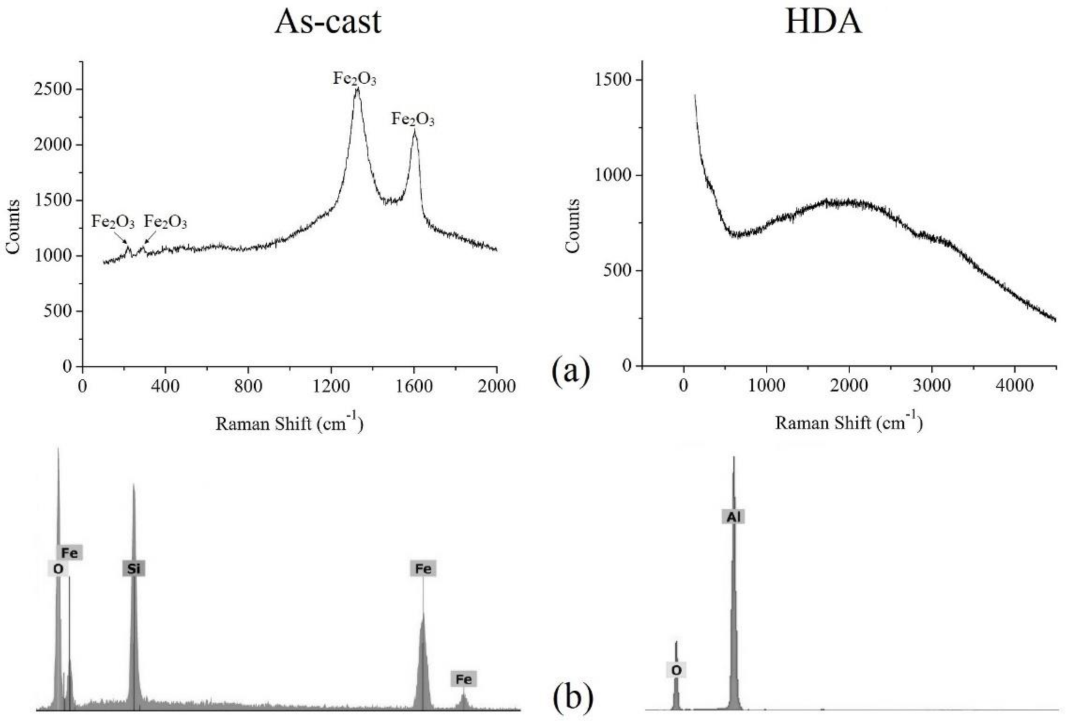

Figure 5.12 : Worn surface of as-cast and HDA samples: (a) Raman and (b) EDX patterns.

It was found that the Raman spectra of the oxide on the worn surface corresponded to hematite (Fe_2O_3) [133,134] as supported by the EDX analysis. It should be also noted that very strong peak of Si has appeared on the EDX pattern of the as-cast sample, which was attributed to its transfer from Si_3Ni_4 counterface material, and no SiO_2 was found on the worn surface as verified by Raman spectroscopy. For HDA sample (Figure 5.11), fragmented particles, grooves, abrasion scratches and plastic deformation traces were seen on the worn surface SEM micrograph. The present results of these wear characteristic are strongly related to the low surface hardness of HDA sample, and the delamination is the main wear mechanism. When compared to the as-cast sample, the worn area of HDA sample becomes wider along with a decrement in the surface hardness, which induced delamination on HDA coating layer. On the other hand, the worn surface of HDA sample contains both O and Al, which were identified by EDX analysis as shown in Figure 5.12. Raman spectra of the oxidized region (Figure 5.12) shows that no characteristic Raman peak of crystalline alumina was found but there is only a broad luminescence line centered at 2000 cm^{-1}. Morphologies of worn surfaces for ADI and HDA + ADI samples are shown in Figure 5.13.

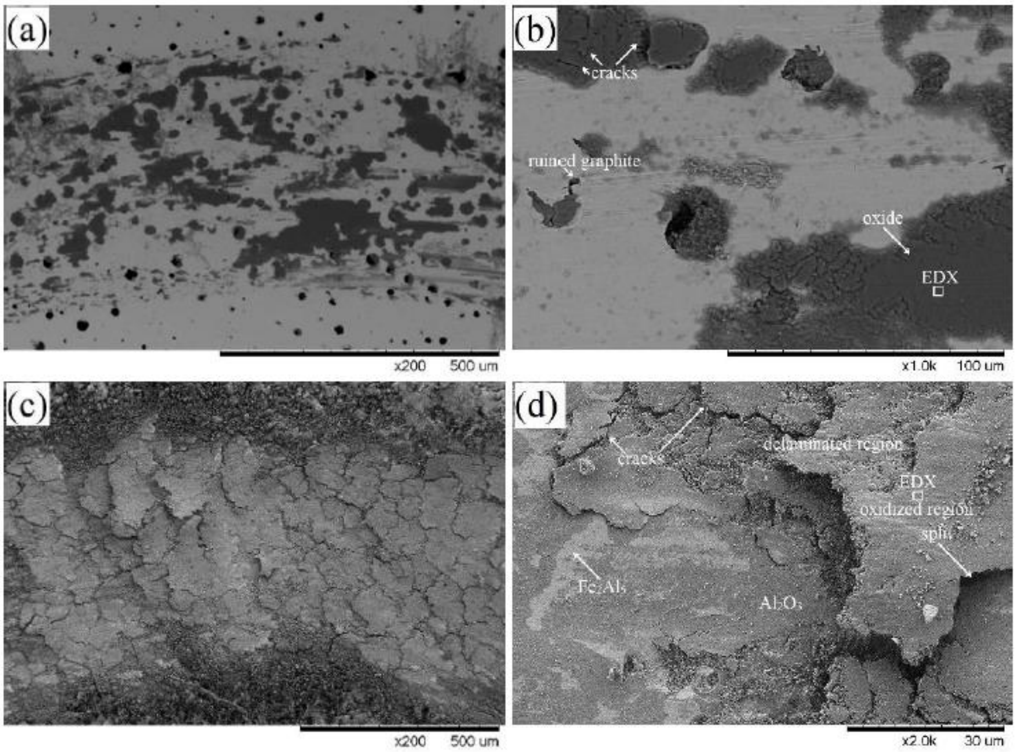

Figure 5.13 : Worn surface SEM micrographs of ADI and HDA + ADI samples: (a) ADI sample, (b) magnified micrograph of worn surface region in (a), (c) HDA + ADI sample, (d) magnified micrograph of worn surface region in (c).

In the worn surface of ADI sample, dark and smooth oxide areas are observed but the oxide does not cover the surface. On the other hand, no trace of plastic deformation or cracks are present in the metallic zone. Therefore, it is understood that the main mechanism of wear is the oxidation of ADI sample. Raman and EDX patterns taken from the oxide region of the worn surface of ADI sample are given in Figure 5.14.

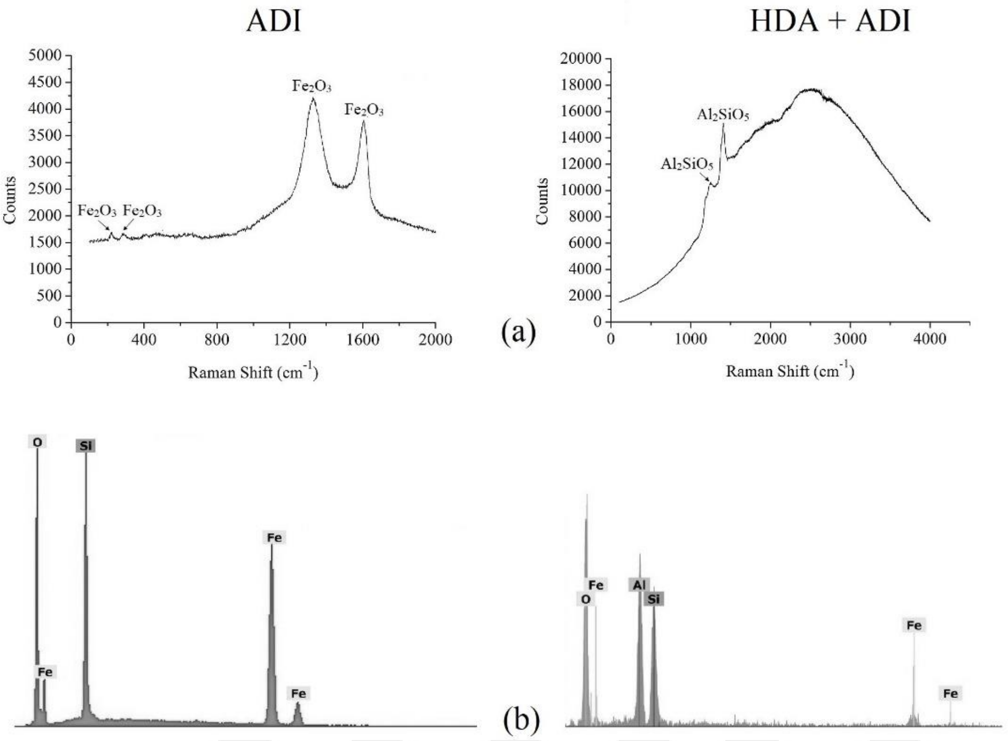

Figure 5.14 : Worn surface of ADI and HDA + ADI samples: (a) Raman and (b) EDX patterns.

The Raman shifts in the pattern of ADI sample are corresponding to oxides of Fe (Fe_2O_3) [133,134], and EDX pattern confirms the formation of oxide regions on the worn surface owing to the presence of strong oxygen peak. Here, strong EDX peak of Si is could be derived from transfer of the Si_3N_4 counterface material during wear. Additionally, no evidence of SiO_2 peak was identified by Raman analysis. For the worn SEM micrographs of HDA + ADI sample (Figure 5.13), it exhibited light and dark gray areas, which correspond to Al_2O_3 (in at%; 65.96 O, 29.70 Al, 4.34 Si) and Fe_2Al_5 (in at%; 69.55 Al, 28.78 Fe, 1.67 Si), respectively, as determined by EDX analysis taken from these areas. The existence of Al_2O_3 and Fe_2Al_5 on the worn surface, which is compatible to the previous EDX analysis showing surface elemental composition (Figure 5.7), indicates that the wear takes place in a very small depth of penetration within Fe_2Al_5 layer, which is in agreement to the wear track depth in Figure 5.10. The Raman and EDX patterns taken from the oxidized region of the worn surface of HDA + ADI sample are also presented in Figure 5.14. According to Raman analysis, the observed peaks belong to complex oxide of Al_2SiO_5 [137,138], and the EDX result seems to support it owing to existence of strong oxygen peak along with very strong silicone peak coming from the Si_3N_4 counterface ball. The worn surface has a characteristic appearance of wear track of brittle materials [139,140]. These cracks were formed during sliding action and can be attributed to brittle fracture form of wear mechanism, which occurs in such materials having a tensile strength less than one-third of their compressive strength [139]. Therefore, in brittle materials, cracking may be seen during sliding.

Variations of the friction coefficient with respect to the sliding distance for the investigated samples are shown in Figure 5.15.

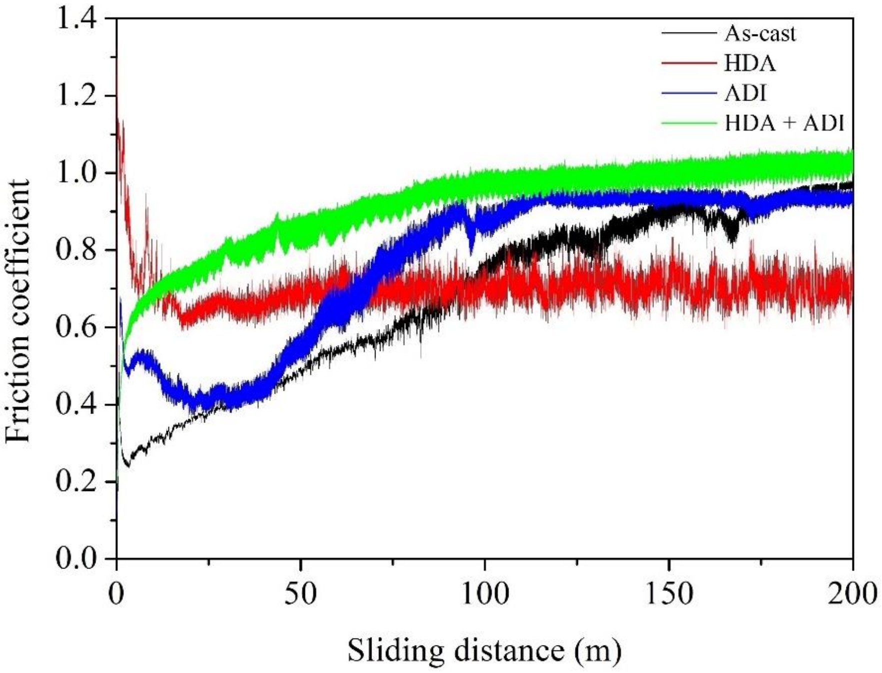

Figure 5.15 : Variations of friction coefficient as a function of sliding distance for investigated samples.

Friction coefficients of the as-cast and HDA samples started off from a very low value and continued with sharp fluctuations. In contrast to the as-cast sample, HDA sample reached a steady state friction coefficient and showed a stable friction behavior. Mean friction coefficients of the as-cast and HDA samples were found as 0.68 and 0.70, respectively. Although the mean friction coefficients of the samples are very close to each other, they exhibited different variations as a function of the sliding distance, and the as-cast sample shows slightly higher mean friction coefficient as compared to HDA sample. This can be explained by the lubrication effect arising from the incorporating graphites in the as-cast matrix [141]. On the other hand, comparison of friction coefficient variations of ADI and HDA + ADI samples show that mean friction coefficients were 0.77, and 0.92, respectively. Friction coefficient of HDA + ADI sample increases continuously from the beginning in contrast to that of ADI sample. After a while, friction coefficients of both samples achieve a steady state regime. HDA + ADI sample shows higher steady state friction coefficient as compared to ADI sample which may be attribute to higher surface roughness of the coating structure.

5.4 Conclusions

Main conclusions of the present study highlight the effect of combined application of hot-dip aluminizing (HDA) and austempering treatments on the properties of the as-cast ductile iron. When it is applied as a single HDA process to the ductile iron, it does not strongly affect the tensile properties due to the limited thickness of the coating layer, while it results in a significant decrement in the wear resistance of the as-cast ductile iron due to the high amount of aluminum on the surface. On the other hand, ADI sample has the highest strength with limited amount of ductility amongst the all samples and it has significantly higher wear resistance than the as-cast and HDA samples. When aluminizing is applied before austempering (HDA + ADI sample), strength values are reduced in favor of the improved ductility as compared to single austempering (ADI). It is worth noting that yield strength is less affected from the combined application of these two processes as compared to ultimate tensile strength. In the view point of wear resistance, additional austempering after HDA improves the wear resistance by about 30%, which is attributed to the support of newly formed Fe-Al intermetallics in the subsurface during austenitizing.

6. CONCLUSIONS AND RECOMMENDATIONS

The aim of this thesis was to find out how the properties of solution strengthened ferritic ductile irons (GJS-500-14, GJS-600-10) change with the application of single austempering, single aluminizing or both of them. These SSF ductile irons subjected to single austempering are comparable to standardized ADI grades with respect to mechanical properties. The magnetic properties of as-cast and austempered ductile irons were discussed in terms of silicon content and austempering conditions, and it was found that saturation magnetization decreased with increasing silicon content and its value also increased as the ferromagnetic ferrite volume fraction increases depending on lower austempering temperature. After single austempering, retained austenite content calculation by magnetic method can be an alternative to XRD method. The mid-austempering temperature (330 °C) is the most suitable for obtaining optimum mechanical properties, and the wear resistance increased by about 50% as compared to as-cast ductile iron at this austempering condition. The mechanical properties were almost unchanged with the application of single aluminizing on as-cast ductile irons, whereas the wear resistance worsened about 4 times. The brittle phases ($FeAl_3$, Fe_2Al_5) were formed in the coating after single aluminizing, and additional austempering on this aluminized ductile iron contributed to the formation of ductile phases (FeAl, α-Fe) with a thin Al_2O_3 layer at the surface, which enhanced both corrosion and wear resistance. With the application of combined processes (aluminizing followed by austempering), an ausferritic microstructure was also formed in the interior as in single austempering. When compared to interior microstructure hardness values, the combined application of two processes provides higher microstructure hardness as compared to single austempering process as a result of lower retained austenite content depending on lower heating to the austenitizing temperature. The yield strength was also less affected with additional aluminizing before austempering, which reduced the tensile strength but incresed ductility as compared to single austempered ductile irons.

Almost every component produced for use in the automotive industry is exposed to vibrations along with dynamic loading under service conditions. Vibrations cause cyclic loads on that material and fatigue is an effective mechanism of failure, even if the maximum stress acting is below the yield strength of material. Due to the increased interest on SSF ductile irons and the limited number of studies on fatigue behaviour of this materials, especially on heavy section components, makes the fatigue behaviour of SSF ductile irons significant. It is known that fatigue limit of ductile cast irons is mainly controlled by the presence of casting defects such as microshrinkages or dross defects, and high silicon in SSF ductile irons decreases total shrinkage during solidification and this ductile irons show low risk of increased dross formation. Therefore, fatigue behaviour of SSF ductile irons, which are strengthened and toughened by austempering, can be studied as a possible future work. In addition, HDA coating and austempering conditions can be optimized to achieve more crack-free and pore-free coatings, and then, fatigue properties of this HDA coated and austempered SSF ductile irons can be studied. On the other hand, considering current and potential application areas of ADIs, the knowledge of ductile-to-brittle transition temperatures and consequently the impact behavior of ADI at subzero temperatures is very useful, and therefore, it can be studied the impact properties of austempered SSF ductile irons with or without aluminizing as a possible future work.

REFERENCES

[1] **Jha, N.K.** (2015) *Green design and manufacturing for sustainability*. Crc Press, .

[2] **Šamec, B., Potrč, I., and Šraml, M.** (2011) Low cycle fatigue of nodular cast iron used for railway brake discs. *Engineering Failure Analysis*. *18* (6), 1424–1434.

[3] **Double, D.D. and Hellawell, A.** (1995) The nucleation and growth of graphite—The modification of cast iron. *Acta Metallurgica et Materialia*. *43* (6), 2435–2442.

[4] **Okunnu, R.** (2015) *High strength solution-strengthened ferritic ductile cast iron.* (Master thesis) Aalto University, ESPOO.

[5] **Backerud, S.L.** (1996) Determination of the carbon equivalent in structure-modified cast iron. *U.S. Patent No. 5,577,545*. Washington, DC: U.S. Patent and Trademark Office.

[6] **Aggen, G. and Allen, M.** (2018) *ASM Handbook Volume I Properties and Selection: Irons, Steels, and High-Performance Alloys*. ASM International: The Materials Information Company, .

[7] **Goodrich, G.M.** (2004) *Iron castings engineering handbook.* American Foundry Soc., .

[8] **Metals Handbook** (2008) *Volume 15 Casting*. Materials Park: ASM International. 416–522.

[9] **Lampman, J.R. and Peters, A.T.** (1981) *Ferroalloys and Other Additives to Liquid Iron and Steel: A Symposium*. ASTM International, .

[10] **Oluwole, O.O., Olorunniwo, O.E., Ogundare, O.O., Atanda, P.O., and Oridota, O.O.** (2007) Effect of Magnesium and Calcium as Spheroidizers on the Graphite Morphology in Ductile Cast Iron. *Journal of Minerals and Materials Characterization and Engineering*. *6* (01), 25.

[11] **Brown, J.** (1999) *Foseco non-ferrous foundryman's handbook*. Butterworth-Heinemann, .

[12] **Skaland, T.** (2001) A New Approach to Ductile Iron Inoculation. in: Trans. Am. Foundry Soc. One Hundred Fifth Annu. Cast. Congr., pp. 1–12.

[13] **Elkem, A.S.** (2009) Cast Iron Inoculation—The Technology of Graphite Shape Control. *Foundry Products Division, Oslo*.

[14] **Olsson, A.** (2011) Fatigue strength of truck components in cast iron–Fatigue rig design, test results and analysis.

[15] **Callister, W.D. and Rethwisch, D.G.** (2000) *Fundamentals of materials science and engineering*. Wiley London, UK:, .

[16] **Rundman, K.B.** (2001) *Cast irons, in Encyclopedia of materials: science and technology (Second Edition)*, K.H.J.B. Editors-in-Chief: et al., Editors. 2001, Elsevier: Oxford. p. 1003–1010.

[17] **Stets, W., Löblich, H., Gießereitechnik, I., Gassner, G., and Schumacher, P.** (2014) Solution strengthened ferritic ductile cast iron properties, production and applicatıon. *International Journal of Metalcasting. 8* (2), 35–40.

[18] **Torre, U. De, Loizaga, A., Lacaze, J., and Sertucha, J.** (2014) As cast high silicon ductile irons with optimised mechanical properties and remarkable fatigue properties. *Materials Science and Technology. 30* (12), 1425–1431.

[19] **Larker, R., Ab, I., and Vindeln, S.** (2009) Solution strengthened ferritic ductile iron ISO 1083 / JS / 500-10 provides superior consistent properties in hydraulic rotators. *China Foundry*. *6* (4), 343–351.

[20] **Bjorkegren, L.E. and Hamberg, K.** (2000) Silicon alloyed ductile iron with excellent ductility and machinability. *Hommes et Fonderie(France)*. 307, 10–20.

[21] **Reardon, A.C.** (2011) *Metallurgy for the Non-metallurgist*. ASM International, .

[22] **Pelleg, J.** (2012) *Mechanical properties of materials*. Springer Science & Business Media, .

[23] **Glavas, Z., Strkalj, A., and Stojakovic, A.** (2016) The properties of silicon alloyed ferritic ductile irons. *Metalurgija*. *55* (3), 293–296.

[24] **Panneerselvam, S., Martis, C.J., Putatunda, S.K., and Boileau, J.M.** (2015) An investigation on the stability of austenite in Austempered Ductile Cast Iron (ADI). *Materials Science and Engineering A. 626*, 237-246.

[25] **Salman, S., Fındık, F., and Topuz, P.** (2007) Effects of various austempering temperatures on fatigue properties in ductile iron. *Materials & Design*. *28* 2210–2214.

[26] **Chiniforush, E.A., Rahimi, M.A., and Yazdani, S.** (2016) Dry sliding wear of Ni alloyed austempered ductile iron. *China Foundry*. *13* (5), 361–367.

[27] **Davis, J.R.** (1996) *ASM specialty handbook: Cast Irons*. ASM international, .

[28] **Metals Handbook** (1991) *Volume 4: Heat Treating*. ASM International. 10.

[29] **Cardoso, P.H.S., Israel, C.L., and Strohaecker, T.R.** (2014) Abrasive wear in Austempered Ductile Irons : A comparison with white cast irons. *Wear*. *313* (1–2), 29–33.

[30] **Rao, P.P. and Putatunda, S.K.** (1998) Dependence of fracture toughness of austempered ductile iron on austempering temperature. *Metallurgical and Materials Transactions A*. *29* (12), 3005–3016.

[31] **Chapetti, M.D.** (2007) High-cycle fatigue of austempered ductile iron (ADI). *International Journalof Fatigue. 29*, 860–868.

[32] **Liu, J.** (2006) Unique microstructure and excellent mechanical properties of ADI. *Carbon*. *897*, 3.

[33] **Tanaka, Y. and Kage, H.** (1992) Development and application of austempered spheroidal graphite cast iron. *Materials Transactions, JIM*. *33* (6), 543–557.

[34] **Putman, D.C. and Thomson, R.C.** (2003) Microstructural and mechanical property modelling of austempered ductile iron. *International Journal of Cast Metals Research*. *16* (1–3), 191–196.

[35] **Url-1** <*https://www.totalmateria.com*>, date retrieved 10.10.2018.

[36] **Darwish, N. and Elliott, R.** (1993) Austempering of low manganese ductile irons. *Materials Science and Technology*. *9* (7), 572–585.

[37] **Sahin, Y., Erdogan, M., and Kilicli, V.** (2007) Wear behavior of austempered ductile irons with dual matrix structures. *Materials Science and Engineering: A*. *444* (1–2), 31–38.

[38] **Yang, J. and Putatunda, S.K.** (2004) Influence of a novel two-step austempering process on the strain-hardening behavior of austempered ductile cast iron (ADI). *Materials Science and Engineering: A*. *382* (1–2), 265–279.

[39] **Elsayed, A.H., Megahed, M.M., Sadek, A.A., and Abouelela, K.M.** (2009) Fracture toughness characterization of austempered ductile iron produced using both conventional and two-step austempering processes. *Materials & Design*. *30* (6), 1866–1877.

[40] **Hsu, C.-H. and Lin, K.-T.** (2011) A study on microstructure and toughness of copper alloyed and austempered ductile irons. *Materials Science and Engineering: A*. *528* (18), 5706–5712.

[41] **Krzy, A. and Kocha, A.** (2014) Properties and structure of high-silicone Austempered Ductile Iron. *Archives of Foundry Engineering*. *14* (2), 91–94.

[42] **Kochański, A., Krzyńska, A., and Radziszewski, T.** (2014) Highsilicone Austempered Ductile Iron. *Archives of Foundry Engineering*. *14* (1), 55–58.

[43] **Larker, R.** (2014) Austempered ductile iron, method for producing this and component comprising this iron. *U.S. Patent No. 8,858,736*. Washington, DC: U.S. Patent and Trademark Office.

[44] **Benam, A.S.** (2015) Effect of alloying elements on the austempered ductile iron (ADI) properties and its process. *China Foundry*. *12* (1), 54–70.

[45] **Smith, W.J. and Goodwin F.E.** (2010) *4.06 Hot Dipped Coatings.in*: Elsevier.

[46] **Fan, D.W. and Cooman, B.C. De** (2010) Formation of an aluminide coating on hot stamped steel. *ISIJ International*. *50* (11), 1713–1718.

[47] **Bariani, P.F., Bruschi, S., Ghiotti, A., and Medea, F.** (2014) *Wear behaviour of Al-Si and Zn coated 22MnB5 in hot stamping*. in: Adv. Mater. Res., Trans Tech Publ, pp. 209–218.

[48] **Huilgol, P., Udupa, K.R., and Bhat, K.U.** (2018) Formation of microstructural features in hot-dip aluminized AISI 321 stainless steel. *International Journal of Minerals, Metallurgy, and Materials*. *25* (2), 190–198.

[49] **Karbasian, H. and Tekkaya, A.E.** (2010) Journal of Materials Processing Technology A review on hot stamping. *Journal of Materials Processing Tech. 210* (15), 2103–2118.

[50] **Merklein, M. and Lechler, J.** (2006) Characterisation of the flow properties of the quenchenable ultra high strength steel 22MnB5. *CIRP Annals-Manufacturing Technology*. *55* (1), 229–232.

[51] **Lin, M.-B. and Wang, C.-J.** (2010) Microstructure and high temperature oxidation behavior of hot-dip aluminized coating on high silicon ductile iron. *Surface and Coatings Technology*. *205* (5), 1220–1224.

[52] **Lin, M.-B., Wang, C.-J., and Volinsky, A.A.** (2011) Isothermal and thermal cycling oxidation of hot-dip aluminide coating on flake/spheroidal graphite cast iron. *Surface and Coatings Technology*. *206* (7), 1595–1599.

[53] **Richards, R.W., Jones, R.D., Clements, P.D., and Clarke, H.** (1994) Metallurgy of continuous hot dip aluminizing. *International Materials Reviews*. *39* (5), 191–212.

[54] **Patterson, W.C. and Hall, J.E.** (1970) Batch Hot-Dip Aluminizing. SAE Technical Paper, .

[55] **Caseres, L. and Sagues, A.A.** (2005) Corrosion of Aluminized Steel in Scale Forming Waters. *Corrosion/2005*. NACE International, Houston.

[56] **Kim, K.H., van Daele, B., Van Tendeloo, G., and Yoon, J.K.** (2006) Observations of intermetallic compound formation of hot dip aluminized steel. in: Mater. Sci. Forum, Trans Tech Publ, pp. 1871–1876.

[57] **Awan, G.H. and Ul Hasan, F.** (2008) The morphology of coating/substrate interface in hot-dip-aluminized steels. *Materials Science and Engineering: A*. *472* (1–2), 157–165.

[58] **Huilgol, P., Udupa, K.R., and Bhat, K.U.** (2018) Metastable microstructures at the interface between AISI 321 steel and molten aluminum during hot-dip aluminizing. *Surface and Coatings Technology*. *348* 22–30.

[59] **Bahadur, A.** (1991) Structural studies of hot dip aluminized coatings on mild steel. *Materials Transactions, JIM*. *32* (11), 1053–1061.

[60] **Kwon, S.C. and Lee, J.Y.** (1981) Interface morphology between the aluminide layer and iron substrate in the hot-dip aluminizing process. *Canadian Metallurgical Quarterly*. *20* (3), 351–357.

[61] **Liberski, P., Gierek, A., Kania, H., Podolski, P., and Tatarek, A.** (2008) Formation of coatings from a liquid phase on the surface of iron-base alloys. *Archives of Foundry Engineering*. *8* (4), 93.

[62] **Cheng, W.-J. and Wang, C.-J.** (2011) Study of microstructure and phase evolution of hot-dipped aluminide mild steel during high-temperature diffusion using electron backscatter diffraction. *Applied Surface Science*. *257* (10), 4663–4668.

[63] **Kobayashi, S. and Yakou, T.** (2002) Control of intermetallic compound layers at interface between steel and aluminum by diffusion-treatment. *Materials Science and Engineering: A*. *338* (1–2), 44–53.

[64] **Springer, H., Kostka, A., Payton, E.J., Raabe, D., Kaysser-Pyzalla, A., and Eggeler, G.** (2011) On the formation and growth of intermetallic phases during interdiffusion between low-carbon steel and aluminum alloys. *Acta Materialia*. *59* (4), 1586–1600.

[65] **Abro, M.A. and Lee, D.B.** (2017) Microstructural Changes of Al Hot-Dipped P91 Steel during High-Temperature Oxidation. *Coatings*. *7* (2), 31.

[66] **Qian, W., LENG, X., YANG, T., and YAN, J.** (2014) Effects of Fe—Al intermetallic compounds on interfacial bonding of clad materials. *Transactions of Nonferrous Metals Society of China*. *24* (1), 279–284.

[67] **Atzori, B., Meneghetti, G., and Ricotta, M.** (2014) Unified material parameters based on full compatibility for low-cycle fatigue characterisation of as-cast and austempered ductile irons. *International Journal of Fatigue*. *68*, 111–122.

[68] **Kumari, U.R. and Rao, P.P.** (2009) Study of wear behaviour of austempered ductile iron. *Journal of Materials Science*. *44* (4), 1082.

[69] **Lin, C.-K., Lai, P.-K., and Shih, T.-S.** (1996) Influence of microstructure on the fatigue properties of austempered ductile irons—I. High-cycle fatigue. *International Journal of Fatigue*. *18* (5), 297–307.

[70] **Cullity, B.D. and Graham, C.D.** (2011) *Introduction to magnetic materials*. John Wiley & Sons, .

[71] **Ansaripour, A., Monajatizadeh, H., and Amighian, J.** (2014) Effect of isothermal annealing on the magnetic properties of cold-rolled low-carbon steel with magnetic hysteresis-loop measurements. *Materiali In Tehnologije*. *48* (3), 367–371.

[72] **Renzetti, R.A., Sandim, H.R.Z., Sandim, M.J.R., Santos, A.D. dos, Möslang, A., and Raabe, D.** (2011) Annealing effects on microstructure and coercive field of ferritic–martensitic ODS Eurofer steel. *Materials Science and Engineering: A*. *528* (3), 1442–1447.

[73] **Sablik, M.J., Yonamine, T., and Landgraf, F.J.G.** (2004) Modeling plastic deformation effects in steel on hysteresis loops with the same maximum flux density. *IEEE Transactions on Magnetics*. *40* (5), 3219–3226.

[74] **Myszka, D., Kowalczyk, M., Spychalski, M., and Wieczorek, A.** (2016) Thermal Stability of Austempered Ductile Iron Evaluated in a Temperature Range of 20-300K. *Materials Science*. *22* (1), 153–157.

[75] **Cullity, B.D. and Stock, S.R.** (2014) *Elements of X-ray Diffraction*. Pearson Education, .

[76] **Putatunda, S.K.** (2001) Fracture toughness of a high carbon and high silicon steel. *Materials Science and Engineering: A*. *297* (1–2), 31–43.

[77] **Zhao, L., Van Dijk, N.H., Brück, E., Sietsma, J., and Van der Zwaag, S.** (2001) Magnetic and X-ray diffraction measurements for the

determination of retained austenite in TRIP steels. *Materials Science and Engineering: A*. *313* (1–2), 145–152.

[78] **Saleh, M.H. and Priestner, R.** (2001) Retained austenite in dual-phase silicon steels and its effect on mechanical properties. *Journal of Materials Processing Technology*. *113* (1–3), 587–593.

[79] **Hassan, M.F. and Megahed, S.M.** (2000) *Current Advances in Mechanical Design and Production VII*. Elsevier, .

[80] **Sicupira, F.L., Sandim, M.J.R., Sandim, H.R.Z., Santos, D.B., and Renzetti, R.A.** (2016) Quantification of retained austenite by X-ray diffraction and saturation magnetization in a supermartensitic stainless steel. *Materials Characterization*. *115* 90–96.

[81] **Jacques, P.J., Allain, S., Bouaziz, O., De, A., Gourgues, A.-F., Hance, B.M., et al.** (2009) On measurement of retained austenite in multiphase TRIP steels—results of blind round robin test involving six different techniques. *Materials Science and Technology*. *25* (5), 567–574.

[82] **Franetovic, V., Shea, M.M., and Ryntz, E.F.** (1987) Transmission electron microscopy study of austempered nodular iron: Influence of silicon content, austenitizing time and austempering temperature. *Materials Science and Engineering*. *96* 231–245.

[83] **Putatunda, S.K., Singar, A. V, Tackett, R., and Lawes, G.** (2009) Development of a high strength high toughness ausferritic steel. *Materials Science and Engineering: A*. *513* 329–339.

[84] **Srivatsan, T.S., Imam, M.A., and Srinivasan, R.** (2012) *Fatigue of Materials II: Advances and Emergences in Understanding*. John Wiley & Sons, .

[85] **Li, D., Feng, Y., Song, S., Liu, Q., Bai, Q., Ren, F., et al.** (2015) Influences of silicon on the work hardening behavior and hot deformation behavior of Fe–25 wt% Mn–(Si, Al) TWIP steel. *Journal of Alloys and Compounds*. *618*, 768–775.

[86] **Laurent, S., Henoumont, C., Stanicki, D., Boutry, S., Lipani, E., Belaid, S., et al.** (2017) *MRI contrast agents: from molecules to particles*. Springer, .

[87] **Nakano, Y. and Kawano, Y.** (1979) Magnetic properties of cast iron. *Imono(Journal of the Japan Foundrymen's Society)*. *51* (6), 315–321.

[88] **Jiles, D.C.** (1988) Magnetic properties and microstructure of AISI 1000 series carbon steels. *Journal of Physics D: Applied Physics*. *21* (7), 1186.

[89] **Stefanita, C.-G.** (2012) *Magnetism: Basics and Applications*. Springer Science & Business Media, .

[90] **Keough, J.R. and Hayrynen, K.L.** (2000) *Automotive applications of austempered ductile iron (ADI): a critical review*. *SAE Transactions*. 344–354.

[91] **Bjorkegren, L.-E., Hamberg, K., and Johannesson, B.** (1996) Mechanical properties and machinability of Si-solution-hardened ferritic ductile iron. *Transactions of the American Foundrymen's Society,*. *104* 139–145.

[92] **Lin, C.-K., Hsu, C.-H., Cheng, Y.-H., Ou, K.-L., and Lee, S.-L.** (2015) A study on the corrosion and erosion behavior of electroless nickel and TiAlN/ZrN duplex coatings on ductile iron. *Applied Surface Science*. *324*, 13–19.

[93] **Hsu, C.-H., Chen, K.-L., Lee, C.-Y., and Lu, K.-C.** (2009) Effects of low-temperature duplex coatings on corrosion behavior of austempered ductile iron. *Surface and Coatings Technology*. *204* (6–7), 997–1001.

[94] **Colombo, D.A., Echeverría, M.D., Moncada, O.J., and Massone, J.M.** (2012) PVD TiN and CrN coated austempered ductile iron: analysis of processing parameters influence on coating characteristics and substrate microstructure. *ISIJ International*. *52* (1), 121–126.

[95] **Hsu, C.-H., Chen, K.-L., and Lu, J.-H.** (2008) Effects of electroless nickel interlayer on surface properties of CrN arc-coated austempered ductile iron. *Surface and Coatings Technology*. *203* (5–7), 868–871.

[96] **Ei-Mahallawy, N.A., Taha, M.A., Shady, M.A., Ei-Sissi, A.R., Attia, A.N., and Reif, W.** (1997) Analysis of coating layer formedon steel strips during aluminising by hot dipping in Al-Si baths. *Materials Science and Technology*. *13* (10), 832–840.

[97] **Deqing, W.** (2008) Phase evolution of an aluminized steel by oxidation treatment. *Applied Surface Science*. *254* (10), 3026–3032.

[98] **Wang, Y., Xiong, J., Yan, J., Fan, H., and Wang, J.** (2011) Oxidation resistance and corrosion behavior of hot-dip aluminized coatings on commercial-purity titanium. *Surface and Coatings Technology*. *206* (6), 1277–1282.

[99] **Dejun, K., Yongzhong, W., and Dan, L.** (2014) Salt Spray Corrosion Resistance of Aluminized Coatings on X70 Pipeline Steel by Laser Thermal Radiation. *Rare Metal Materials and Engineering*. *43* (9), 2083–2088.

[100] **Jiang, W., Fan, Z., Li, G., Liu, X., and Liu, F.** (2016) Effects of hot-dip galvanizing and aluminizing on interfacial microstructures and mechanical properties of aluminum/iron bimetallic composites. *Journal of Alloys and Compounds*. *688*, 742–751.

[101] **Jamnapara, N.I., Mukherjee, S., and Khanna, A.S.** (2015) Phase transformation of alumina coating by plasma assisted tempering of aluminized P91 steels. *Journal of Nuclear Materials*. *464*, 73–79.

[102] **Zhang, Q.Y., Zhou, Y., Liu, J.Q., Chen, K.M., Mo, J.G., Cui, X.H., et al.** (2016) Wear behavior and mechanism of Fe-Al intermetallic coating prepared by hot-dip aluminizing and diffusion. *Metallurgical and Materials Transactions A*. *47* (5), 2232–2242.

[103] **Rundman, K.B. and Klug, R.C.** (1982) An X-Ray and Metallographic Study of an Austempered Ductile Cast Iron.(Retroactive Coverage). *Transactions of the American Foundrymen's Society*. *90*, 499–508.

[104] **Kang, S., Han, K., Kim, K., Kang, Y., Son, K., and Kim, D.** (2012) Formation behavior of an intermetallic compound layer during the hot dip aluminizing of cast iron. *ISIJ International*. *52* (7), 1342–1347.

[105] **Yeremenko, V.N., Natanzon, Y. V, and Dybkov, V.I.** (1981) The effect of dissolution on the growth of the Fe2Al5 interlayer in the solid iron-

liquid aluminium system. *Journal of Materials Science*. *16* (7), 1748–1756.

[106] **Wang, C.-J. and Chen, S.-M.** (2006) The high-temperature oxidation behavior of hot-dipping Al–Si coating on low carbon steel. *Surface and Coatings Technology*. *200* (22–23), 6601–6605.

[107] **Badaruddin, M., Wang, C.J., Wardono, H., Tarkono, and Asmi, D.** (2016) High-temperature oxidation behavior of aluminized AISI 4130 steel. in: AIP Conf. Proc., AIP Publishing, p. 40002.

[108] **Lopez, M.F. and Escudero, M.L.** (1998) Corrosion behaviour of FeAl-type intermetallic compounds. *Electrochimica Acta*. *43* (7), 671–678.

[109] **Windmann, M., Röttger, A., and Theisen, W.** (2013) Phase formation at the interface between a boron alloyed steel substrate and an Al-rich coating. *Surface and Coatings Technology*. *226*, 130–139.

[110] **Wang, C.J., Lee, J.W., and Twu, T.H.** (2003) Corrosion behaviors of low carbon steel, SUS310 and Fe–Mn–Al alloy with hot-dipped aluminum coatings in NaCl-induced hot corrosion. *Surface and Coatings Technology*. *163*, 37–43.

[111] **Potesser, M., Schoeberl, T., Antrekowitsch, H., and Bruckner, J.** (2006) The characterization of the intermetallic Fe-Al layer of steel-aluminum weldings. in: EPD Congr., San Antonio Texas, USA, p. 167.

[112] **Matysik, P., Jóźwiak, S., and Czujko, T.** (2015) Characterization of low-symmetry structures from phase equilibrium of Fe-Al system—Microstructures and mechanical properties. *Materials*. *8* (3), 914–931.

[113] **Yürektürk, Y. and Baydoğan, M.** (2017) Effect of microstructural features on mechanical and magnetic properties of austempered high-silicon ductile irons. *ISIJ International*. *57* (11), 2049–2057.

[114] **Angella, G., Zanardi, F., and Donnini, R.** (2016) On the significance to use dislocation-density-related constitutive equations to correlate strain hardening with microstructure of metallic alloys: the case of conventional and austempered ductile irons. *Journal of Alloys and Compounds*. *669*, 262–271.

[115] **Stern, M. and Geary, A.L.** (1957) Electrochemical polarization I. A theoretical analysis of the shape of polarization curves. *Journal of the Electrochemical Society*. *104* (1), 56–63.

[116] **Hsu, C.-H. and Lin, K.-T.** (2014) Effects of Copper and Austempering on Corrosion Behavior of Ductile Iron in 3.5 Pct Sodium Chloride. *Metallurgical And Materials Transactions A*. *45* (3), 1517–1523.

[117] **Hsu, C.-H. and Chen, M.-L.** (2010) Corrosion behavior of nickel alloyed and austempered ductile irons in 3.5% sodium chloride. *Corrosion Science*. *52* (9), 2945–2949.

[118] **Antunes, R.A., Ichikawa, R.U., Martinez, L.G., and Costa, I.** (2014) Characterization of corrosion products on carbon steel exposed to natural weathering and to accelerated corrosion tests. *International Journal of Corrosion*. 2014.

[119] **Allély, C., Dosdat, L., Clauzeau, O., Ogle, K., and Volovitch, P.** (2014) Anticorrosion mechanisms of aluminized steel for hot stamping. *Surface and Coatings Technology*. *238*, 188–196.

[120] **Konys, J., Krauss, W., Voss, Z., and Wedemeyer, O.** (2007) Comparison of corrosion behavior of bare and hot-dip coated EUROFER steel in flowing Pb–17Li. *Journal of Nuclear Materials*. *367*, 1144–1149.

[121] **Colombo, D.A., Echeverría, M.D., Laino, S., Dommarco, R.C., and Massone, J.M.** (2014) Sliding wear behavior of PVD CrN and TiN coated austempered ductile iron. *ISIJ International*. *54* (12), 2860–2867.

[122] **Amirsadeghi, A. and Sohi, M.H.** (2008) Comparison of the influence of molybdenum and chromium TIG surface alloying on the microstructure, hardness and wear resistance of ADI. *Journal of Materials Processing Technology*. *201* (1–3), 673–677.

[123] **Amirsadeghi, A., Sohi, M.H., and Bozorg, S.F.K.** (2008) Effects of TIG surface melting and chromium surface alloying on microstructure, hardness and wear resistance of ADI. *Journal of Iron and Steel Research, International*. *15* (4), 86–94.

[124] **Roy, A. and Manna, I.** (2001) Laser surface engineering to improve wear resistance of austempered ductile iron. *Materials Science and Engineering: A*. *297* (1–2), 85–93.

[125] **Shamanian, M., Abarghouie, S.M.R.M., and Pour, S.R.M.** (2010) Effects of surface alloying on microstructure and wear behavior of ductile iron. *Materials & Design*. *31* (6), 2760–2766.

[126] **Zhang, Q.Y., Zhou, Y., Liu, J.Q., Chen, K.M., Mo, J.G., Cui, X.H., et al.** (2015) Comparative research on dry sliding wear of hot-dip aluminized and uncoated AISI H13 steel. *Wear*. *344*, 22–31.

[127] **Yürektürk, Y. and Baydoğan, M.** (2018) Characterization of ferritic ductile iron subjected to successive aluminizing and austempering. *Surface and Coatings Technology*. *347*, 142–149.

[128] **Rao, P.P. and Putatunda, S.K.** (1997) Influence of microstructure on fracture toughness of austempered ductile iron. *Metallurgical and Materials Transactions A*. *28* (7), 1457–1470.

[129] **Kim, S.-Y. and Choi, C.-S.** (1980) A Study on mechanical properties of aluminized steel plate. *Journal of the Korean Institute of Surface Engineering*. *13* (2), 81–86.

[130] **Xu, D., Li, J., Meng, Q., Liu, Y., and Li, P.** (2014) Effect of heating rate on microstructure and mechanical properties of TRIP-aided multiphase steel. *Journal of Alloys and Compounds*. *614*, 94–101.

[131] **Badaruddin, M., Riza, R.T., and Zulhanif** (2018) The effect of diffusion treatment on the mechanical properties of hot-dip aluminum coating on AISI P20 steel. in: AIP Conf. Proc., AIP Publishing, p. 50004.

[132] **Prado, J.M., Pujol, A., Cullell, J., and Tartera, J.** (1995) Dry sliding wear of austempered ductile iron. *Materials Science and Technology*. *11* (3), 294–298.

[133] **de Faria, D.L.A., Venâncio Silva, S., and de Oliveira, M.T.** (1997) Raman microspectroscopy of some iron oxides and oxyhydroxides. *Journal of Raman Spectroscopy*. *28* (11), 873–878.

[134] **Marciuš, M., Ristić, M., Ivanda, M., and Musić, S.** (2012) Formation of iron oxides by surface oxidation of iron plate. *Croatica Chemica Acta*. *85* (1), 117–124.

[135] **Baier-Saip, J.A., Avila, J.I., Tarrach, G., Cabrera, A.L., Fuenzalida, V., Zarate, R.A., et al.** (2005) Deep oxidation of aluminum by a DC oxygen plasma. *Surface and Coatings Technology*. *195* (2–3), 168–175.

[136] **Fang, J., Levchenko, I., and Ostrikov, K.K.** (2014) Free-standing alumina nanobottles and nanotubes pre-integrated into nanoporous alumina membranes. *Science and Technology of Advanced Materials*. *15* (4), 45004.

[137] **Mernagh, T.P. and Liu, L.** (1991) Raman spectra from the Al_2SiO_5 polymorphs at high pressures and room temperature. *Physics and Chemistry of Minerals*. *18* (2), 126–130.

[138] **Clarence Jr, K.** (1975) *Infrared and Raman Spectroscopy of lunar and terrestrial minerals*. in: Elsevier.

[139] **Rabinowicz, E. and Tanner, R.I.** (1966) Friction and wear of materials. *Journal of Applied Mechanics*. *33*, 479.

[140] **Stachowiak, G.W.** (2006) *Wear: materials, mechanisms and practice*. John Wiley & Sons, .

[141] **Ghaderi, A.R., Ahmadabadi, M.N., and Ghasemi, H.M.** (2003) Effect of graphite morphologies on the tribological behavior of austempered cast iron. *Wear*. *255* (1–6), 410–416.

CURRICULUM VITAE

Name Surname **:** Yakup Yürektürk

Place and Date of Birth **:** Van, Turkiye, 16/01/1987

E-Mail **:** yurekturky@gmail.com

EDUCATION:

- **B.Sc.:** 2012, Istanbul Technical University, Chemical and Metallurgical Faculty, Metallurgical and Material Engineering
- **M.Sc.:** 2013, Istanbul Technical University, Chemical and Metallurgical Faculty, Metallurgical and Material Engineering

PROFESSIONAL EXPERIENCE AND REWARDS:

- 2013-2018: Research Assistant at Istanbul Technical University, ISTANBUL

PUBLICATIONS, PRESENTATIONS AND PATENTS ON THE THESIS:

- **Yürektürk, Y.** and Baydoğan, M. (2017) Effect of microstructural features on mechanical and magnetic properties of austempered high-silicon ductile irons. *ISIJ International*. 57 (11), 2049–2057.
- **Yürektürk, Y.** and Baydoğan, M. (2017) Estimating volume fractions of microstructural constituents in austempered high silicon alloyed GJS 600-10 ductile iron through magnetic measurements (VSM). *Materials Science Forum*. 907 50–55.
- **Yürektürk, Y.** and Baydoğan, M. (2018) Characterization of ferritic ductile iron subjected to successive aluminizing and austempering. *Surface and Coatings Technology*. 347 142–149.
- **Yürektürk, Y.** and Baydoğan, M. (2018) Effect of aluminizing and austempering processes on structural, mechanical and wear properties of a SSF ductile iron. *Materials Research Express*.

OTHER PUBLICATIONS, PRESENTATIONS AND PATENTS:

- Tekoğlu, Emre., Ağaoğulları, D., **Yürektürk, Y.**, Bulut, B. and Öveçoğlu, M.L. (2018) Characterization of LaB6 particulate-reinforced eutectic Al-12.6 wt%Si composites fabricated via mechanical alloying and spark plasma sintering. *Powder Technology*. 340, 473-483.
- **Yürektürk, Y.**, Muhaffel, F. and Baydoğan, M. (2015) Characterization of micro arc oxidized 6082 aluminum alloy in an electrolyte containing carbon nanotubes. *Surface and Coatings Technology*. 269, 83-90.
- Kilic, D., Muhaffel, F., **Yurekturk, Y.** and Baydogan, M. (2015). Influence of Pulse Time on the Structural and Tribological Properties of Micro Arc Oxidized AZ91D Magnesium Alloy. in: Magnesium Technology 2015, Springer, pp. 339-342.
- Yazıcı, S.K., Muhaffel, F., **Yürektürk, Y.** and Baydoğan, M. (2014) Characterization and wear properties of carbon nanotubes incorporated ceramic coatings on Ti6Al4V and Ti6Al7Nb alloy. *Journal of Achievements in Materials and Manufacturing Engineering*. 65, 73-78.
- **Yürektürk, Y.**, Muhaffel, F. and Baydoğan, M. (2013) Effect of process parameters on surface properties of micro arc oxidized 6082 aluminum alloy. *Academic Journal of Science*. 2, 379-384.
- Ünlü N., **Yürektürk Y.,** Ateş B., Sağır H., Kara İ.H., Tüfekçioğlu K.Ç., Yılmaz E.D., and Çimenoğlu, H. 2018: AL8Mg-MultiWall-Carbon Nano Composites Prepared by Mechanical Milling and Hot Pressing. 2. Ulusal Karbon Konferansı March 16-17, 2018 İstanbul, Turkey.
- Altay M., **Yürektürk Y.,** and Baydoğan, M. 2018: Hot Dip Aluminizing of Commercially Pure (CP) Titanium. 1st International Symposium on Light Alloys and Composite Materials (ISLAC'18), March 22-24, 2018 Karabük, Turkey.
- Rashidi A., **Yürektürk Y.,** and Baydoğan, M. 2018: Effect of Intermediate Deformation on Formability Characteristics of Retrogression and Reaged (RRA) 7075 Al Alloy. 1st International Symposium on Light Alloys and Composite Materials (ISLAC'18), March 22-24, 2018 Karabük, Turkey.
- Taşlıçay C., **Yürektürk Y.,** Muhaffel F., and Baydoğan, M. 2017: A Ceramic Coating for Corrosion Protection on AISI 316Ti Stainless Steel. 2nd International Conference on Material Science and Technology in Cappadocia (IMSTEC 2017), October 11-13, 2017 Nevşehir, Turkey.
- **Yürektürk Y.,** Muhaffel F., and Baydoğan, M. 2017: Formation of a Wear-Resistant Oxide Coating on High Silicon Cast Iron by Combining Aluminizing and Micro Arc Oxidation Methods. 9th International Conference on Tribology (BalkanTRib'17), September 13-15, 2017 Nevşehir, Turkey.
- Taşlıçay C., **Yürektürk Y.,** Muhaffel F., and Baydoğan, M. 2017: Production of a Protective Alumina Coating on 316Ti Grade Stainless Steel by Micro Arc Oxidation Process. 9th International Conference on Tribology (BalkanTRib'17), September 13-15, 2017 Nevşehir, Turkey.
- Çamlıbel B., Muhaffel F., **Yürektürk Y.,** and Baydoğan, M. 2017: Microstructural Characterization of Micro Arc Oxidized ZA-8 Zinc-aluminum Alloy. 31th

International Conference on Surface Modification Technologies (SMT31), July 5-7, 2017 Mons, Belgium.

- Aytan G., **Yürektürk Y.,** and Baydoğan, M. 2017: Effect of pre-straining and baking temperature on bake hardening behaviour of hot-dip galvanized steels. 10th International Conference on Materials Science Engineering (BraMat 2017), March 8-11, 2017 Braşov, Romania.
- Gider G., **Yürektürk Y.,** Muhaffel F., and Baydoğan, M. 2016: Influence of Austempering Temperature on Microstructural and Mechanical Properties of EN GJS 500 7 and EN GJS 600 3 Grades Nodular Cast Irons. 5th Heat Treatment Symposium, June 2-3, 2016 İstanbul, Turkey.
- Gider G., **Yürektürk Y.,** Malcıoğlu A.U., Muhaffel F., and Baydoğan, M. 2016: Effect of Single Step and Two Step Austempering on Microstructure and Mechanical Properties of a High Silicon Ductile Iron. 1st International Conference on Advances in Automotıve Technologies 2016, October 11-14, 2016 İstanbul, Turkey.
- Gider G., **Yürektürk Y.,** Paksoy A.H., Muhaffel F., and Baydoğan, M. 2016: Microstructural Investigation and Wear Performance of Spheroidal Graphite Cast Iron Treated by a Two Step Austempering Process. 16th International Materials Symposium (IMSP'16), October 12-14, 2016 Denizli, Turkey.
- Açıksöz M., **Yürektürk Y.,** Muhaffel F., and Baydoğan, M. 2016: Characterization of Micro Arc Oxidized Unalloyed Low Carbon Steel After Hot Dip Aluminizing Process. 12th International Conference on Diffusion in Solids and Liquids (DSL2016), June 26-30, 2016 Split, Croatia.
- Taşlıçay C., **Yürektürk Y.,** Muhaffel F., and Baydoğan, M. 2016: Characteristics of Ceramic Coating Fabricated by Micro Arc Oxidation on Aluminized Stainless Steel. International Conference on Material Science and Technology in Cappadocia (IMSTEC 2016), April 6-8, 2016 Nevşehir, Turkey.
- Yerli N., Erol Taygun M.M., **Yürektürk Y.,** and Oskay, S. 2016: Fabrication and Characterization of Copper Doped Polymer Bioactive Glass Composite Scaffolds. Recent Advances in Nanotechnology (RAN'16), April 1-2, 2016 Prague, Czech Republic.
- Malcıoğlu A.U., **Yürektürk Y.,** Muhaffel F., and Baydoğan, M. 2015: Tribological Investigation of Austempered Grey Cast Iron for Automotive Components under Dry Sliding Conditions. 1st International Conference on Tribology (TURKEYTRIB'15), October 7-9, 2015 İstanbul, Turkey.
- Bostan B., **Yürektürk Y.,** Motallabzadeh A., Atar E., and Çimenoğlu H. 2015: Nitriding Effect on High Temperature Wear Resistance of High Speed Tool Steels. 2nd International Iron&Steel Symposium (IISS'15), April 1-3, 2015 Karabük, Turkey.
- **Yürektürk Y.,** Kayalı E.S., Baydoğan M., and Çimenoğlu H. 2015: Failure Analysis Study on a Superheater Tube. 15th International Materials Symposium (IMSP'14), October 15-17, 2014 Denizli, Turkey.
- **Yürektürk Y.,** Kayalı E.S., Baydoğan M., and Çimenoğlu H. 2015: Failure Analysis Study on an Aluminum Extrusion Die. 10th International Fracture Conference, April 24-26, 2014 Kayseri, Turkey.